Single particle dynamics in liquid crystalline phases formed by filamentous viruses

Laura Álvarez Francés

▶ To cite this version:

Laura Álvarez Francés. Single particle dynamics in liquid crystalline phases formed by filamentous viruses. Chemical Physics [physics.chem-ph]. Université de Bordeaux; KU Leuven (1970-..), 2016. English. NNT : 2016BORD0429 . tel-01534484

HAL Id: tel-01534484

https://theses.hal.science/tel-01534484

Submitted on 7 Jun 2017

THÈSE EN COTUTELLE PRÉSENTÉE

POUR OBTENIR LE GRADE DE

DOCTEUR DE

L'UNIVERSITÉ DE BORDEAUX

ÉCOLE DOCTORALE DE CHIMIE

SPÉCIALITÉ : PHYSIQUE CHIMIE

Par Laura ÁLVAREZ FRANCÉS

Single Particle dynamics in liquid crystalline phases formed by filamentous viruses

Sous la direction de Eric GRELET et
de Minne Paul LETTINGA

Soutenue le 21 Décembre 2016

Membres du jury:

M. BASCHNAGEL, Jörg	Professeur à l'Université de Strasbourg	Rapporteur
M. DAVIDSON, Patrick	Directeur de Recherche, CNRS	Rapporteur
M. POULIN, Philippe	Directeur de Recherche, CNRS	Examinateur
M. WENSINK, Rik	Chargé de Recherche, CNRS	Examinateur

Titre : Dynamique individuel de particule dans les phases de cristaux liquid formé par les bactériophages filamenteux

Résumé : [1700 caractères maximun, espaces compris]

Cette thèse porte sur la dynamique des différentes mésophases liquides cristallines et des transitions de phase d'un modèle colloïdal de particules en forme de bâtonnent: les virus fd. L'étude de l'auto-organisation des cristaux liquides colloïdaux traite des phénomènes les plus simples de formation de systèmes structurés. Dans un système où les particules anisotropes ont des interactions de noyau rigide, l'auto-organisation est purement entropique en raison de la maximisation du volume libre du système. Ainsi, il y a une modification de la dynamique qui peut être mesurée, et fournisse des informations sur le volume libre disponible et la structure de la mésophase.

La dynamique des bâtonnets fd peut être mesurée avec précision à l'aide de techniques de microscopie à fluorescence. Nous quantifions la dynamique autour des transitions de phase et l'effet de la flexibilité et de la longueur en tant que mécanisme pour relâcher la contrainte de leurs voisins. En outre, dans une structure lamellaire *guest-host*, nous avons prouvé la pérmeation favorisée des bâtonnets longs *guest* à travers les couches de la matrice Smectique *host* formée de plus petites particules. Dans ces conditions, la super-diffusion de la particule invitée est également observée lorsqu'elle se diffuse dans une limite de grain. Il s'agit d'un pas en avant pour comprendre la dynamique des systèmes structurés colloïdaux et aussi dans le développement des nouveaux matériaux basés sur des diffuseurs rapides avec des applications potentielles dans la biologie médicale. Les résultats expérimentaux sont très prometteurs et stimulantes.

Mots clés : Cristaux Liquid, fd virus, colloïdes, dynamique

Title : Single particle dynamics in liquid crystalline phases formed by filamentous viruses

Abstract : [1700 caractères maximun]

This thesis treats the dynamics of the different liquid crystalline mesophases and phase transitions of a model colloidal of rod-like particles: the fd viruses. The study of the self-organization of colloidal liquid crystals treats the simplest phenomena of forming structured systems. In a system where anisotropic particles have hard core interactions, the self-organization is purely entropy driven due to the maximization of the free volume of the system. Thus, there is a change on the dynamics at single particle level that can be measured, providing information on the available free volume and the structure of the mesophase.

The fd rods are a versatile colloidal system and their self-dynamics can be accurately measured using fluorescence microscopy techniques. We quantify the relaxation of the dynamics around the phase transitions and the effect of flexibility and length as a mechanism to release the constraint of their neighbors. Moreover, in a guest-host lamellar structure we demonstrate that a big guest particle is faster than the small host, if the guest particle is not commensurate in the host energy landscape. In these conditions, also the super-diffusion of the guest particle is observed when it diffuses into a grain boundary. This is a step forward to understand the dynamics of colloidal structured systems and also in the development the new materials based on fast diffusers with potential applications in drug delivery. The extensive experimental results are completed by a whole analysis and interpretation, being very promising and challenging.

Keywords : Liquid crystals, fd viruses, colloids, self-dynamics

Centre de Recherche Paul Pascal

[CNRS, CRPP, UPR 8641, F-33600 Pessac, France.]

Résumé

Les colloïdes sont des particules de 1nm à 10 µm qui se dispersent dans du liquide ou du gaz et qui sont sensibles aux fluctuations thermiques. Ils manifestent un mouvement Brownien, d'abord observé par Robert Brown en 1827 [1] et expliqué plus tard par Jean Perrin et Albert Einstein. De plus, les particules colloïdales peuvent prendre n'importe quelle forme : sphères, bâtonnets, particules en forme d'étoile et plaquette, parmi bien d'autres [2-4]. Durant ces dernières décennies, les suspensions colloïdales ont attiré l'attention des chercheurs grâce à leurs nombreuses applications pratiques et leur présence dans les systèmes biologiques. Concrètement, les colloïdes en forme de bâtonnet comment par exemple le cytosquelette, les protéines musculaires et les virus [9-11]. Ces systèmes s'organisent de différentes façons selon leur fonction ou même des changements du milieu où ils se trouvent. L'une des motivations des études dynamiques et cinétiques de ces systèmes est de comprendre le chemin que prennent ces systèmes vers l'ordre et le désordre [12-17]. Il a été observé que les particules colloïdales en forme de bâtonnet présentent un comportement unique en formant différentes mésophases de cristaux liquides, comme présenté dans la figure 1.1. Zocher observa le premier les tactoïdes biréfringents nématiques des bâtonnets inorganiques V2O5 dans un milieu isotrope en 1925 [18]. Plus tard, un comportement similaire a été découvert dans des particules biologiques comme le virus de la mosaïque du tabac (TMV) [19, 20]. D’autre part, des motifs smectiques ont été observés pour la première fois grâce à la monodispersitée de ces virus [21,22]. La coexistence entre les phases Isotrope et Nematique observée experimentalment, incita Lars Onsager à développer une théorie sur la transition de phase Isotrope-Nématique des bâtonnets rigides dans son séminaire de 1949 [23].

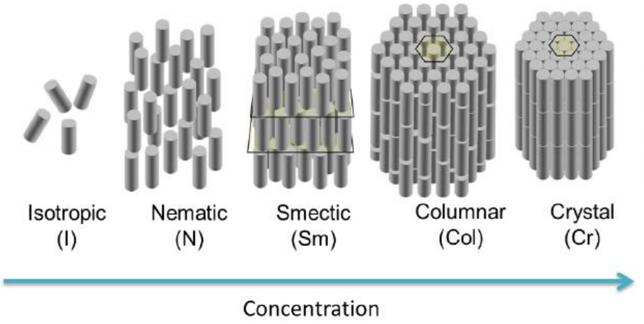

Figure 1.1 : schéma des différentes mésophases que forment les bâtonnets rigides lorsque la concentration augmente, des moins concentrées (isotropes) à la phase la plus dense (cristaux) [19]

Par définition, les bâtonnets rigides ne peuvent pas se superposer et ne se sentent que lorsqu'ils entrent en contact. Onsager a démontré comment les particules hautement anisotropes transitent de la phase liquid isotrope à la phase nématique en augmentant leur volume libre. En la phase Isotrope, les particules n'ont pas d'ordre de position, ni d'ordre d'orientation, contrairement à la phase Nématique où elles ont un ordre à longue distance d'orientation mais pas de position. Le travail d'Onsager a été étendu via simulation numériques pour inclure la transition de la phase Nématique à la phase Smectique, où les particules s'organisent selon d'ordre quasi-1D à longue distance, causé par le confinement en couches [8,9]. Les transitions entre ces phases sont causées uniquement par une maximisation de l'entropie, ce qui signifie que l'exclusion du volume libre entre les particules est suffisante pour créer les différentes mésophases. Ces systèmes sont appelés cristaux liquides lyotrope colloïdaux et leurs transitions de phases dépendent uniquement de leur concentration.

Indépendamment du virus TMV, les virus fd ont également montré des mésophases de cristaux liquides et, grâce à leurs propriétés physiques, sont considérés comme un bon système expérimental pour étudier les phénomènes de transition de phase ainsi que l'organisation des particules en forme de bâtonnets. Le type fdwt (*wild type*) est reconnu pour sa capacité à infecter *Escherichia coli* (E. Coli). Contrairement aux particules synthétiques, il est naturellement monodispersée en taille, ce qui favorise la formation de couches Smectiques [28]. De plus, le virus fd peut être visualisé grâce à des marquages fluorescents. Ses propriétés physiques peuvent être variées par modifications génétiques afin d'obtenir des mutations de taille ou rigidité différentes. C'est le cas pour le mutant fdY21M qui est légèrement plus long et beaucoup plus rigide que le fdwt. Le fort rapport d'aspect, L/D>100 rend la visualisation individuelle par microscopie fluorescente possible. Egalement, la transition I-N du virus solide fdY21M se passe à la même fraction volumique que la valeur prédite par Onsager [29]. En outre, ils exhibent mouvement Brownien qui peut être étudié pour comprendre les caractéristiques des différentes mésophases qui forment et la physique sous-jacente.

Puisque la transition de phase implique une différence dans le volume libre entre les phases, elle affecte directement la dynamique du système. Ainsi, la dynamique du virus fd a été étudiés intensivement ces dernières années, et ce pour chaque mesophase distincte. Dans la phase Isotropique diluée, les bâtonnets n'ont aucun ordre, ni de position ni d'orientation, ce qui cause une libre rotation et translation des bâtonnets. Les simulations ont montré que lorsque la transition de phase I-N approche, la diffusion rotationnelle s'arrête durant la phase Isotrope [30-32]. Après la transition de phase I-N, en la phase Nématique, la diffusion parallèle est plus importante, due à l'alignement des bâtonnets le long de l'axe des particules [33]. Ensuite, il a été découvert que la diffusion de ces bâtonnets durant la phase Smectic a lieu grâce au transport de matière entre les couches par sautes quantifiés d'amplitude égale à une longueur de virus [37-37]. Bien qu'un grand pas ait été effectué vers la compréhension des dynamiques des virus fd dans leurs différentes mesophases, l'effet direct de la dynamique dans les transitions de phase qui sont induites reste une question ouverte.

Cette Thèse fournit une étude de la dynamique des phases des cristaux liquides et des transitions de phase des bâtonnets colloïdaux en utilisant le virus filamenteux fd comme système modèle colloïdal. De plus, nous donnons un aperçu de l'impact de la structure de la mésophase sur la dynamique des particules de type bâtonnets, et l'influence des propriétés physiques des particules (longueur et flexibilité).

Nous avons étudiés la dynamique du mutant fdY21M à travers le diagramme de phase. Nous avons d'abord étudiés la dynamique autour de la transition de phase I-N. Durant la phase Isotropique proche de la transition Isotropique-Nématique, l'augmentation de la fraction volumique créé une situation dans laquelle la diffusion rotationnelle et translationnelle est limitée, due à « l'effet de tube ». L'étude de la diffusion translationnelle révèle une limitation de mouvement, ce qui est en accord avec les études précédentes [33]. Nous avons montré que non seulement le taux de diffusion est affecté, mais également le comportement Gaussien, ce qui est mis en avant par le changement de forme de la fonction de van Hove. Nous avons découvert que le mouvement Brownien est très restreint durant la phase Isotropique proche de la transition de phase I-N.

De plus, nous avons montré que pour les transitions N-SmA et SmA-SmB, la dynamique peut être caractérisée pour déterminer l'ordre des transitions de phase. En revanche, nous devons garder à l'esprit un possible problème d'homogénéité des échantillons. A ce haut taux de concentration, nous ne pouvons pas obtenir séparation de phase macroscopique, pour que la dynamique puisse être identifiée à ces transitions de phase.

Nous avons comparé les dynamiques entre les régimes isotropes dilués à semi dilués avant la transitions de phase pour des particules courtes et rigides ainsi que longues et flexibles. Nous avons montré un comportement dynamique différent qui dépend de la longueur de persistance de la particule. La particule flexible récupère plus rapidement le comportement gaussien à des concentrations correspondantes au régime semi-dilué. Ainsi, la flexibilité créé un mécanisme de diffusion pour relâcher la contrainte imposée par les bâtonnets alentours. Il peut être mis en relation avec le fait que la concentration de la phase Isotropique est plus haute pour les particules flexibles [29].

La proposition que la diffusion des particules browniennes diminue avec l'augmentation de la taille des particules n'est pas toujours vraie. Nous avons prouvé cet effet en mettant en évidence la pérmeation favorisée des bâtonnets longs dopés à travers les couches de la matrice Smectique hôte formée de plus petites particules. Nous avons montré que les grosses particules browniennes peuvent diffuser plus rapidement que les petites particules: le long M13KO7 dopées diffuse plus rapidement à travers les couches smectiques que les particules hôte (fdY21M) elles-mêmes.

Une particule peut ainsi sauter si une lacune temporaire existe dans une couche adjacente. A une concentration plus forte, le nombre des lacunes diminue. Comme les bâtonnets les plus longs sont toujours présents au moins dans deux couches en même temps, ils génèrent leur propre lacune et facilitent leur pénétration. Pour cette effet, la flexibilité du le long M13KO7 dopée peut certainement augmenter la diffusion, en accord avec les résultats obtenus pour la phase colonnaire durant laquelle le semi fdwt flexible montre un nombre de demi saut plus importants que pour le fdY21M plus rigide [104].

De plus, nous avons pu suivre les particules dopées dans les joints de grains. Il semblerait que ces particules diffusent depuis les couches Smectiques vers les lignes de dislocation au sein du joint de grains. Il a été démontré que cette cassure géométrique causé par des défauts puisse initier un super diffusion [173]. Nous avons pu calculer la dynamique des particules M13KO7 dopées, où un léger comportement de super diffusion a été observé dans des particules diffusant du domaine smectique vers un joint de grains. Un comportement semblable à la phase Nématique a également été observé pour les particules localisées au cœur du défaut. Cela pose la question de la nature du cœur du défaut.

Pour conclure, cette Thèse a montré que nous pouvons utiliser la dynamique comme une signature des transitions de phase des virus fd colloïdaux. La dynamique fournissent des informations détaillées sur le volume exclu des systèmes, autour de la transition de phase I-N et des transitions N-SmA et SmA-SmB. Par conséquence, nous pouvons mesurer la relaxation de ces dynamiques lorsque les transitions de phase se approchent, ainsi que la dynamique à la coexistence pour les transitions de phases N-SmA et SmA-SmB. La fonction de van Hove a été utilisée comme outil principal afin de caractériser les dynamiques. De plus, le fait que les bâtonnets fd soit un système si versatile nous a permis de jouer avec les différentes propriétés physiques des particules pour comprendre des systèmes complexes.

Contents

1

Acknowledgments

When 3 years ago I started my Ph.D., I truly did not imagine how much it would change my life. Not only from the academic point of view since I moved from a chemistry background to the experimental physics, but also personally. There are a lot of people that have been part of this amazing and challenging journey, and even in complicated moments they have stayed to support and help me, and for this reason, I would like to dedicate a few words to all of them.

First of all and foremost I would like to thanks my thesis advisors Eric Grelet and Pavlik Lettinga for their invaluable guidance during these 3 years. I am very grateful for all the time and effort that they have dedicated to me and for all what they have taught scientifically and also personally. They form an amazing team, complementing each other and without their feedback and help this Ph.D. would not have been possible. Once again thanks a lot to both of you. Indeed, it would be a pleasure to share again with them their experience and knowledge during my scientific career.

I sincerely thank my thesis committee Jörg Baschnagel, Patrick Davidson, Philippe Poulin and Rik Wensink for their feedback and discussion before, during and after my defense. They have been critical and helpful, and I felt very comfortable sharing my research with all of them.

Also, I would like to thank the ex-director Philipe Richetti and the current director Cécile Zakri of the CRPP. Thanks a lot to Béatrice Dupin, Elizabeth Hortolland and Corinne Amengual and Nathalie Touzé for making the bureaucratic and all kind of paperwork less complicated. Also thank Karen, Eric, and Ahmed for their help.

During this time between Bordeaux and Leuven, I could meet amazing people that, as me, were involved in a scientific career.

First, thanks to the people of my research group in Bordeaux with which I spent plenty of hours: Alexis, Marie, Baeckkyoung, Cheng, Lin, Anna, Andrii, Louis and Jérome. Special thanks to Alexis, the best colleague one can expect, I cannot say in words how much I appreciate your help since the first moment and also the good moments together. I hope science will reunite us again, otherwise, we will!

Thanks a lot to my group *Hakunis*. First starting with the Spanish crew, my small family that I will always carry in my heart whenever life brings me. The *gallegos*: Noe and Miguel (who supported me in the ups and downs during my first months in Bordeaux), Cintia my crazy old sister in Bordeaux, Maria and Sergio the best couple ever, and the always smiling Marina. The Catalan David and his zen spirit, from which I have learned a lot. The Vasques team: Jon, Leire. Thanks to Laura and Thomas for those relaxing days in Les Landes. Thanks to Noelia and Miguel and also Olaia and Alberto completing the Alvarez family. Then, my *international* Hakunis which indeed have lived this 3 years Ph.D. with me to the limit: Katerina for all the conversations, magic moments and her spontaneity and Magdalena for her inspiring courage and strength. Both of them are amazing women and friends for life. I should write another book to thank you all your presence during this 3 years (or during the last year for some of you), but you all know that my energy is always refiled when you are around. Thanks also to Eva,Alexandra, Petra, Aurelie, Marie, Franco, Marco, Carlotta, Armand, Laura, Theo and all the rest of people with I could share my time in the CRPP.

I would like to thank as well to my favorite musical couple Laure and Deniz, which have been always a boost of life and good vibes. Hope you can rock and roll for more and more years together!

In Leuven I could share office with amazing people such as Angelina, whose smile and laugh made days better, Tristan which always motivated me with his scientific questions, and Alessia Gennaro. Thanks you all for making my several stays in Leuven a good memory. I would like to thank also Michael Wübbenhorst, Patrick Wagner, Christ Blorieux and Carmen Bartic for their time and help.

Thanks to the people in Jülich, Manolis, Rafa and specially to Pancho and Oli. Thanks a lot to both of you for opening your house for me and making me feel part of your family. Oli, let our friendship last a lot of years, between labs and Irish beers, I hope we still have a lot to share! Thanks a lot for your inspiring personality and for all the good moments we spent together. And, of course, for all your help with our *friend* Matlab ;).

Also, I met such amazing people in the best summer school ever, which remain good friends now. Jerome Unidad or my Filipino bro, Xuan the happiest girl in the world and Charley aka Polly, which indeed has been one of the most important persons during this Ph.D. Thanks a lot for everything (too much to write down here), and please keep like you are, an amazing person!

Also, I met different and wonderful people that were not part of the scientific world but had an important impact in my life. Thanks to all my French family. Those who have chosen to stay with me, and share smiles, laughs and good times. Fabien, mon *petit frère* with whome I have shared the most intense moments, and supported me all the way throughout these 3 years. Remi et Marinne merci beaucoup pour rester avec moi pendant ce jolie aventure. Sans doute je garde votre amitié par toujours! Merci à Olive (père castor) et Sandra. Merci beaucoup aussi Guillame et a sa famille. Tu m'as soutenu la moitié du doctorat et spécialement pendant l'écriture. Espérons que on peut partager plus des années de bonheur ensemble, et peut-être que la science sera de plus en plus facile pour toi! Avec toi, tout est mieux et plus amusant. Je t'aime.

Je ne pouvais pas oublier ma petite famille de rugby du Stade Bordelaise. Merci de m'avoir reçu et de me faire partie du groupe dès le début. Mon français n'aurait pas amélioré sans votre aide. Ces 3 ans sans rugby auraient été un désastre. Merci, merci beacoup, J'espère pouvoir partager plus de rugby avec vous. Force et honneur!!

Then my two unique roommates in Bordeaux, Mariajo and Mariu. Two girls that have shared with me most of the craziest moments of my life and also part of the most difficult moments of my Ph.D. Gracias mi rubia y mi morena por estar ahí pase lo que pase!

There is a lot of people that I left behind at home when I left 3 years ago, but that every time that I come back they make me feel like nothing has changed and that no matter what happen, they will be always there. First thanks to Elena, Hugo and Sara. When we started 10 years ago the university we could truly not imagine where we would be now. Thanks for all the good moments and for being there also in the tough ones. Life is not easy, but together It gets better.

All the people that have held me and that support me when I left and they make me feel wonderful every time that I come back to Vigo: My rugby girls Gladis, Vanesa, Ana y Mariana. My good friends after all Efrén, Nahir, Nya and Jesús.

Also, there are people that I would like to see more often, but distance makes it difficult. Thanks a lot to Cristina, my *sister*, you always inspires me to be better and stronger. Gracias mi sister! Also to Irene Gómez, another person that rugby put in my life and made it better with her nice smile and positive energies. Thanks as to Dionisia and Ianina, two very special persons that I have meet before I started my PhD but were indeed important when I had to take important decisions.

Thanks to the people from Leuven: Cristina, Neele, Sara, Marie and the rest of the rugby girls. Also to my Belgium family: Jan, Astrid, Goele and Kathelyn. You have lived with me 6 months of intense writing but also nice moments, deep conversations and even we got some time to party! You are this kind of people that will remind always in my heart.

Angel, a very important person during my first year, without whom, I would probably be still lost. Thanks to my guard-angel.

Thanks to my professors in the USA who showed me how wonderful and exciting is the research world.

Thanks to all the people that have stayed there but also for the ones that are gone. We need to experience good and bad things that make us stronger. To take a path in life leads to important changes, but one has the control to choose how long to stay in that path and how the journey is going to be.

Finally, I would like to thanks my family. First, thank to my sister Irene and to her fiancé (finally) and good friend Agus, for they good moments and their support. Thanks to my parents, they have taught me everything they know in the best way possible. They have held me when worst times came, and when complicated decisions were in front of me. Their love is my strength. Os quiero.

L'homme se découvre quand il se mesure avec l'obstacle

Antoine de Saint-Exupéry.

2

Introduction

2.1 Overview

Liquid crystals are one of the best examples of the unique behavior of matter. As the name describes, they form intermediate states between the liquid and crystalline phases, that share important properties from both of them. First observed by Friedrich Reinitzer and later explained by Otto Lehmann [1], the molecular Liquid crystals have represented an important step in material science and technology, used as the Liquid Crystal Display (LCD). However, this phenomenon was also observed in colloidal particles.

Rod-like colloidal particles form different liquid crystalline mesophases, as shown in Fig.2.1. Zocher was the first to observe birefringent nematic tactoids of inorganic V_2O_5 rods in an isotropic background, in 1925 [2]. Later, not only the I-N phase coexistence was also reported in biological particles as the Tobacco Mosaic Virus (TMV) [3,4], but also the Smectic layered patterns formed due to the high monodispersity of the particles [5,6]. The phase coexistence between the Isotropic and Nematic phases observed experimentally, motivated Lars Onsager to develop a theory for first-order Isotropic-Nematic Phase transition of hard rods in his seminal work during 1949 [7].

Hard rods per definition cannot overlap, and only feel each other when they are in contact. Onsager demonstrated how highly anisotropic particles undergo a transition from the Isotropic liquid to the Nematic phase, which depends only on the maximization of the free volume. Particles in the Isotropic phase have neither positional nor orientational order, as opposed to those in the Nematic phase which have long-range orientational order but no po-

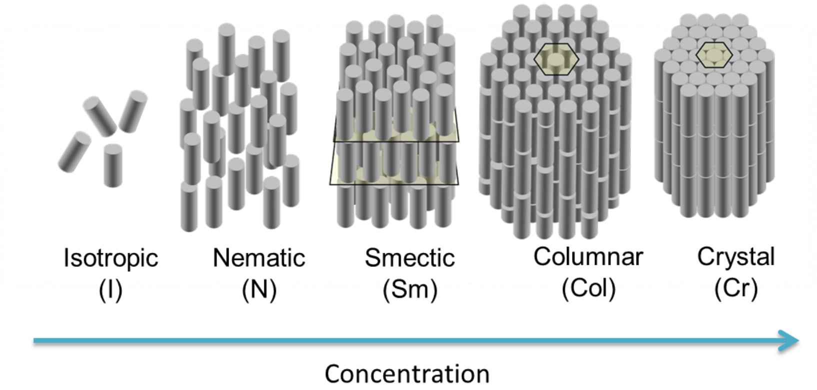

Figure 2.1: *Scheme of the different meshopases that hard rods form when increasing concentration, from the less concentrated (Isotropic) to the highest dense phase (Crystal) [19]*

sitional order. Through computer simulations, the work of Onsager was expanded to include the transition from the Nematic to the Smectic phase, where the particles gain 1D quasi-long-range positional order due to their layer confinement, being liquid-like within the layer [8, 9]. Transitions between these phases are purely entropy driven, which means that the excluded volume interaction between particles is enough to form the different mesophases. These kinds of systems are called colloidal lyotropic liquid crystals, and their phase transitions are concentration dependent. Moreover, rod-like particles are abundant in nature, e.g. the actin filaments, cytoskeleton and muscular proteins [10–12] that have a liquid crystalline-like behavior. These systems self-organize or diffuse in different ways, depending on their functions or even the changes in the medium. However, we are far from understanding some of the structures and mechanisms involved. One of the motivations for studying the dynamics and kinetics of these systems over the past decades was to understand the path that these systems follow to order and disorder [13–18].

In addition to the TMV viruses, the fd viruses were also observed to exhibit liquid crystalline mesophases [20], and due to their physical properties, they are considered an ideal experimental system to study the phenomena of phase transitions and self-organization of rod-like particles. The fdwt (wild type) is well known for the ability to infect *Escherichia coli* (E.Coli). As opposed to synthetic particles, they are naturally monodisperse, which favors the formation of the Smectic layers [21]. Moreover, the fd virus can be easily labeled with fluorescent dyes, thanks to the solvent exposed amines in their coat protein. Their physical properties can be tuned by genetic modification to obtain mutants with different lengths or stiffness. This is the case for the mutant fdY21M which is slightly longer than and much stiffer than fdwt. The fd virus high aspect ratio, L/D>100, makes the individual visualization with fluorescence microscopy possible. Also, the I-N transition of the stiff fdY21M virus takes place at the same volume fraction of the value predicted by Onsager [22]. Futhermore, they exhibit Brownian motion due to thermal agitation, first observed by Robert Brown in 1827 [23]. Thus, their dynamics that can be studied in order to understand the features of the different mesophases that they form and the underlying physics.

Since the phase transition implies a difference in the free volume between the liquid crystalline phases, it directly affects the self-dynamics of the system. Thus, of fd viruses dynamics have been extensively studied over the past decade for each distinct mesophase. In the dilute Isotropic phase, the rods have no positional or orientational order, causing a freely rotation and translation of the rods. Experiments and simulations have demonstrated that when approaching the I-N phase transition, the rotational diffusion freezes in the Isotropic phase [24, 25]. After the I-N phase transition, in the Nematic phase, the parallel translational diffusion is promoted, due to the alignment of rods along the long axis of the particles [26]. Later, it was found that self-diffusion of these rods in the Smectic phase occurs via mass transport between the layers, which is called hopping-type diffusion [27–30]. In this case, the particles jump between the layers, overcoming the layering potential, rather than staying within the layer. Thus, the rod-like viruses exhibit 1D diffusion confined in a potential energy background set by the Smectic layers. Although a big step has been taken towards the understanding of the dynamics of fd viruses in their different mesophases, the direct effect of the self-dynamics at these entropy driven phase transitions and in dense phases due to the change of free volume remain unclear. These will be the main questions treated in this Thesis.

2.2 Phase transitions in Liquid Crystals

The cascade of liquid crystalline phases exhibited by rod-like particles has been of great interest in the field of Soft Matter. In this section, we first introduce the theoretical work that Onsager developed on the Isotropic-Nematic Phase transition for hard rods. Second, we introduce the Onsager's theory for the Nematic-Smectic phase transition and also denser phases, which has been demonstrated with experiments and simulations.

2.2.1 Onsager's theory for an entropy driven Isotropic-Nematic Phase transition

Onsager developed the virial theory in the Isotropic-Nematic Phase transition for hard rod particles (1949). He established the theoretical basis for next generations in the field of colloidal liquid crystals. His work was motivated by the experiments of Zocher with the inorganic rod-like particles of V_2O_5, that exhibit Isotropic and Nematic phase coexistence [2] as well as for TMV viruses, observed by Bawden *et al.* in 1936 [4]. The work of Onsager is based on the maximization of entropy since he considered purely hard particles. When discussing entropy, we consider the definition given by Boltzmann [1], which refers to the number of accessible microstates of the system, which corresponds to the accessible volume.

Onsager developed a theory based on the second virial expansion of the free energy. The free energy has a contribution for an assembly of non-interacting rods, F_{ideal} and a contribution due to the excluded volume F_{exc}, where $F = F_{ideal} + F_{exc}$. Therefore, the free energy of a hard rods system expanded to the second virial factor can be expressed as

$$\frac{\triangle F}{Nk_Bt} = \frac{\mu^o(T)}{k_BT} + Ln(\Lambda^3\rho) + B_2\rho, \tag{2.1}$$

---

[1] To explain the behavior of macroscopic systems regarding the dynamical laws that rule their microscopic elements was the main motivation for Clausius, Maxwell, and Boltzmann in the 18th century. In his paper in 1877, Boltzmann presented a probabilistic expression for the entropy, where he showed that the entropy S is proportional to the 6N-dimensional phase space volume Ω occupied by the corresponding macrostate of an N-particle system, $S \propto log\Omega$. The second law implies to have an irreversible change in a closed system, the number of final states has to be larger than the initial state

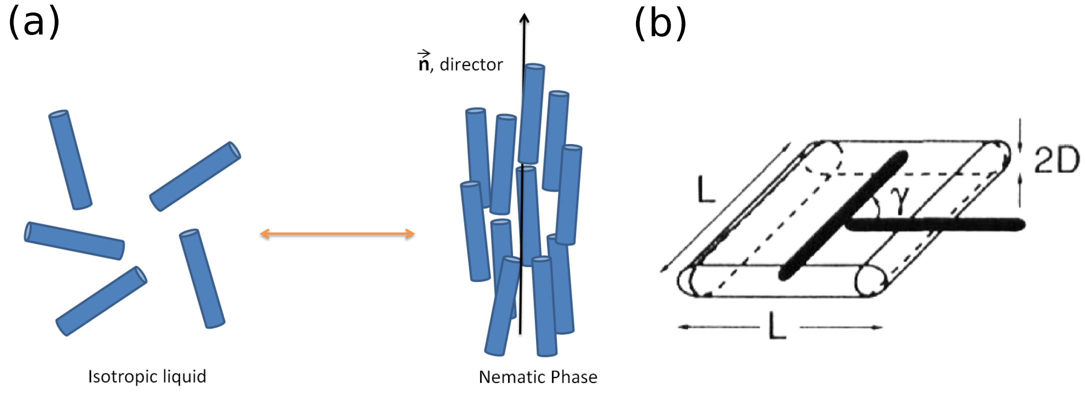

Figure 2.2: *a) Scheme of the Isotropic and Nematic phases. The particles in the Isotropic phase have short range positional and short range orientational order, while in the Nematic phase they have long-range orientational order and short range positional order. The arrow indicates that the transition is reversible by changing the volume fraction b) Excluded volume between two hard rods in the isotropic phase. [32]*

where, μ^o is the chemical potential of the solvent, Λ is the Broglie wavelength, ρ the rod particle density N/V, and B_2 is the second virial coefficient which is related to the intermolecular pair potential, in other words: the interaction between two particles. Since the second virial coefficient contains the interaction of two particles, it can be expressed as

$$B_2 = \frac{-1}{2V} \iint \Phi_1 \Phi_2 dr_1 dr_2, \tag{2.2}$$

where Φ represents the Mayer functions [31] for a pair potentials of two particles *1* and *2*. The solution of Mayer functions, Φ, depends on if the particles overlap or not, being -1 for overlapping particles and zero in the opposite case.

In the context of Onsager's hard rod system, where the Isotropic-Nematic Phase transition occurs (Fig.2.2), the contribution to the free energy is expressed as orientational distribution function $f(\Omega)$, which is the probability of finding a particle with determined orientation characterized by the solid angle Ω. In the Isotropic phase $f_{iso}(\Omega) = \frac{1}{4\pi}$, where all orientations are equally probable due to the possibility of the rods to rotate. Onsager reformulates the second virial coefficient using this distribution function for pair potentials between two hard rods given by:

$$B_2 = \frac{1}{2}\iint d\Omega d\Omega' f(\Omega) f(\Omega') v_{excl}(\Omega\Omega') \tag{2.3}$$

where $V_{excl}(\Omega\Omega')$ is the excluded volume between two spherocylinders with orientations Ω and Ω' which can be written as

$$V_{excl}(\Omega, \Omega') = 2L^2 D|sin\gamma| + \frac{4}{3}\pi D^3 + 2\pi L D^2, \tag{2.4}$$

where $\gamma(\Omega, \Omega')$ is the angle formed between two adjacent rods, D the diameter and L the length. Onsager considered the particular case of infinite long rods, where the aspect ratio is $L/D >> 100$. If the rods are completely parallel the excluded volume is minimal $V_{excl}^{\parallel} = 2\pi L D^2$ (Nematic phase) and maximal if they are perpendicular $V_{excl}^{\perp} = 2L^2 D$ (Isotropic phase).

Knowing the orientational distribution function, the orientational order parameter S can be determined,

$$S = \frac{1}{2}\langle 3\cos^2(\theta) - 1\rangle \tag{2.5}$$

where $\langle ... \rangle$ indicates the average and θ the angle that the particle orientation forms with the director. If all particles are oriented along the director unit vector **n** (unit vector that represents the preferred orientation of the particles in the phase, see Fig.2.2), then $\theta = 0$ and $S = 1$, while for particles which have a random orientation $S = 0$.

At the I-N Phase transition then $F_{exc} \propto \frac{L}{D}\phi$. Therefore, the formation of a liquid crystalline phase as the phase transition depends only on the volume fraction of the system ϕ. For flexible rods, an approach has been used [33], where the excluded volume is less than for hard rods due to their partial deformability. It follows that, within the Onsager theory, the volume fraction of hard rods at the I-N phase transition scales as $\phi = 4\frac{D}{L}$. When increasing volume fraction, the excluded volume becomes very small for parallel rods, the free volume in the system must increase. This way, when there is a transition from the isotropic which involves a loss of orientational entropy, it is compensated by the gain of translational entropy. Onsager determined with his theory that the Isotropic-Nematic Phase transition of thin and long hard rods is a first order phase transition and purely entropy driven when the aspect ratio of rods is higher than 100. For smaller aspect ratios, third or higher virial terms need to be taken into consideration for the free energy expansion.

To find the Isotropic-Nematic Phase boundaries, the free energy is minimized with respect to the orientational distribution function as a function of concentration. Thus, the volume fraction of both phases at phase coexistence is obtained numerically using the correct distribution functions [34]:

$$\phi_{I(-N)} = 3.3\frac{D}{L}, \quad \phi_{(I-)N} = 4.2\frac{D}{L}, \quad S = 0.79 \tag{2.6}$$

The low packing density of thin rods or fibers in comparison to that of spheres is explained due to the number of rod contact per rod [35].

The ideal theoretical particle does not exist in nature; therefore different considerations need to be taken into account for the study of experimental systems. Extensions of Onsager's theory were done for the case where the particles are not completely rigid but have a persistence length P,

$$P = \frac{B_s}{k_B T} \tag{2.7}$$

where B_s is Young's modulus and measures the capacity of deformation. Flexibility destabilizes the Nematic phase. Thus, the I-N phase transition for flexible particles is found at higher volume fraction values, and there is a decrease of the order parameter at the phase coexistence.

Since many colloidal particles in solution are stabilized by the charge repulsion, another extension that has to be applied to the theoretical model of Onsager is the charge on the particle surface. Onsager has introduced the concept of the effective diameter (D_{eff}) of a charged particle, which is bigger than the bare particle diameter. First simulations were performed by Khokhlov and Semenov in 1982 [36] and later Chen [33] predicted the isotropic-nematic coexistence concentrations accurately for hard, semiflexible, polymers, $c_I = 4.7/b_{eff}$

and $b_{eff} = \pi L^2 D_{eff}^{iso}/4$. The increase of the D_{eff}, leads to a decrease of the aspect ratio, and to an increase of the volume fraction needed to form a liquid crystalline phase [34,37].

2.2.2 Nematic-Smectic Phase Transition

When increasing the volume fraction or rod density, liquid crystals formed by monodisperse rod-like particles exhibit a transition to a higher ordered phase called Smectic phase. In this phase the particles are located in periodic layers, exhibiting long range positional order in 1D and short range positional order (or liquid-like behavior) within the layers.

The fact that Smectic ordering was observed for TMV at low concentrations (3 wt%) only due to electrostatic repulsion interactions was surprising, and it caught the attention of researchers in the 80's. The theory developed by Onsager of the effect of the excluded volume was applied to explain the phase transition that occurs from the Nematic phase to the Smectic phase. Hosino in 1979 developed a second virial approximation theory for the Nematic-Smectic phase transiton [38]. He showed that the Nematic-Smectic-A is a second order phase transition when fluctuations of the director are not taken into account or very weak first order otherwise. Wen and Meyer [39] proposed that the appearance of smectic layers is driven by the decrease of lateral packing density of the rods within the layers, compensating the entropy loss involved in the layer ordering, again due to an effect of excluded volume. The same year, Mulder shows theoretically and compared with simulations, that smectic order occurs purely due to packing effects caused by short-range repulsions [40] Then Frenkel and Stroobants in their simulations in 1988 [41,42] demonstrated that the N-Sm phase transition for short rods ($L/D \simeq 5$) it is purely entropy driven, undergoing a stable Smectic phase. Later, simulations for hard spherocylinders of infinite aspect ratio L/D were performed in 1997 by Polson and Frenkel [9], where they showed that N-Sm phase transition was first order. Even though there were different opinions about the order of this phase transition, it has been accepted that for freely rotating hard long rods the Nematic-Smectic phase transition is first order.

The Smectic phase has been observed in suspensions of stiff monodisperse rod-like particles like TMV and silica-coated boehmite rods [43, 44], and also in the semiflexible fd viruses [21]. Indeed, flexibility is a factor that affects the concentration at which the the Nematic-Smectic Phase transition occurs. In the same way that it was observed for I-N Phase Transition, simulation and experimental studies agree that flexibility shifts the N-Sm phase transition, destabilizing the formation of Smectic-A phase for flexible rods, and also decreasing the layer spacing. Experiments performed by Pouget *et al.* [29] and Grelet [19], compared the flexible fdwt with its stiff mutant fdY21M, showing that the effect of flexibility shifts also the N-Sm phase transition. These results were supported by theory and simulations [8]. The volume fraction for the N-Sm phase transition depends on the approximations done (i.e., if the rods are parallel or freely rotating), varying from 0.36 to 0.47. Kuijk *et al* [45] showed that the phase behavior of silica rods with an aspect ratio (L/D) smaller than 8, exhibits Isotropic-Nematic and Smectic phases. Later experimental work showed that for fd viruses, Smectic-B mesophase could also be formed, in which the particles have hexagonal long range positional order within the layer [19].

Different studies [46–49] have proved that monodispersity is a key feature for the formation of the Smectic phase. It has been reported that, when the polydispersity of the system increases, a hexagonal columnar phase is favored rather than the Smectic lamellar phase [5]. Stroobants showed with simulations how the bidispersity of the rods favors the Nematic-Hexagonal columnar phase transition rather than the Nematic-Smectic phase transition, supported later by more simulations [49].

In the next sections, we will show how the dynamics of the particles is influenced by these phase transitions or even how dynamics cause them to occur, as well as by the structure of each mesophase. Prior to that, we will take some time to introduce the general theory for the diffusion equation of rods and their dynamical features.

2.3 Self-diffusion Equation for rods and diffusion coefficients: from semi-dilute Regime to high concentrated phases

Colloids exhibit the very well-known Brownian motion, due to thermal agitation, first observed by Robert Brown in 1827 [23]. This motion originates from thermal agitation of the order of a $k_B T$ per solvent molecule, which was demonstrated by Einstein in 1906 [50]. In nature, we find a lot of examples of anisotropic particles which exhibit Brownian motion,

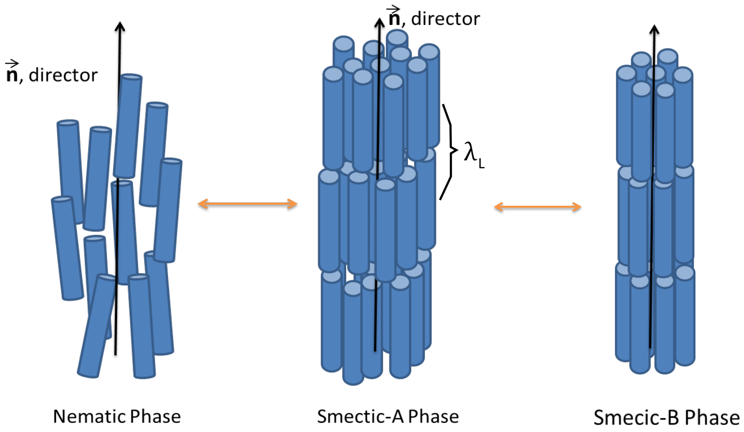

Figure 2.3: *Scheme of the Nematic and the Smectic mesophases for a system of hard rods. In the Smectic phase the particles gain position quasi long range order in 1D forming the Smectic layers.* λ_L *indicates the layer spacing.*

like DNA, proteins. This motion in most cases occurs in crowded environments which make dynamics more complex.

The diffusion of rod-like particles does not only have a *translational component*, but also a *rotational component* with respect to the symmetry axis of the particle, corresponding to the positional and orientational degrees of freedom. The diffusion is concentration dependent, as increasing the volume fraction the free volume decreases, decreasing the space available for diffusion [51, 52].

At infinite dilution, we consider a single Brownian rod-like particle j, for which the orientation varies from $\hat{u}_j(0)$ to $\hat{u}_j(t)$, and the centre of mass changes from $\vec{r}(0)$ to $\vec{r}(t)$ (Fig.2.4a). This change of position and orientation is due to the thermal energy equal to k_BT, while at the same time we need to consider the friction that a particle feels when moving throughout a solvent. Considering the friction coefficients and the equation of Stoke-Einstein, for long thin rods, the diffusion coefficients at infinite dilution are given by

$$D^0_\parallel = \frac{k_BTLn(L/D)}{2\pi\eta_0 L}, \quad D^0_\perp = \frac{k_BTLn(L/D)}{4\pi\eta_0 L} \tag{2.8}$$

where η_0 is the viscosity of the solvent and L/D is the aspect ratio of the rod, with length

L and diameter D. Hence, for the perpendicular motion the friction constant is twice larger as for parallel motion. Knowing that $D_{\perp} = (1/2)D_{\parallel}$, thus the total *translational diffusion* is

$$D_t = \frac{1}{3}[D_{\parallel} + 2D_{\perp}] = \frac{k_B T ln\{L/D\}}{3\pi\eta_0 L} \tag{2.9}$$

For the rotational diffusion coefficient,

$$D^0_{rot} = \frac{3k_B T Ln(L/D)}{\pi\eta_0 L^3} \tag{2.10}$$

From these equations, we can conclude that the friction is reduced if we increase the aspect ratio or the rod. If we imagine these rods as a chain of single beads, we can imagine that first bead will decrease the effect of friction in the second bead that follows, which is called the hydrodynamics effect. When we have rods with a finite length, this effect decreases.

At higher concentrations, the interaction between particles needs to be taken into account. This is done by defining the equation of diffusion of the probability density function of an ensemble of rods as $P(\mathbf{r}_1,...\mathbf{r}_N,\ \hat{\mathbf{u}}_1,...\hat{\mathbf{u}}_N,t)$. The equation of diffusion for the probability density function P of these phase space coordinates can be found from the exact conservation,

$$\frac{\partial}{\partial t}P(\mathbf{r}_1,...\mathbf{r}_N,\hat{\mathbf{u}}_1,...\hat{\mathbf{u}}_N) = -\sum_{j=1}^{N}\{\nabla_j \cdot [v_j P] + \hat{R}_j \cdot [\Omega_j P]\} \tag{2.11}$$

where $[v_j$ is the translational velocity and Ω_j the rotational velocity. Finally, we get

$$\frac{\partial}{\partial t}P = \sum_{j=1}^{N}\{\frac{3}{4}D^0\,\nabla_j \cdot (\hat{\mathbf{I}} + \hat{\mathbf{u}}_j\hat{\mathbf{u}}_j) \cdot [\nabla_j P + \beta P \nabla_j \phi] + D^0_r \hat{R}_j \cdot [\hat{R}_j P + \beta P \hat{R}_j \phi]\} \tag{2.12}$$

where $\hat{\mathbf{I}}$ is the identity matrix. This is the *Smoluchowski equation* for very long and thin, rigid rods, where hydrodynamic interactions are neglected. The index 0 indicates that we consider

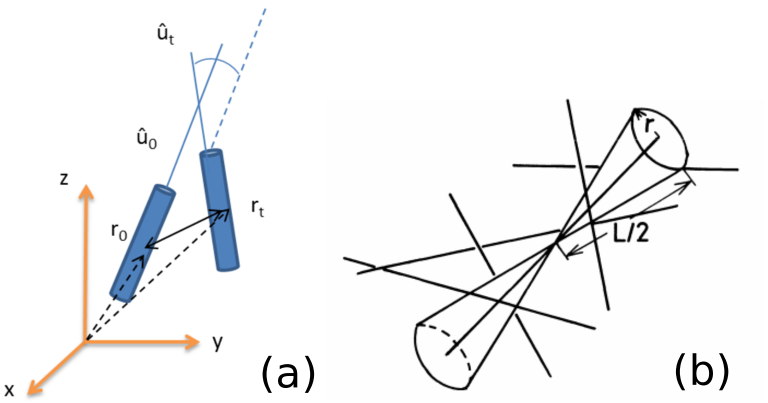

Figure 2.4: *a) Rod-like particle translational and rotational motion. The initial and final orientations of the rod are u_0 and u_t respectively and r_0, r_t are the initial position and final position. b) Interacting rods in the semi-dilute regime [51].*

the case of infinite dilution for which the diffusion coefficients are given by Eq. 9 and 10. Note that we will always consider equilibrium on the colloidal time-scale. For infinite time $t \rightarrow \infty$, when the suspension attains equilibrium, the probability density function P is proportional to the Boltzmann exponential $\beta\phi$ and $\partial P/\partial t = 0$.

The *translation motion* of a particle in a time t can be measured knowing its initial position. This is described by the conditional probability density function (pdf), which is the probability for a particle to diffuse a given distance at time t. For a Brownian particle, when there is no external force acting on the colloid, positive or negative displacement can occur with the same probability. If we consider a single particle at infinite dilution such that interaction potential can be neglected, then:

$$\frac{\partial}{\partial t}P(r,t) = {D^0}_{t,S}\,\nabla^2 P(r,t) \qquad (2.13)$$

As aforementioned, since random motion has no preferred direction, we square the average displacement over all particles; otherwise the average displacement would be zero. The *Mean Square Displacement*, is defined from the trajectories r_j of the diffusing particles (labelled with index j) in terms of the distance from the initial position $r(0) = 0$ as:

$$MSD(t) = \langle r^2(t) \rangle = \frac{1}{N} \sum_{j=1}^{N} (r_j(t) - r(0))^2 \tag{2.14}$$

$\langle ... \rangle$ being the average over all particles and N the total number of particles. If we use equation 2.13, we average over the pdf,

$$\frac{d}{dt} \int drr^2 P(r,t) = D^0_{t,s} \int drr^2 \bigtriangledown^2 P(r,t) \tag{2.15}$$

where Gauss's integral theorem has been used twice in the second line and $\bigtriangledown^2 r^2 = 6$ in three dimensions, 4 in two dimensions and 2 in one dimension. Hence

$$MSD(t) = a2D_s t^{\gamma} \tag{2.16}$$

where a defines the dimension of the system, and γ is the diffusion exponent. When $\gamma \sim 1$, the self-diffusion has a Brownian (diffusive) behavior, while $\gamma < 1$ is characteristic of a subdiffusive regime. Anomalous subdiffusive events have been observed in systems near glass transition of spherical colloids [53] a cage effect is observed. Moreover, the same behavior is present in most biological systems (i.e. diffusion of proteins) [54], transport in porous media [55] or the so called free energy landscape systems [29,56]. The value of D depends on the interaction with other rods or if there is any obstacle in the way.

The *rotational diffusion coefficient* D_{rot} is obtained by measuring the orientation of a particle at time t, $\hat{u}_j(t)$, knowing the initial orientation $\hat{u}_j(0)$. The angle between $\hat{u}_j(0)$ and $\hat{u}_j(t)$, is calculated using P($\hat{u}_j$|$\hat{u}_0$), the so-called conditional probability density function, which gives the probability that a particle has an orientation û at time t, given that it had orientation $\hat{u}_0$ at $t = 0$. This function correlates the orientations of the particles at different times. The orientational ordering in the system is set by P($\hat{u}_0$), which is peaked around the director $\hat{\mathbf{n}}$, when the rods are in the nematic phase. The ordering of the system is characterized by the square cosine of the angle Φ between the rod, û$_0$, and the director n̂ defined by

$$\bar{P}_2 \equiv \langle P_2(\Phi) \rangle = \frac{1}{2}\{3\langle \cos^2(\Phi) \rangle - 1\} \tag{2.17}$$

where $\theta = \mathbf{n}.\hat{\mathbf{u}}$ is the angle between the molecular axis and the director and $P_2(x)$ is the second Legendre polynomial. Thus, $\bar{P}_2$ is de order parameter which measures the degree of order, and it is 0 for an isotropic state and equal to 1 for a perfectly aligned state. For a system of rods without orientational order P(û$_0$) $= \frac{1}{4\pi}$. We now derive the time dependence of the orientation of a single particle, again using Eq.2.12 omitting the torque term, such that

$$\frac{\partial}{\partial t} P(\hat{\mathbf{u}}, t) = D^0{}_{\hat{\mathbf{u}},S} \hat{R}^2 P(\hat{\mathbf{u}}, t) \tag{2.18}$$

Hence, for a system with no orientational order, the *Mean Squared Angular Displacement* is

$$MSAD(t) = \frac{2}{3} exp(-6D^0{}_{r,S}t) \tag{2.19}$$

Finally, we can re define the evolution of the order parameter for a single particle:

$$\bar{P}_2 = \langle P_2(\Phi_t) \rangle) = \frac{1}{2}(3\, MSAD(t) - 1) = \frac{1}{2}\{3\langle \cos^2(\Phi) \rangle - 1\} = exp(-6D^0{}_{r,S}t) \tag{2.20}$$

We derived the equations for the translational and rotational motion, by omitting the interaction terms. In principle, the full collective translational and rotational diffusion can be calculated from the Smoluchowski equation. In this thesis, however, we will focus on the self-diffusion of rods, which is a good measure of the available free volume. The accessible volume of the system plays a significant role in the dynamics. Thus, when increasing the volume fraction, the rotational diffusion "freezes", as Russo *et al.* demonstrate for the TMV [57–59]. However, it is important to distinguish between the self-diffusion D_i^S and the collective diffusion D_i^C. It has been proved that in the Isotropic phase the self-rotational diffusion of the particles decreases as increasing concentration which does not reach zero, contrary to the collective diffusion. [60, 61].

A further step to explain the motion within an entangle of rods in the semi-dilute regime where $L^{-3} < v < d^{-1}L^{-2}$ was done by Doi in 1975 [51]. He developed the first successful theory to explain the diffusion of rods in a concentrated rod dispersion. He assumed that a really thin rod in an isotropic packing of rods could diffuse freely in the direction of the rod axis. Its rotational motion, however, is highly restricted by neighbor rods (Fig.2.4b). This confinement can be visualized, when one considers a sphere of radius $L/2$ centered on the middle-point of the test rod, and project all the other rods intersecting the sphere on the surface of this sphere. Thus, at short times the rotating rod can probe a surface S and is thus effectively confined in a tube with radius $a = \sqrt{S}$. The confining tube is given by the maximum angle a/L and the free rotational motion $(a/L)^2/D_r^0$. When the rod diffuses throughout its tube, it can only rotate by a/L. A rod can only get out of its confining tube when it diffuses at least $L/2$ along its axis, or when one of the other confining rods does. When the rod diffuses out of its tube, it can only rotate by an angle a/L. The overall rotation of the rod is attained by the repetition of these jump steps, hence

$$D_r \cong (a/L)^2/\tau_1 \cong a^2 D_{\|}/L^4 \tag{2.21}$$

where τ_1 is the persistence time, assuming that translational diffusion along the axis is unhindered. The size of the tube a can be estimated with the probability that two cones with radius r if the base circle does not contact with the randomly placed thing rods, giving $a \cong 1/cL^2$, where c is the concentration. Thus, assuming that $a << L$, the rotational diffusion is

$$D_r(\phi)/D_r^0 = \beta(v/L^3)^{-2} \tag{2.22}$$

The interest to understand the diffusion in the liquid crystalline phases of rod-like particles in isotropic and semi-dilute has motivated extensive experimental dynamical studies, such as experiments with F-actin filaments in isotropic and semi-dilute regime phases [62], silica rods [45] and the filamentous fd viruses [19, 28, 63, 64]. However, there are some issues like the coupling between the translational and rotational diffusion and the effect of the flexibility of the particles that should be addressed and which play an important role to understand the diffusion of rods in semi-dilute and dilute regimes.

2.3.1 Self-Van Hove function as a robust method to quantify dynamics

The dynamical equivalent of the radial distribution function $g(r)$ is the van Hove distribution function $G(r,t)$ [65–67]. It is a conditional real-space dynamical correlation function to characterize the spatial and time distributions of particles in a fluid [68]. It gives the probability of finding two particles at a distance r at time t , given that at time $t = 0$ they were at distance r,

$$G(z,t) = \frac{1}{N}\langle\sum_{i=1}^{N}\sum_{i\neq j}^{N}\delta[z+z_j(0)-z_i(t)]\rangle \tag{2.23}$$

where $\langle ... \rangle$ represents the average over all particles, i and j are two different particles, and δ is the three dimensional Dirac delta function. Then the van Hove function can be split in two terms, the *distinct* part where $i \neq j$ and the *self* part of the van Hove function where $i = 1$ for a single particle,

$$G_s(z,t) = \frac{1}{N}\langle\sum_{i=1}^{N}\delta[z+z_i(0)-z_i(t)]\rangle \tag{2.24}$$

$G_s(z,t)$ describes the conditional motion of the particle that was initially at the origin. Generally, for Brownian particles, it has the shape of a Gaussian function that smears out with time [69], as we show in Fig.2.5. The self-van Hove function $G_s(z,t)$ has been used to study dynamics around the glass transition, where the shape is not Gaussian anymore but turns out to be a Lévy-flight distribution where $P \sim exp^{(-|x/x_0|^{\beta})}$ [53,70]. The Lévy-flight distribution is characteristic for heterogeneous dynamics typical of the glass state. Furthermore, for particles that diffuse in a periodic potential background, the self-Van Hove function is affected showing distinct peaks due to potential barriers, as shown by Dalle-Ferrier *et al.* [71]. This is also the

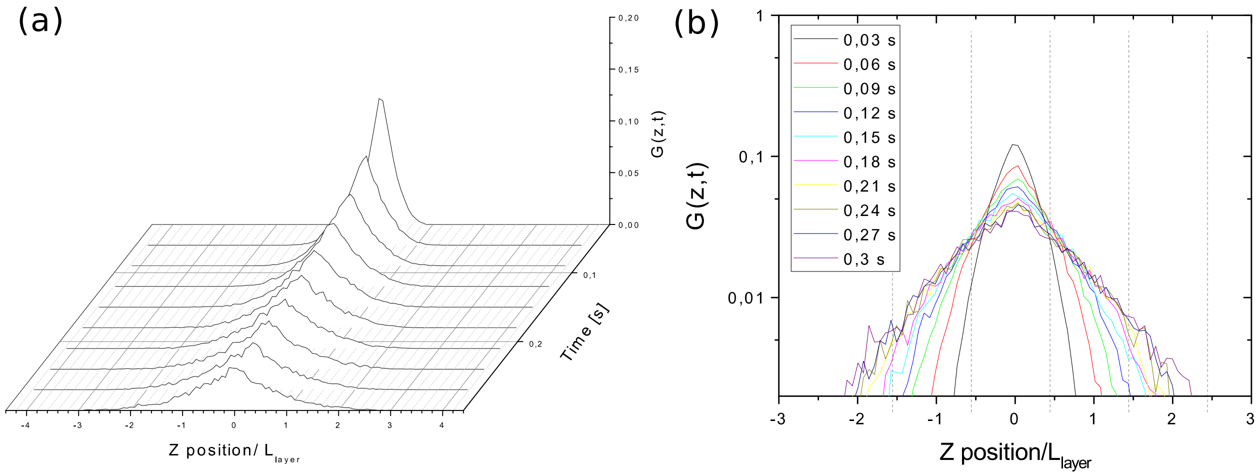

Figure 2.5: *a) 3D representation of the G(z,t) as a function of time and position. The probability density function decreases with time as the particle diffuses from the first position. b) Log-linear representation of the self-van Hove function as a function of time. The different colors indicate different time steps. The position is normalized by the length of the rod.*

concrete case for the already mentioned jump-like diffusion [29, 72]. Hence, the change of shape of the self-van Hove function provides important dynamical and structural information of the system.

2.3.2 Theoretical background for the analysis of the self-van Hove function: study of diffusivity

For Brownian colloidal particles, the general approximation is to assume that $G_s(z,t)$ it is Gaussian [69]

$$G_s(z,t) = (4\pi D_t t)^{-3/2} exp(-\frac{z^2}{4D_t t}) \tag{2.25}$$

The change of shape of the self-van Hove function can be characterized to distinguish the type of diffusion that the system exhibits. In this thesis, we use a method to analyze the self-van Hove function developed by Wouter den Otter (the University of Twente, private communications). This method quantifies the deviation from the Gaussian behavior with the shape of the self-van Hove function, as well as the Gaussian behavior itself. Thus, from the probability density function G(z,t) represented in Fig2.5b,

$$G(z,t) = \frac{G_0}{\sqrt{t}} exp - (\frac{\Delta z}{t}) \tag{2.26}$$

the probability $G(z,t)$ is rescaled by the $\sqrt{dt}$ and the position by $z/\sqrt{dt}$ to cancel the effect of time and to represent the squared position z^2

$$\sqrt{t}G(z,t) = G_0 exp - (a_1 \Delta z^2) \tag{2.27}$$

Next, we plot the $Ln(G(z,t) * \sqrt{dt})$, such that for in case of a purely diffusive process all curves are linear.

$$ln(\sqrt{t}G(z,t)) = lnG_0 - (a_1 \Delta z^2) \tag{2.28}$$

and fit it by

$$Ln(G(z,t)\sqrt{dt}) = a_0 - a_1(\triangle z^2)^{a_2}; \tag{2.29}$$

The parameter a_1 measures the slope of the normalized self-van Hove function, while the a_2 is the exponential parameter. Hence, after the normalization of the self-van Hove function, we observe that the linear function is characteristic for Gaussian behavior ($a_2 = 1$), while the exponential decay function ($a_2 = 0.5$) corresponds to Lévy-flight. Thus, equation 2.25 is valid only when $a_2 = 1$ and in this case a_1 is proportional to D_t. We use this method to quantify the a_2 parameter which measures the deviation from the Gaussian behavior. In Fig.2.6 we show the simulations provided by Wouter den Otter (University of Twente, private communications),

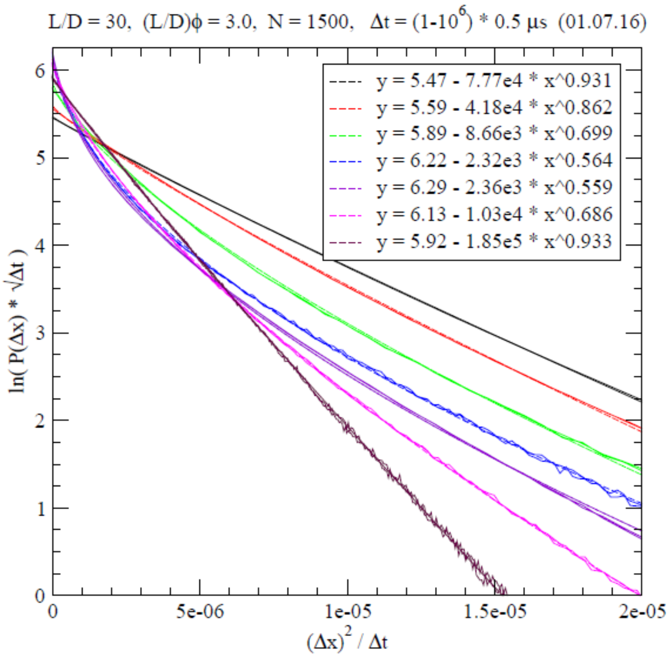

Figure 2.6: *Simulation of the rescale and fit self-van Hove function with Wouter de Otter, private communications) The curves are the self-van Hove function at different dt normalized and fit with Eq.2.29. The linear lines correspond to Gaussian behavior,* $a_2 \cong 1$ *while the exponential decays is related with the diffusive heterogeneity* $a_2 \cong 0.5$.

obtained from a self-van Hove function at different times, which goes from Gaussian behavior (linear) to Lévy-flight (exponential decay), and it recovers again to Gaussian.

All this quantitative information (MSD, diffusion coefficient and exponents, and self-van Hove function) is the result of the analysis of previous qualitative results, which have been collected using the single particle tracking. The single particle tracking is a tool to study the dynamics at individual particle scale or also called *self-dynamics*. The advantage of the single particle tracking is that individual particles can be observed even when they are dispersed in a host system consisting of identical or different non-labelled particles. In addition to the mean square displacement of the center of mass of the rod, also the orientation can be followed. Hence, the position and orientation of single particles at every point in time are known, and one is free to choose the kind of correlation function that is used to determine the rotational diffusion coefficient. This is in contrast to techniques such as Dynamics light scattering (DLS) or fluorescence recovery after photobleaching (FRAP) where only second moments are measured, and they provide no information about the deviation from the Gaussian behavior [44]. Moreover, it is not only possible to independently measure translational and rotational diffusion, but also to see how they are correlated. We consider that the self-dynamics is related to the available space or *free volume*, and it can be a probe for the entropy of the system [73, 74]. However, a suitable experimental system and method to explore the complexity of dynamics in the different liquid crystalline mesophases is needed.

2.4 fd filamentous bacteriophages as a hard rod model colloidal system

In previous sections, we have introduced the theoretical model for colloidal hard-rods, their phase transitions and the dynamics of the rod-like particles from dilute to the semi-dilute regime. However, the ambition to find an experimental system to test this theoretical model has always motivated researchers to explore different types of colloidal dispersion. One of the main goals is to connect order and dynamics.

In biological systems, we can find many different and complex filamentous ordered systems (cytoskeleton, actin filaments, DNA or TMV) which can also form liquid crystalline phases. These crowded systems and the way they ordered were poorly known, despite the important role that they play in nature. One of the ways for understanding the ordering of these systems is by using the hard rod model of Onsager through the maximization of entropy.

the fd viruses are an excellent experimental model of anisotropic colloidal particles and consistent with the previously described theoretical predictions. Their easy production, their versatility to be functionalized (with polymers and dyes) and their physical properties, make them a perfect model system as a lyotropic colloidal liquid crystal [20, 75]. Moreover, it has been widely studied in molecular biophysics [76, 77].

In this section, we will give details about the morphology, phase diagram and dynamics of the fd-viruses in their different liquid crystalline mesophases which are the experimental colloidal system used in this thesis.

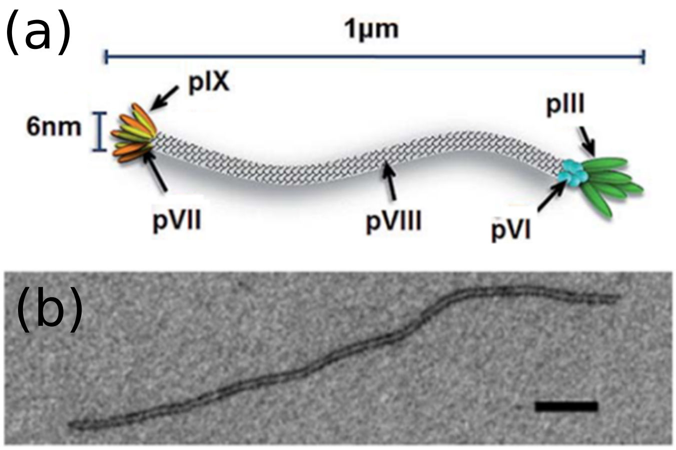

Figure 2.7: *a) Structure of fd viruses and the forming proteins [85] b) TEM image of fd virus [29].*

2.4.1 Morphology of the fd viruses

The fd virus, together with M13, belongs to a group of closely related filamentous, male-specific coli phages. It is formed by a circular single-stranded DNA chain covered by the main coat protein and consists of 6408 nucleotides. It has only 8 genes which are responsible for the codification of the proteins of the virus. [78–80]. The process of infection *Escherichia coli* is done through the adsorption of the p2 protein to the host receptor, which is the tip of the F-pilus [81, 82]. The ssDNA encodes three classes of proteins: *replication* (pII, pX and pV), *morphogenetic* (pI, pIV and pXI) and *structural* (pVIII, pIII, pVI, pVII and pIX) proteins, as shown in Fig.2.7. Although filamentous bacteriophages do not have a membrane, the major coat protein (pVIII) is present in the viral lifecycle [83, 84]. Proteins pIII and pVI are located at one extremity of the virus pVII and pIX in the other.

The coat protein pVIII has around 2700 copies of identical structural subunits, and it forms an α-helix structure with 50 amino acids, of which only the 20 first are hydrophilic and solvent-exposed [86], which determines the surface properties. The charge surface density is approximate 10 e^{-}/nm at $pH = 7.5$ as a result of the location of the two amino groups (NH_2) and five acidic residues (COOH) in the solvent exposed part. [87] and its isoelectric point (IEP) is 4.2.

The fdwt virus is about 880 nm in length (L) and 6.6 nm in diameter (D) [12], having an aspect ratio (L/D) bigger than 100. The persistence length (P) or stiffness is around 2.2 μm, being 2.5 times its contour length. The Molar Weight (MW) of fdtwt is $1.62x10^7$ g/mol. The virus absorbs in the UV's spectra at 269 nm with an extinction coefficient (ε) of 3.84 cm^2/mg. The fact that by genetic modification the physical properties such as length and stiffness change makes this particle a versatile system to study. The result of these modifications is the so-called mutants, which have different physical features compared to the wild-type. In this thesis, we will focus on fdY21M and M13KO7 mutants.

The *fdY21M* only differs by one aminoacid from fdwt: the tyrosine in the 21st place is replaced by a methionine in the pVIII inside coat protein [88], which is not solvent-exposed. This change has a direct effect on the morphology of the virus. The length $L = 0.92\mu m$ is bigger than for *fdwt*, as well as for the persistence length $P = 9.9\mu m$ [22], which makes the mutant fdY21M stiffer. The molar weight is slightly different being $1.63x10^7$ g/mol and the UV absorption changes to 3.63 cm^2/mg at 269 nm.

The *M13* virus differs only from fdwt by the substitution of one charged for one neutral amino acid per virus coat protein. This is the Aspartic acid in the 12th position of the pVIII of the fdwt, which is replaced by the Asparagine. This time the amino acid replaced is exposed to the solvent, and the surface charge of the virus is affected, decreasing up to 7 e^-/nm at $pH = 7$. On the contrary the length, diameter and molar weight are not affected by this modification [89]. One of the most known mutants of M13 is M13KO7, used as helper phase for bacterial infection [90]. It consists of M13 phage with a Kanamycin resistance gene added to the genome. The only difference for this mutant is the length $L = 1.2$ μm.

The characterization of these viruses can be performed by TEM (Transmission Electron Microscopy) and measure the average length, but also by gel electrophoresis. This is possible due to their different surface charge [89]. However, the most precise way to characterize each virus is by DNA sequencing, which determines the precise order of nucleotides (including the genetic modification for each mutant).

2.4.2 Phase behavior of fd viruses

The *isotropic-nematic* phase transition of fd viruses was first studied by Purdy and Fraden [89]. They investigated the ionic strength dependence of the location of the phase transition. These experiments allowed them to compare this experimental system to the Onsager's theory. These

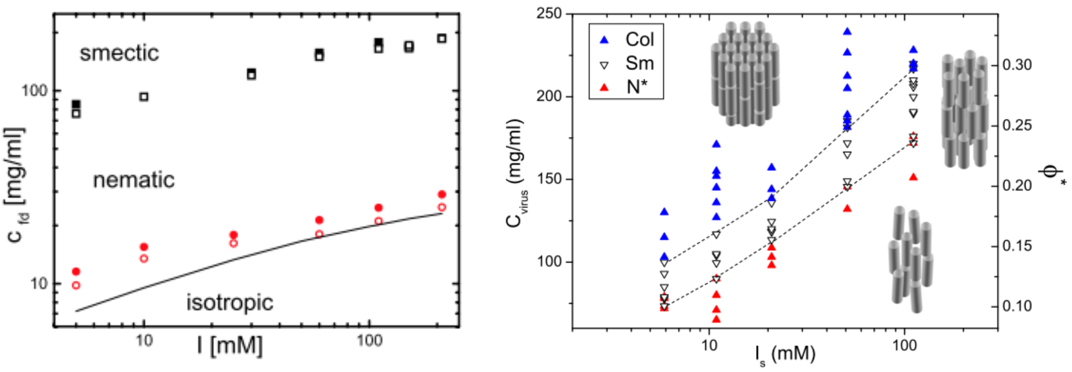

Figure 2.8: *(Left) Phase transitions for suspensions of fd as a function of ionic strength. The isotropic-cholesteric transition is indicated by the circles, with the open circles the coexisting isotropic phase. The cholesteric- smectic transition is indicated by the squares with the open symbols the highest measurable nematic phase concentration. The solid line is the second virial theoretical prediction for coexisting isotropic phase for charged semi-flexible rods [33] with* $L/P = 0.4$ *[91]. (Right) Experimental phase diagram of the dense phases showing the N-Sm and Sm-Col as a function of ionic strength [19]*

studies on ionic strength dependence were also performed for N-Sm and Sm-Col phase transitions, as shown in Fig.2.8. Moreover, the flexibility has a strong influence on the location of the I-N phase transition. Decreasing the flexibility of the particles, the concentration at which the I-N transition occurs decreases, as shown by Barry *et.al* [22]: the coexistence concentration at a fixed Ionic strength of $110mM$ is $19.8 - 22.6\ mg/mL$ for fd and $13.9 - 18.9\ mg/mL$ for fdY21M.

Due to the chirality of fd virus, in the Nematic phase particles are not just aligned along the director, but also the director rotates forming a helix. The characteristic texture for this behavior is the *fingerprint* from which they are able to measure the *pitch* P_0 [92]. This pitch decreases with concentration, as shown in Fig.2.9. Thus, the nematic phase is called *chiral-nematic* phase, and it has been first observed by Lapointe and Marvin during 1973 [93]. Dogic and Fraden have studied this chiral-Nematic phase for fdwt and fdY21M [22].

The origin of this chirality is studied and discussed by Grelet and Fraden [95], showing that the chirality was independent of the charge, proposing a model of the existence of a superhelical twist, where chirality occurs at a much larger length scale.

The first observation of the *Nematic-SmecticA* phase transition and *Smectic phase* was per-

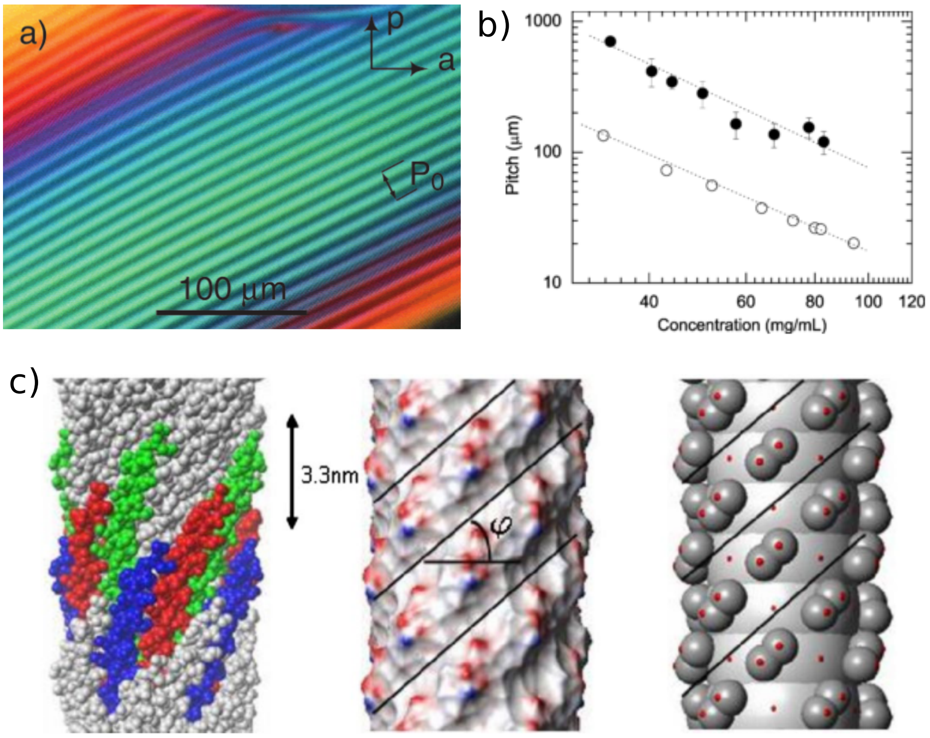

Figure 2.9: *a) Polarized microscopy picture of the fingerprint characteristic of chiral-Nematic phase [92] b) Representation of cholesteric pitch P_0 as a function of concentration for fd (open circles) and fdY21M (solid symbols) [22] c) Model of the helical location of the coat protein on the virus surface. The left image represents the atoms of the individual proteins in different colors. In the middle, the electrostatic representation is shown, where the blue corresponds to the negative and the red the positive potentials. The right figure represents the model for the general surface of the virus; being the red dots the negative punctual charges [94]*

formed by Lapointe and Marvin [93], observing a periodicity of $1\mu m$ and the iridescence due to the diffraction of white light. Later, extensive studies were carried out to explain the behavior of the Smectic phase depending on the flexibility and charge of the fd virus [21, 89]. Also, the flexibility will shift the Nematic-Smectic phase transition to higher volume fractions and decrease the smectic periodicity. Dogic explained that N-Sm phase transition of fd viruses is discontinuous (first order) rather than continuous (second order), and the fd smectic layer spacing is approximately one rod-length, and this value decreases with rod flexibility. This effect of flexibility on the stability of the Smectic phase has been already predicted by simulations [42]. Later, the formation of a Smectic-B phase by fd viruses was shown by Grelet [19]. The difference between Smectic A and Smectic B is the ordering within the layer of the particles being liquid-like for Smectic-A and crystalline like for Smectic-B (Fig.2.10). Also, Grelet

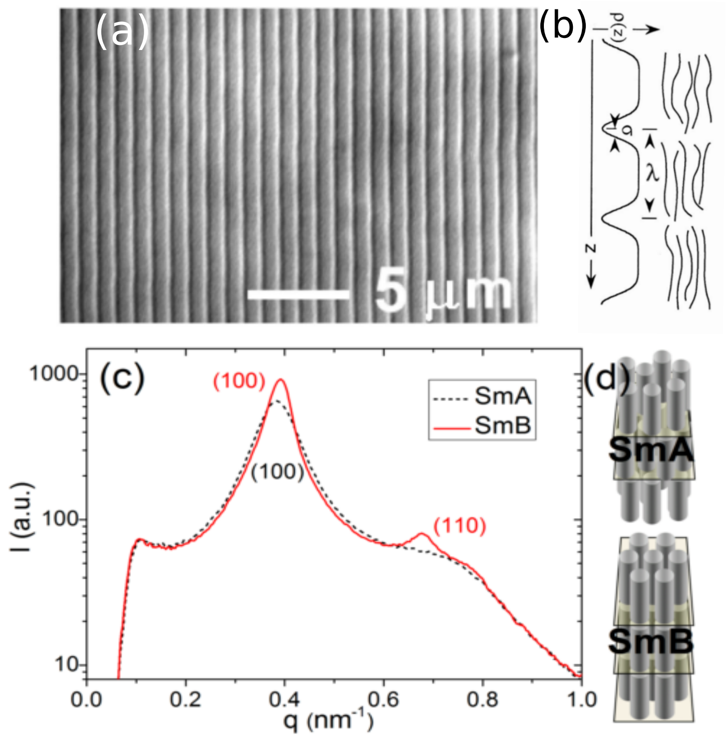

Figure 2.10: *a) DIC optical micrograph of the fd smectic. The high contrast narrow black-white lines are the gaps between smectic layers. The particles are oriented perpendicular to the smectic planes [20]. b) Sketch of the smectic layers where $\rho(z)$ density distribution and λ is the layer spacing [20]c)Scattered intensity obtained by SAXS that shows the different ordering within the layer for SmA (dotted black line) and SmB (solid red line) phases d) corresponding SmA and SmB schemes [19].*

proposes how the condensed ions estimated by different models change the effective diameter, finding a good agreement between experiments and theory. The smectic layers create a periodic energy landscape in one dimension, which as we will see later, affects the dynamics.

2.4.3 Dynamics of the fd virus throughout the phase diagram

The fd viruses can be labeled with fluorescent dyes, which make them a suitable system to be observed under fluorescence microscopy. Moreover, the high aspect ratio (L/D>100) of these particles allows for the study of the self-rotational diffusion of the particle and the diffusion along the short and long axis. This is indeed interesting to investigate the self-dynamics at the single particle level, related to the available space and being a probe for the entropy of

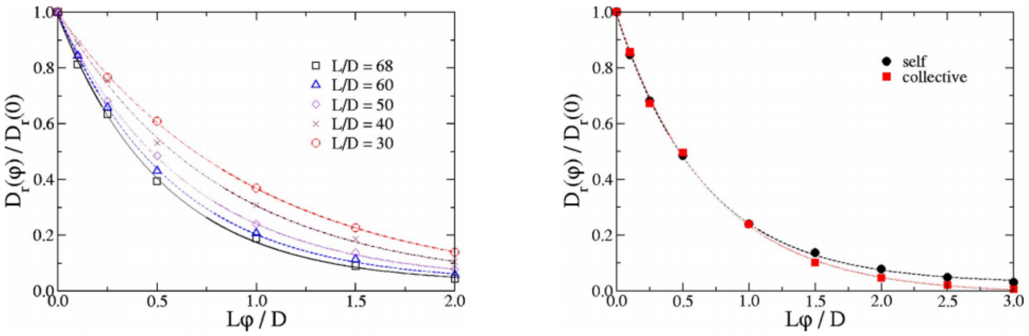

Figure 2.11: *a) Results of simulation for the rotational self-diffusion coefficients of rigid rods with various aspect ratios as functions of the scaled volume fraction based on Doi's theory in semi-dilute regime b) Scaled volume fraction dependence of self (black circles) and collective (red squares) rotational diffusion coefficients for rods of L/D=50 [60].*

the system. Using this technique the position and orientation of each particle at every point in time is known. Hence, the dynamics of the fd virus in the different mesophases has been investigated over the past decade.

It has been demonstrated that the diffusion in the Isotropic and Nematic phases is affected by the change of free volume [26]. In the Isotropic phase, the rotational diffusion decreases by increasing the concentration. Simulations for fd viruses were performed to study the collective and self-rotational diffusion, as shown in Fig.2.11. In these simulations, there is a difference between the collective and the self-rotational diffusion, where the last does not drop to zero. Moreover, in the semi-dilute isotropic regime, the rotational diffusion starts to be restricted due to the interaction which neighbor rods. This agrees with the model proposed by Doi for the "tube effect" [51]. This tube diffusion for fd viruses has been confirmed by Modlinska *et al.* in his experiments at I-N phase transition [24], where a reptation-like diffusion is observed within the isotropic a-tactoids at the phase coexistence.

In the Nematic phase, the $D_{||}$ is higher than in the Isotropic phase, being promoted by the alignment of the rods (see Fig.2.12). However, at higher concentration, it decreases due to the packing of rods.

In the Smectic phase a *hopping-like* diffusion between the smectic layers is reported by Lettinga and Grelet [28]. The self-van Hove function shows distinct peaks at integers of one-rod length, as shown in Fig.2.13. To understand this jumping-like behavior we need to introduce the concept of *Smectic ordering potentials*. The Smectic potential can be measured

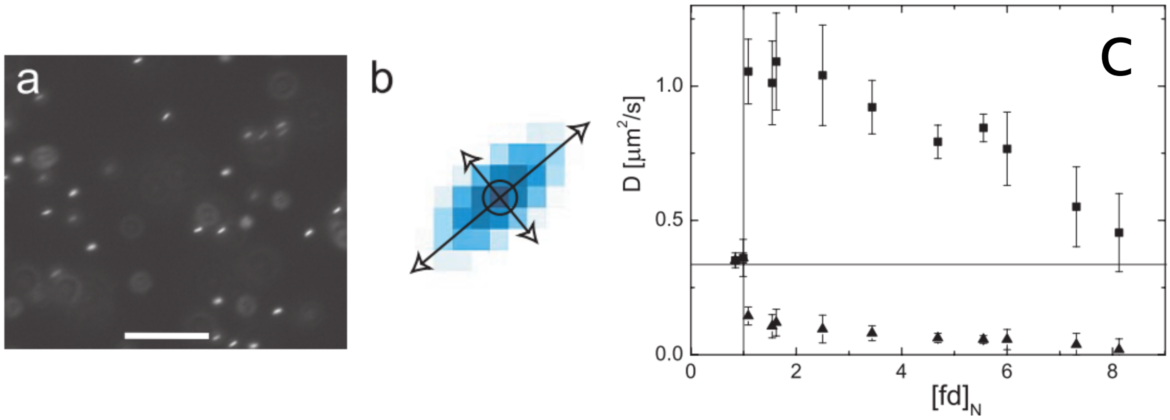

Figure 2.12: *a) Fluorescence image of labeled fd rods dispersed in the Nematic phase of unlabelled ones. The scale bar is 5 μm b) Two-dimensional Gaussian fit for an individual rod. The circle indicates the center of mass and the arrow the short and long axis. c) Diffusion coefficient D_{par} (squared) and D_{per} (triangles) as a function of concentration. The vertical line indicates the I-N phase transition [26].*

from the fluctuations of the particles within the layers. When increasing the concentration, the system gets highly packed, decreasing the fluctuations and increasing the potential barrier. Thus, the diffusion of the particles between the smectic layers decrease. The presence of vacancies between adjacent layers and the packing of the system play a significant role in this type of diffusion. The small perpendicular diffusion within the layer depends on the flexibility, being more restricted for the flexible particles [29]. However, the reasons are still unclear. It has been proposed that flexibility allows a higher packing within the layer, consequently decreasing the perpendicular dynamics [29].

Recently, simulations on dynamics in the Smectic phase with particles of different aspect ratio (L/D) are presented in the work of Patti *et al.* [6]. They show that the potential barrier increases with increasing particle anisotropy, making the dynamics more heterogeneous and non-Gaussian for longer hard rods, having a lower diffusion coefficient. At even higher concentrations, it has been reported that there are full and half-jump displacements in the columnar phase in an aqueous solution of fd, due to the creation of a void. The jumping frequency if higher for flexible particles, in this case [96].

These studies of dynamics are all performed in systems formed by one type of particles. Although there are some studies on the effect of bidispersity in the formation of the Smectic phase, neither the experiments nor the simulations treat the complexity of a Smectic system

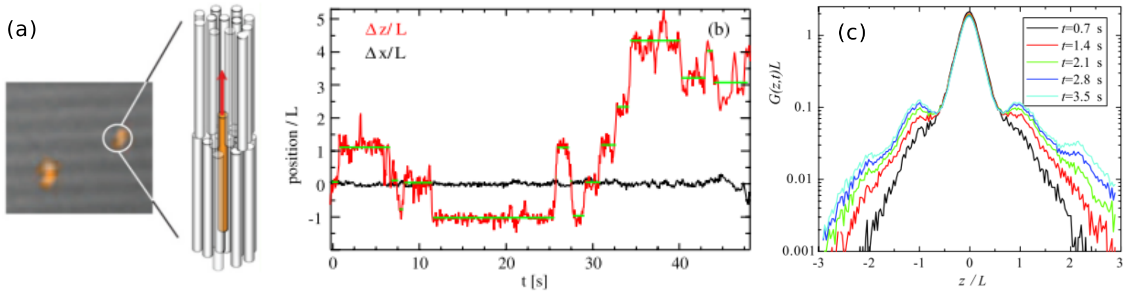

Figure 2.13: *a) Overlay of DIC and fluorescence images, showing the Smectic layers and two fluorescently labeled particles, and the schematic representation of the jump of rod-like particles between adjacent smectic layers. The layer spacing is* $L \simeq 0.92\ \mu m$ *b) Displacement as a function of time of a given particle in the parallel (red line) and perpendicular (black line) directions to the normal of the smectic layers. The horizontal green lines indicate the residence time* τ_{res} *within a layer [64] c) Evolution of the self-Van Hove function at different times. The functions are normalized to one; the z-axis is scaled by the smectic layer thickness L [64].*

with guest particles that do not belong to the host Smectic phase. The interest of studying these systems relies on the dynamics of particles on crowded order phases. In the smectic phase, the dynamics are affected by the Smectic potentials, but a particle that is not commensurate within this potential could exhibit a different behavior. In nature we find a lot of examples for the lamellar-like structure (e.g., cell membranes) [97] as well as for some new materials [98, 99]. The effect on dynamics of the organization of the host system as well as the characteristics of the guest particle could be addressed. Moreover, the behavior of the dynamics at the phase transitions and its dependence on physical propertier of the particles remains unclear and a challenging part of the dynamical studies.

2.5 Outline of this thesis

The study of the self-organization of colloidal liquid crystals treats the simplest phenomena of forming structured systems. In a system where anisotropic particles have hard core interactions, the self-organization is purely entropy driven due to the maximization of the free volume of the system. Thus, the measure of dynamics at the single particle level should provide information on the available free volume and the structure of the mesophase. The dynamics can be used to address different questions related to the liquid crystalline phase transitions and with the structure of the mesophases. We propose different approaches to find a dynamical signature of the phase transitions, to dynamically recognize the order of the phase transitions, to explore the dynamics as a function of physical features such as flexibility and length, and finally to study the diffusion of guest particles in a layered system.

Experimentally, the self-dynamics has been used extensively in the study of the kinetics and diffusion of liquid crystalline mesophases of fd viruses [27–29, 63], which are considered a colloidal model system of rod-like particles. However, some questions have not been treated concerning the dynamics at phase transitions and the techniques to characterize it. Furthermore, systems of higher complexity, like the guest-host systems of Smectic phases can help to understand diffusion in high order systems, as found in nature. Although there are extensive theoretical and simulation studies focused on how the stability and location of the phase transitions are affected by flexibility, aspect ratio and monodispersity, very few experimental studies have been done about dynamics and kinetics at the phase transitions of fd viruses [24, 63]. On the contrary, there are no studies of the diffusion of inclusions in the Smectic phase of fd viruses, which could help to understand the behavior of diffusion through lamellar structures found in nature.

In this Thesis, we aim to clarify the nature of the dynamics at the phase transitions and to understand more complex problems as the introduction of a guest particle in a host system and the effect of length and flexibility in the Isotropic semi-dilute regime where Doi's theory can be applied [51]. We use the analysis of the self-van Hove function as a robust method to characterize the Gaussian behavior, and as an alternative to the *non-Gaussian parameter*. We develop our experiments and data analysis with a complexity hierarchy: going from the less complex to the more complex system and phases. Hence, this thesis is done in such a way that the results of each chapter build upon the previous one.

In Chapter 3 we describe the general experimental approaches and strategies performed during this Thesis, which are the production and purification of our viral particles, the sample preparation for each different system here studied, and finally a brief description of the microscope techniques used.

In Chapter 4 we provide insights of the self-dynamics at each liquid crystalline mesophase of the stiff fdY21M mutant. We characterized the dynamics in the Isotropic-Nematic Phase transition, being highly heterogeneous and glass-like at the Isotropic phase, and undergoing to Gaussian in one direction in the Nematic phase. This is done by analyzing the self-van Hove function. Moreover, we can distinguish dynamical coexistence at the Nematic-SmecticA and SmA-SmB phase transitions by using an image and dynamical analysis. This presents an extra confirmation that N-SmA is a first order phase transition. The question of how the homogeneity of the sample affects the results is discussed.

In Chapter 5 we address the question of how the diffusion of a guest particle is affected by the organization of the host system, concretely when the guest particle is not commensurate within the Smectic phase. We study the self-diffusion of a semi-flexible long guest particle that has been included in the host Smectic phase of the stiff fdY21M. We show that the long and semi-flexible particle exhibits a faster and more continuous diffusion through the layers, in comparison with the jumping-like diffusion of host fdY21M. Furthermore, the results of the dynamics within the layer suggest that its perpendicular diffusion is restricted, being only promoted by the parallel diffusion when permeating between the layers.

In Chapter 6 we present the study of dynamics of the guest particles presented in the previous chapter, which is located into defects of the Smectic phase. We show that particles diffuse within a defect exhibit a slightly super-diffusive behavior. The analysis of the trajectory and the diffusion exponents make us conclude that the change of geometry imposed by the defect promotes the D_{par} of the guest particle. Moreover, we observe that the long guest particle prefer to be located within defects, where it exhibits Nematic-like diffusion.

In Chapter 7 we study the effect of flexibility in the diffusion at concentrations corresponding to the semi-dilute regime in the Isotropic liquid phase. With these preliminary results, we show that the flexibility may help to release the constraints imposed by the surrounding neighbors, making the diffusion at this concentration more Gaussian-like.

Finally, we conclude by providing an outlook and perspectives for future investigations.

3

Experimental Materials and Methods

In this chapter, we will introduce the experimental procedures followed in this thesis from the very first step of sample production and preparation to the data acquisition by techniques such as fluorescence and DIC microscopy. In the first section, we introduce the standard protocol for virus production and purification. In section 2 we explain a method of induced fractionation used to remove polyphages from the sample. In section 3 we get into details of the protocol followed for the particle labeling with fluorescence dyes. Finally, in the last section we describe the sample preparation to perform microscopy observation.

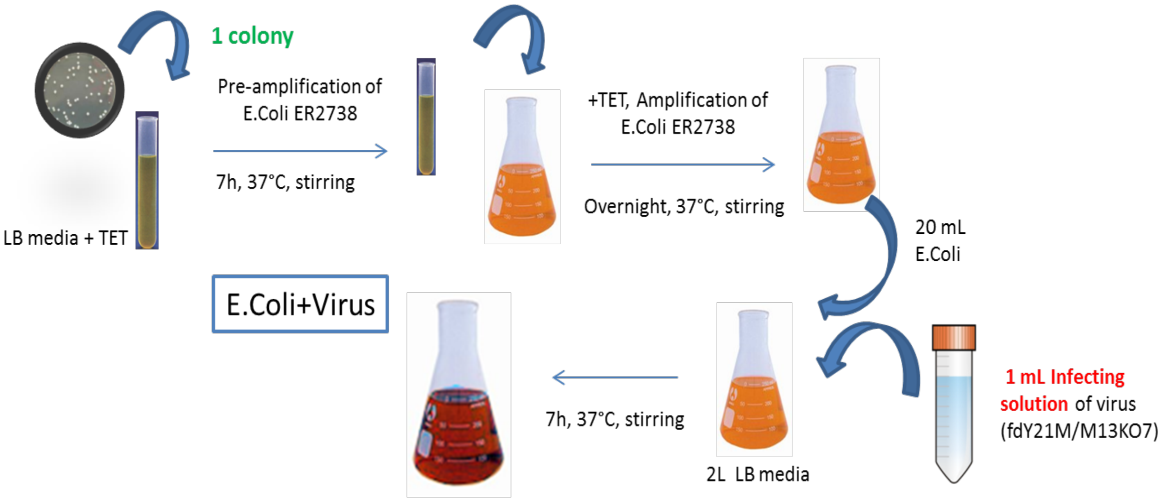

Figure 3.1: *Scheme of the different steps carried out during the phage infection process*

3.1 Production and purification of fd bacteriophages

Filamentous bacteriophages (fd, M13, and f1) are well known for their ability of the infection of *Escherichia Coli* bacteria, by the complex formation between the minor coat protein g3P (see Chapter 1) and the bacteria integral membrane protein TolA, which leads to the introduction of the phage genome into the bacterial cytoplasm [100, 101]. The infection technique is used to prepare stock samples of viruses which are further purified. The production and purification of fdY21M and M13KO7 were performed several times to get a stock sample for future experiments.

Production of fdY21M and M13KO7 bacteriophages. In both cases, the viruses were grown following the standard biological protocol using E.coli ER2837 as host bacteria. All materials and LB media have been autoclaved before the production, and the infecting experiment was carried out in a biological laminar-flow hood. All the infection procedure has been done in extremely clean conditions, by cleaning with ethanol the instruments used (pipets, vials) before introducing them in the laminar flow hood to avoid the introduction of any biological contamination.

We first pre-amplified the bacteria, taking a colony from the Petri plate in 3mL of LB media where we add 4 μL of Tetracycline (TET, antibiotic, $1.5x10^{-2}\ mM$). The incubation is done for 5 hours at 37 $^{\circ}C$ and 200 rpm, until the solution is turbid. Then, in a 500 mL Erlenmeyer we add 100 mL of LB media, 1 mL of the bacteria solution and 133 μL of TET, and we let it grow overnight stirring at 200 rpm at 37 $^{\circ}C$. For the infection of bacteria dispersion with the bacteriophage, 6 total liters of LB media are divided in three Erlenmeyer (2L in each one) and autoclaved. Then, we add in each Erlenmeyer 20 mL of the pre-amplified bacteria and 1 mL of the bacteriophages infecting solution of around $10^{-9} PFU/mL$ infection power. In virology, a plaque-forming unit (PFU) is a measure of the number of particles capable of forming plaques per unit volume, like in this case viruses [102].

The final infected solution is stirred for 7h at 37 $^{\circ}C$ and 200 rpm. It is important to control the bacteria Optical Density (OD). When the OD is between to 0.5-0.9 (approx.6 hours), the growth has reached an exponential state. Before the OD reaches 1, we stop the infection and we proceed to the purification step.

Purification of the viruses from the bacteria solution. After the step of infection, the viruses need to be purified from the bacteria. It is important to remark that the first turbidity that we observe during and after the infection is due to the growth of bacteria. Viruses are 1 μm length and 6 nm diameter, while E.Coli are approximate 2 μm length and 1 μm diameter. This difference in size and volume and also molecular weight makes possible the separation of the bacteria and the viruses with centrifugation. For the bacteria removal, we use a rotor F10-4x1000 LEX in a Sorvall RC6+ centrifuge. We set the speed at 6000g (approx. 6000 rpm) during 20 minutes at 4 $^{\circ}C$, to separate the bacteria of the virus suspension. We put the supernatant (with the suspended viruses) in clean and sterile Erlenmeyer. In each Erlenmeyer where the supernatant has been collected we add 15g per liter of NaCl and 20g per liter of PEG 8K, working as a depletant for the negatively charged viruses. The depletion is performed to collect the viruses at low-speed centrifugation from significant volumes of LB used during the infection process. Depletion takes place under stirring during around 1h at 4° C, until the solution is turbid. In the next step, the viruses are collected by centrifugation using the same rotor and centrifuge, at 6000g (approx. 6000 rpm) during 30 minutes at 4 $^{\circ}C$. The pellet is re-dispersed in a small amount of distilled water and transferred to 20 mL ultra-centrifuge tubes. Another step of bacteria removal is done at higher speed using rotor F50L-8x39 in the Sorval WX Ultra 80 centrifuge, at $24000g(15000rpm)$ for 45 minutes at 4 $^{\circ}C$. The supernatant containing the viruses is collected, and it needs to be concentrated by ultra-centrifugation at 215 000g (45000 rpm) for 3 hours at 4 $^{\circ}C$. After this step of centrifugation, the viruses have precipitated forming a pellet, and the supernatant is discarded. We redisperse the pellet in approximately 20 mL of fresh TrisHCl-NaCl buffer at 20 mM and $pH = 8.2$ to stabilized the electrostatic interactions and it is stored in the fridge at 4 $°C$ as a stock solution for our experiments. The concentration of the viruses can be checked by getting the absorbance at 269 nm (extinction coefficient of the virus is 3.84 cm^2/mg for fd-wt and M13 or 3.63 cm^2/mg for fd-Y21M) with a spectrophotometer Genesys 10 UV scanning (Thermo). As purity check the ratio between the absorbance at 269 nm and 244 nm should be less than 1.41 for impurities below 1% [103]. The final yield obtained from the production (using 6L of LB media) is approximate 130 mg for fdY21M and 180 for M13KO7. The concentration of stock solution is between 40 and 50 mg/mL.

Characterization by Transmission Electron microscopy. The length of fdY21M and M13KO7 viruses after the production was measured using TEM (Transmission Electron Microscopy), analyzing the images obtained as shown in Fig.3.2. The center of the peak is placed at the average length value for each virus. For fdY21M there is a percentage of dimers in the sample (at around 1800 nm), while there is no important of dimers in M13KO7 sample.

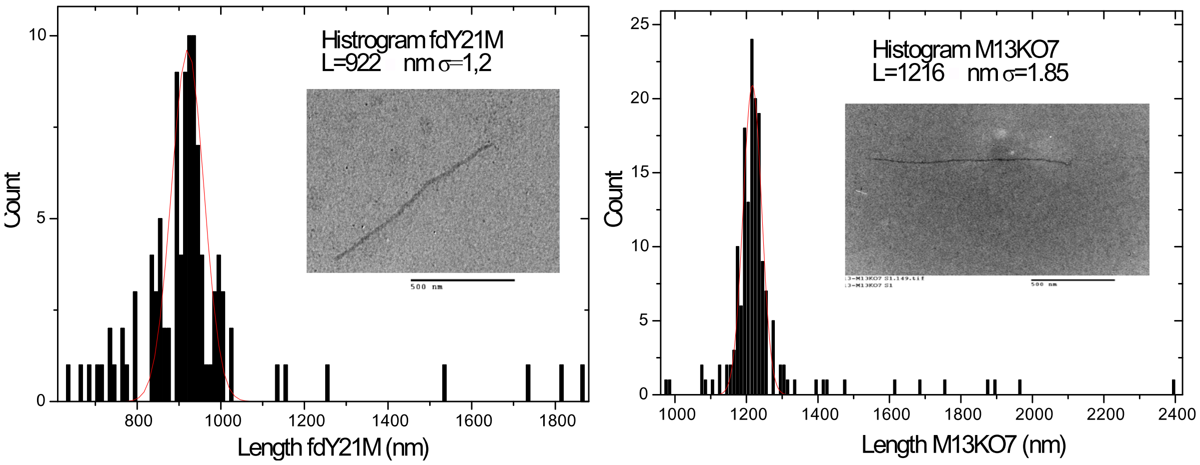

Figure 3.2: *Histogram of the length of the viruses obtained from the measured of the TEM images for fdY21M (left) and M13KO7 (right). Red line is the Gaussian fit. Insets are the original TEM images.*

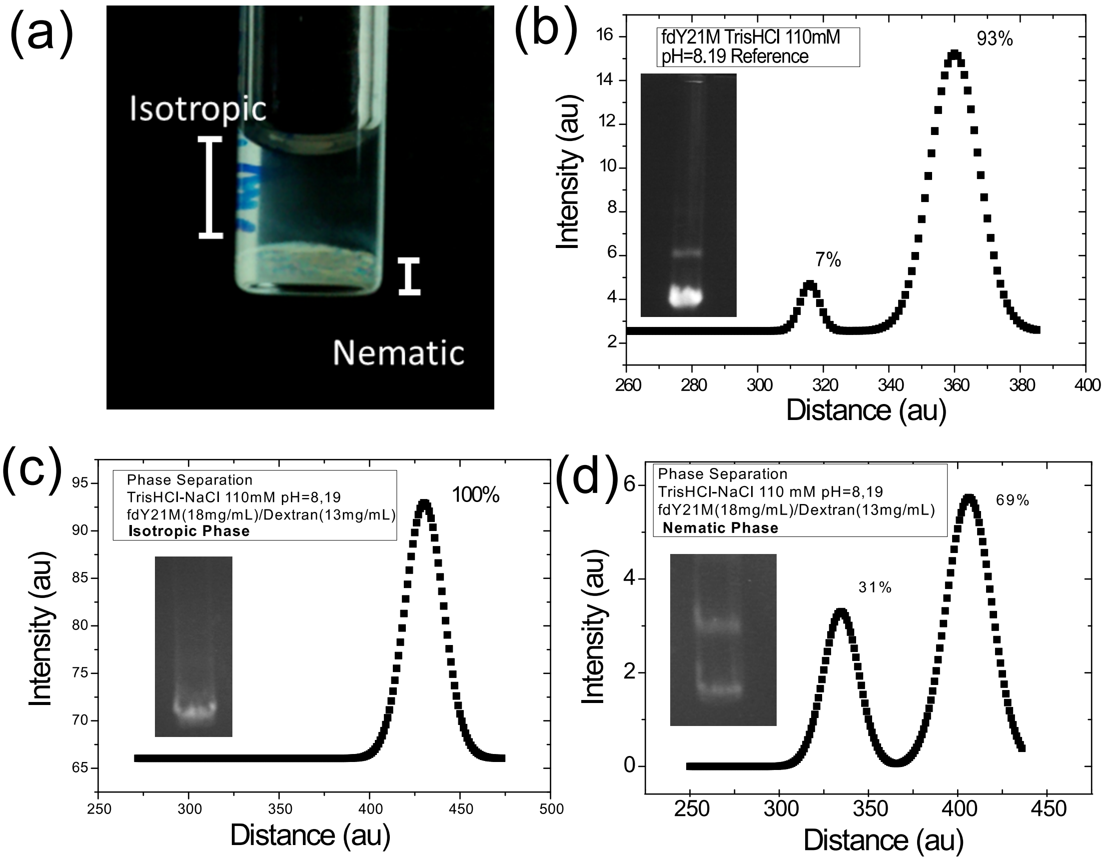

Figure 3.3: *a) Image of the phase separation using Dextran between polarizers. Analysis of the intensity from the gel electrophoresis (inset) of the b) reference sample c) Isotropic phase after phase separation d) Nematic phase after phase separation .*

3.2 Induced phase separation using non-adsorbing polymer to increase monodispersity

Since we aim to have completely monodisperse tracers in our experiments, we have performed a sample purification for fdY21M using Dextran (non adsorbing polymer) as depletant, which will allow us to phase separated the longer polyphages from, the shorter (Brandeis protocol, private communication).

The presence of Dextran increases the concentration at which the I-N transition takes place and also extends the phase coexistence concentration [63, 104]. The long viruses (dimers, trimers) go to the Nematic phase due to the difference of free volume, while the small viruses stay in the Isotropic phase (see Fig.3.3). The buffer used for the experiment is TriHCl-NaCl 110 mM pH=8.19. Different concentrations of Dextran have been tried in a small volume of our fdY21M. The optimal concentration of Dextran and fdY21M for the phase separation are 13 mg/mL and 18 mg/mL respectively, for which the separation was efficient as shown in Fig.3.3.

Gel electrophoresis for virus characterization. The characterization of both phases obtained from the induced phase separation with Dextran has been done by gel electrophoresis. Shorter molecules move faster and migrate farther than longer ones because shorter molecules migrate more easily through the pores of the gel. This characterization confirms that there are not polyphages in the Isotropic phase after the phase fractionation. Contrary, in the Nematic phase we have a population of monomers and polymers of the fdY21M viruses.

The gel used is 1.4% agarose to have the optimal pore size, weighing 0.7 g of agarose in an Erlenmeyer and add 1x TBE Buffer until the total mass reaches 50 g. The mix is heated in the microwave until the agarose melts. The solution is transferred to the agarose tray to cool it down. We prepare 20 μL of the sample of around 1 mg/mL and for the staining, we add 4μL of Bromophenol Blue (used as tracking dye in electrophoresis). The electrophoresis was performed overnight at 28V to obtain an optimum resolution of the sample. The next day the gel is introduced into a solution of NaOH of 0.2M for 45 minutes in a shaking plate and then put in a distilled water bath for other 45 minutes. After the gel is put into an Ethidium Bromide (BET) bath; a fluorescence dye used to stain nucleic acids, as the gel is checked with UV-light. We need to take extreme precaution due to the high toxicity of this compound

The purified total mass of monomers obtained from the Isotropic phase (around 6 mg) is used for the functionalization with fluorescence dyes, as explained in next section.

3.3 Efficient fluorescence labeling for microscopy observation

The measure of dynamics of Brownian particles have been mostly done by fluorescence imaging using different techniques such as Fluorescence Correlation Spectroscopy, Fluorescence

Recovery after Photobleaching (FRAP) and dynamic light scattering [105–107]. However, the simplest way to obtain the diffusion coefficient is by individually imaging the particles using fluorescence microscopy [108–110]. This technique, as it is performed in this thesis, allow us to observe individual *tracer* particles when they are dispersed in a host system consisting of identical or different, non-labelled particles [28], to further calculate the self-dynamics. We have used two different viruses (fdY21M and M13KO7) for two main experiments: 1) dynamics in pure systems (labeled viruses in a matrix of identical non-labelled viruses), 2) dynamics in guest-host systems (labeled viruses inside a matrix of different non-labelled viruses). We assume that the labeled particles behave similar to the unlabeled ones, as demonstrated to happen regarding physical features, such as length and diameter [111]. The two different dyes are used as shown in Table 3.1, one for each virus.

Table 3.1: *Resume of dyes used and the correspondent virus labeled.* $\lambda(nm)$

Dye name	Molar Weigth (g/mol)	Virus	Excitation/Emission (λ)
Alexa Fluor 488 5-TFP	884.91	fdY21M	495/519
Dylight 549 NHS Ester	982	M13KO7	556/571

NHS and TFP Esters react with primary amines of the protein, forming stable, covalent amide bond and releasing the NHS groups, as shown in Fig.3.4.

The most important point during and after the labeling process is to protect them from light with aluminum foil to avoid photo-bleaching of the dyes. Moreover, the second consideration for the labeling of the virus with fluorescent dyes is that the reaction between the dye and the virus occurs with the amine groups of the coat protein. Thus, TRIS buffer has to be excluded, due to the presence of amine group that will compete with the coat protein amine groups of the viruses. For the labeling with Alexa Fluor488 5-TFP ester, the buffer used is Sodium Carbonate ($I = 150mM$ and $pH = 9$), while for Dylight549-NHS Ester we have used Phosphate buffer ($I = 350\ mM$ and $pH = 7$). In the case of reaction with the TFP ester, a slightly basic pH is needed, to maintain the amine group in the non-protonated form. For the NHS ester, we achieve a more specific labeling due to the neutral pH, as the pk_a of the amine is lower than the amine terminus protein of the virus ($pK_a = 7.9$). The virus concentration should be around 1 mg/mL. The dye has to be kept in the fridge inside the glove box.

Dialysis of the viruses for the labeling with fluorescent dyes. The fresh buffer is prepared one day before the labeling is done (see Appendix 1) to perform the dialysis to exchange

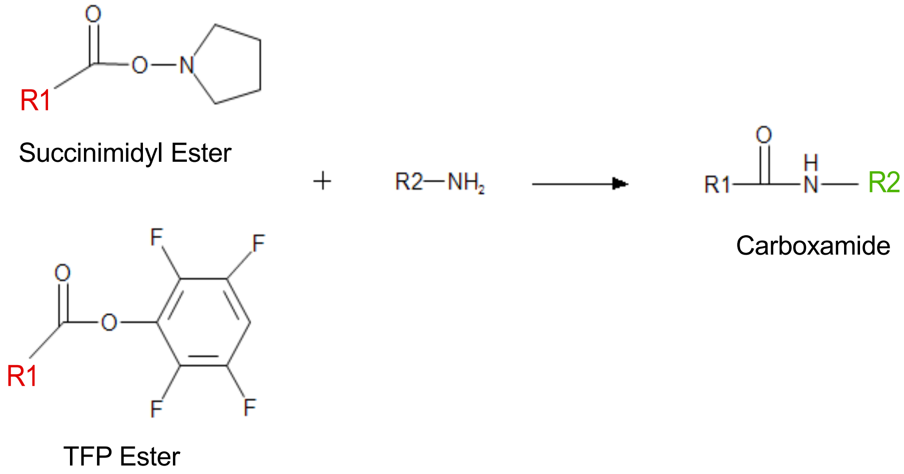

Figure 3.4: *Scheme of reaction corresponding to the functionalization of viruses with the two types of fluorescent dyes. The reaction takes place between the surface amino group and the ester groups of the dyes.*

buffer. The principle relies on the selective diffusion of molecules across a semi-permeable membrane with a fixed pore size. In our case, we use SnakeSin 10K Molecular weight cut-off (MWCO), which allows the exchange of ion concentration of the buffer and non-reacting dye molecules, while the viruses stay inside the membrane.

We first need to clean the stock solution from any bacteria. We take 1mL of the stock solution of around $40-50\ mg/mL$ and we transfer it to a clean ultracentrifuge tube in which a volume of the fresh PBS buffer at 350 mM ionic strength and $pH = 7.0$ is added to have a final concentration of around $4-5\ mg/mL$ and a bacterial removal step is done. We transfer the supernatant to a clean falcon tube of 15 mL. The dialysis bag is prepared in which 1 mL of the already clean solution is transferred and after PSB fresh buffer is added giving final concentration between 1 and 2 mg/mL. The dialysis is carried out against the fresh buffer, which should be 3 times the volume inside of the dialysis bag. We make at least 3 changes of buffer and leaving the last change overnight. The next day the sample is removed from the dialysis bag (essential to rinse the bag walls well to recover all viruses that could get attached to the dialysis bag).

Labeling of fdY21M and M13KKO7. To start with the labeling process, we take a volume of around 1 mL of our stock solution at around 1 mg/mL and we transferred it to a glass vial covered with aluminum foil and with a small stirring bar inside. The dye stock once opened, has to be used in one go. The quantity (mass) of virus which has to be adjusted knowing that, for 1mg of virus the optimum number of moles of the dye is $0.5x10^{-6}mol$ [112], having a 3 times excess of dye per protein. The dye should be dissolved in DMSO in a volume such that it does not exceed 20% of the total volume when added to the virus suspension. The viruses have to be added carefully. Once the dyes and the viruses are mixed, the reaction is carried out under stirring during 1h at room temperature or overnight at $4^{\circ}\ C$, in the fridge (still under stirring). After the process of labeling, the solution has to be purified from the excess of dye, and the buffer needs to be changed again. Several dialyzes are done until the outer dilution color is transparent, against the desired buffer. In this case, we use TrisHCl-NaCl at 20mM and pH=8.2. After, the solution of labeled dyes is transferred to a ultracentrifuge tube where a first turn to clean bacteria is done and then the sample is concentrated, and the pellet is redispersed in the chosen buffer to have a stock solution concentration of 1mg/mL.

3.4 Optical microscopy techniques: sample preparation and observation

In all the experiments a fixed concentration of tracers is introduced in the non-labeled virus sample (matrix). These samples need to be in the correct buffer for each experiment, so a dialysis has been done as explained before the experiment. After, each sample is transferred to an ultracentrifuge tube in which a bacteria cleaning step is performed, and then the sample is concentrated (in the same conditions mentioned above), and the pellet is redispersed in the chosen buffer up to Nematic Phase close to Smectic. The addition of the tracers is done at this concentration because homogenization of the sample is easier (liquid like state) and also to have an idea how the tracers look in a background at a relatively high concentration. Later, depending on the experimental system studied we follow different procedures to prepare the dilutions, as explained below.

Prepararation of the pure systems: fdY21M-Alexa488 in non-labeled fdY21M and M13KO7-Dylight549 in non-labeled M13KO7 (Isotropic experiments). A volume that contains 30 mg of the stock virus solution obtained from each production is dialyzed against TrisHCl-NaCl 110 mM buffer at pH=8.2 and then reconcentrated at around 70 mg/mL. A dilution of the labeled stock solution ($1mg/mL$) is prepared at 10^{-4} mg/mL. A set of different dilutions are prepared in 100 mL plastic Eppendorf to get different concentrations from the Nematic phase through the Isotropic up to infinite dilution. Each dilution has a final total volume of 20 μL. Thus, we add a constant volume of tracers (in order to have a final ratio of around 1 labelled virus for 10^5 non-labelled viruses), and spacers (beads of around 500 nm diameter), and we change the ratio between of non-labeled host viruses sample and buffer (increasing the buffer and decreasing the host sample) in order to decrease concentration at each dilution. From each dilution, a volume of around 10 μL is pipetted and poured onto a previously cleaned and dried (see Appendix) glass slide ($76x26$ mm) and covered rapidly with a coverslip ($18x18$ mm). The sample is sealed with UV-glue and covered with aluminum foil.

Table 3.2: *The different systems used in this thesis*

System	Viruses	I(mM)/pH
Pure host-host	fdY21M-Alexa488 in fdY21M	110/8.2
Pure host-host	M13KO7-Dylight549 in M13KO7	110/8.2
Guest-host	M13KO7-Dylight549 and fdY21M-Alexa488 in M13KO7	20/8.19

Prepararation of the guest-host systems: guest M13KO7-Dylight549 and fdY21M-Alexa (Phase Transition and Smectic experiments). The buffer used in this experiment is TrisHCl-NaCl at 17 mM and pH=8.19 in which we have added 3 mM of NaN_3 to avoid any bacteria growing, being an inhibitor for gram-negative bacteria [113–115]. The host system is formed by non-labelled fdY21M at around 70 mg/mL in which labeled fdY21M-Alexa488 and M13KO7-Dylight549 are added directly to have a final ratio of around 1 labeled virus for 10^5 non-labelled viruses. The sample is then re-concentrated to a high dense phase (Columnar) of about 140 mg/mL. Dilutions are done by adding small amounts of the buffer in the same tube and homogenizing by vortexing and centrifuging at low speed. The final sample is prepared by pipetting around $8-10$ μL onto a glass slide. When covering it with the coverslip is important to shear to homogenize the sample. We use two stripes of a thin layer of a polymer film (12 μm) as a spacer, placed at the edge between the coverslip and glass slide. The sample is sealed with UV-glue and covered with aluminum foil. All samples are observed one day after sample preparation to ensure they are in equilibrium.

Optical microscopy observations. Samples with labeled viruses are visualized using an inverted microscope (IX-71 Olympus), equipped with a high-numerical aperture (NA) oil objective (100x PlanAPO NA 1.4) and a mercury lamp as excitation light source (X-cite series 120 Q). The camera used is an sCMOS and Neo, using a rolling shutter. The readout time between

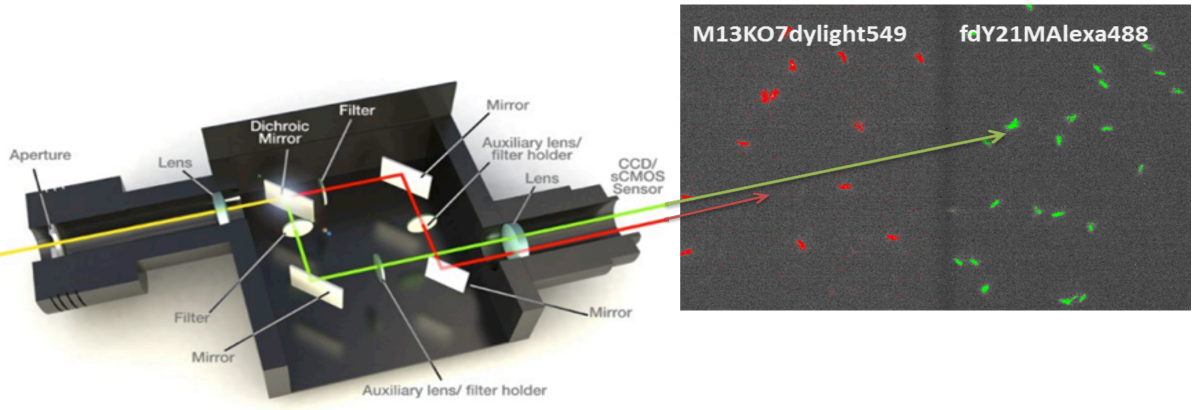

Figure 3.5: *Set-up used for the guest-host experiments. (Left) Scheme of the Optosplit II Andor. The emission wavelength recovered from both dyes is split into two channels by using a dichroic mirror. (Right) Fluorescence image result of the beam split for each labeled particle in the same field of view.*

frames is not the same as the exposure time set during the data acquisition in the microscope. The real read out time is calculate using $readout\ time = (1/frame\ rate) - exp_{time}$.

In the experiments of *host-host pure systems*, the exposure time set for the experiments was 5 and 2 ms, with frame rates of 55 and 199 fps respectively. The corresponding readout times are 2 and 3 ms, which means that the real exposure times are 7 and 5 ms. This difference could be due to the size of the Region of Interest (ROI) used during the data acquisition. The SNR (Signal to Noise Ratio) at 2ms is very low, so we have chosen to use the data acquired at 5 ms. The correspondent polarization microscopy image was taken for each sample. For *guest-host systems* series of experiments, the exposure time set was 20 ms and 5ms, giving frame rates of 33 and 55 fps respectively. The movies taken at 20 ms had a duration of 15 s while the movies taken at 5ms were 5 s total. The readout time for this experiment was 10 ms. Again, for image quality reasons only 20ms data is used and because results are consistent at lowest exposure time (see Appendix). After approximately 6-7 seconds photobleaching of the Alexa488 dyes becomes apparent while Dylight-549 seems to be less photo-bleachable. To observe the two different labeled viruses at the same time in real time, a dual emission image splitter (Optosplit II Andor) was used to project two identical fields of view, corresponding to the two emission wavelengths, on to the two halves of the sensor of the ultra-fast electron-multiplying camera (Fig.3.5). Each time after the acquisition of fluorescence movie a DIC (Differential interference contrast) microscopy picture has been taken to have the correspondent Smectic background.

4

Self-Dynamics as a signature of the Liquid Crystals Phase Transition

In this chapter, we report on the dynamics at phase transitions of a colloidal suspension of stiff viral rods, called fdY21M. The stiff fdY21M forms liquid crystalline mesophases, which undergo phase transitions when varying the volume fraction, due to the maximization of free volume in the system. The dynamics are strongly affected exhibiting a different behavior for each mesophase. We focus on the dynamical insights around the Isotropic-Nematic Phase transition and at the Nematic-SmecticA and SmecticA-SmecticB phase transitions. For this purpose, direct visualization at the scale of a single particle is performed. For the I-N phase transition, we quantify the deviation from the Gaussian behavior analyzing the self-van Hove function, showing that Brownian diffusion is much more restricted in the Isotropic phase close to the Phase transition, and being characterized as glass-like. Moreover, we found a dynamical coexistence at the Nematic-SmecticA and SmecticA-Smectic B phase transitions, confirming that both phase transitions are first order.

4.1 Introduction

Assuming that we have a bunch of pencils inside a box just big enough such that they can be pointing in different directions. If we want to add pencils to the box, we need to optimize the space by aligning them. Thus, the system will undergo a phase transition from a *disordered phase* to an *orientated phase*. In this oriented phase, the rods have more space to be placed, and also more rods can be added. At the colloidal scale, for rod-like particles which undergo Brownian motion, this is the so-called Isotropic-Nematic Phase transition, and it spontaneously occurs at scaled concentration of $\phi = 4D/L$, predicted by Onsager [7]. In the long-rod limit $(L >> D)$, the excluded volume scales as $V_{excl}^{\perp} = 2L^2D$ in the Isotropic phase near the I-N transition. In the case of parallel hard rods and neglecting rod-end $V_{excl}^{\|} = 2\pi LD^2$. At higher concentration, the system undergoes the N-SmA, where the particles gain positional order in one dimension, which leads to the formation of Smectic layers [8, 9, 32]. At even higher concentration, another phase transition occurs from the Smectic-A to the crystalline Smectic-B phase [64], as it is illustrated in Fig.4.1. Thus, colloidal rods self-organize spontaneously into different liquid crystalline phases, displaying different phase transition that are purely entropy driven [4, 45] when increasing the rod density.

It is, however, demonstrated that this loss of entropy between phases is counter-balanced by an increased in the local free volume, and hence, that the dynamics of the single particles are affected [116]. The study and understanding of dynamics at the single particle level around the phase transition is crucial because it might hint to an entropic gain which is related to the accessible free volume. Recent advances in experimental techniques have made it possible to explore the Brownian motion of individual particles in liquid crystalline phases. It is the case for the self-diffusion of actin filaments in dilute and semi-dilute isotropic regimes [62], as well as for the fd viruses [59]. Later, self-diffusion of fd viruses in the nematic phase was studied using fluorescent microscopy techniques [63]. It was found that the self-diffusivity along the main axis of the particles is promoted in the nematic phase compared to that in the isotropic phase. Moreover, in the smectic phase, diffusion of particles along the main axis has been found to be a kind of hopping-type diffusion between smectic layers [27–30, 72, 96]. This is also the case for the Smectic phases of monodisperse silica rods [117].

These studies provided relevant information on the physical behavior for each liquid crystalline mesophase. Contrary, self-diffusion at the phase transitions is still poorly understood, although some experiments have been done [24,44]. In the case of the I-N, simulations showed that the collective rotational diffusion slows down reaching zero, facilitating the formation of aligned states, while the self-diffusion does not [25, 60].

The already mentioned fd virus, are particularly interesting because, unlike most other types of colloidal particle, they are very monodisperse. Due to the high aspect ratio and rigidity, the I-N transition of stiff fdY21M virus takes place at the same volume fraction of the value predicted by Onsager. Their length makes them accessible to be observed under optical microscopy. In this chapter, we study dynamics throughout the full phase diagram by tracking labeled fdY21M inside a matrix of unlabeled particles using fast fluorescence microscopy. We show how we calculate and use different dynamical parameters than can act as dynamical signatures for phase transitions. The main goal is to investigate how the self-diffusion of the particles is affected by the proximity of the phase transition and if, reciprocally, the phase transition is affected by the dynamics of the system. Moreover, we will explore a method to quantify the dynamical signature of the phase transition, as well as characterized dynamically the phase coexistence.

We will treat dynamically three phase transitions of fdY21M: I-N, N-SmA, and SmA-SmB. In the first case, at the I-N phase transition, the analysis of the self-van Hove function (as it has been explained in Chapter 3) is used to quantify the diffusivity on both sides of the phase transition. At higher concentration, N-SmA and SmA-SmB phase transitions, the fitting and analysis of the self-van Hove is not straightforward. Thus, we use a step-detect algorithm (see Appendix at the end of the Thesis) to study the evolution of dynamics at the phase transitions of denser phases, showing that self-dynamics is sensitive to the order of the phase transition.

This chapter is structured as follows: in Sec.1 we show the raw data for the full phase diagram consisting of self-van Hove functions and mean-squared displacement. Then, we first treat the dynamics around the I-N Phase transition analyzing the self-van Hove function. In the last sections, the results for the dynamical coexistence at N-SmA and SmA-SmB are shown and discussed.

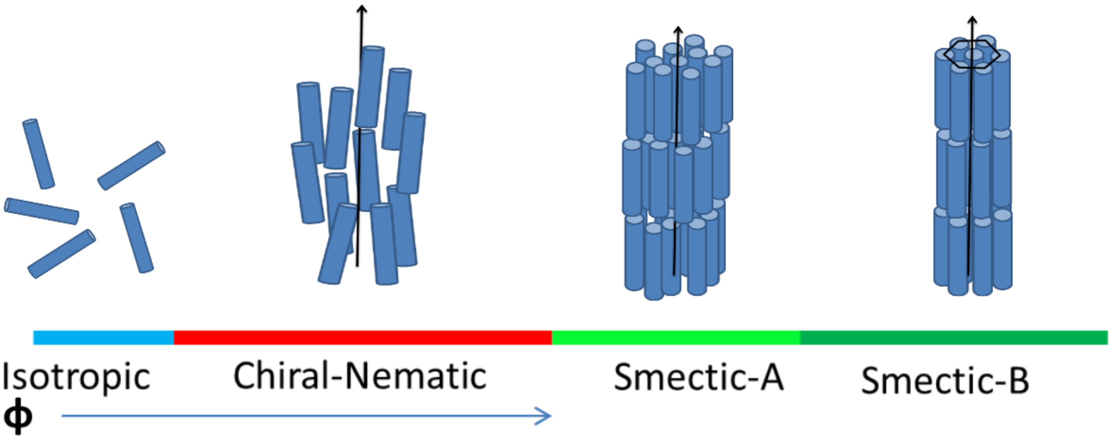

Figure 4.1: *Scheme of the liquid crystalline phase diagram of hard rods. From left to right: Isotropic, Nematic, Smectic A and Smetic B phase by increasing the volume fraction. The black arrow indicates the director* ***n*** *along which the particles are oriented.*

4.2 Stiff fdY21M as a colloidal model rod-like particle: experimental system

We investigate the dynamics of three Phase Transitions of the system formed by the stiff filamentous virus fdY21M: Isotropic-Nematic, Nematic-Smectic A, Smectic A-Smectic B. As already mentioned in Chapter 1, the stiff fdY21M has a persistence length of $P = 9.9\ \mu m$ and a contour length $L = 0.92\ \mu m$, and it has a diameter of $d = 6.6\ nm$. We take a volume from the stock solution sample to have a total mass of viruses of around 40 mg/mL, and we clean and concentrate it with an ultra centrifugation step. We re-disperse from the resulting highest concentrated (Columnar) phase, by adding TrisHCl-NaCl $I = 17mM$ at $pH = 8.2$ and $3mM$ of NaN_3, covering all range of mesophases and phase transitions (Fig.4.1). Samples were prepared by putting a drop of solution between a glass slide and cover slip, as explained in details in Chapter 2. Observations by optical microscopy were performed one day after sample preparation, assuming that the system has reached the equilibrium.

The Nematic and Smectic phases are characterized by their optical features. The chiral-Nematic phase exhibits birefringence by observing the sample through cross polarizers, while the Smectic phase displays iridescence, due to the diffraction of white light from the layer spacing of around 1 μm (see Fig.4.2a and see Fig.4.2b at SmecticA phase). Moreover, polar-

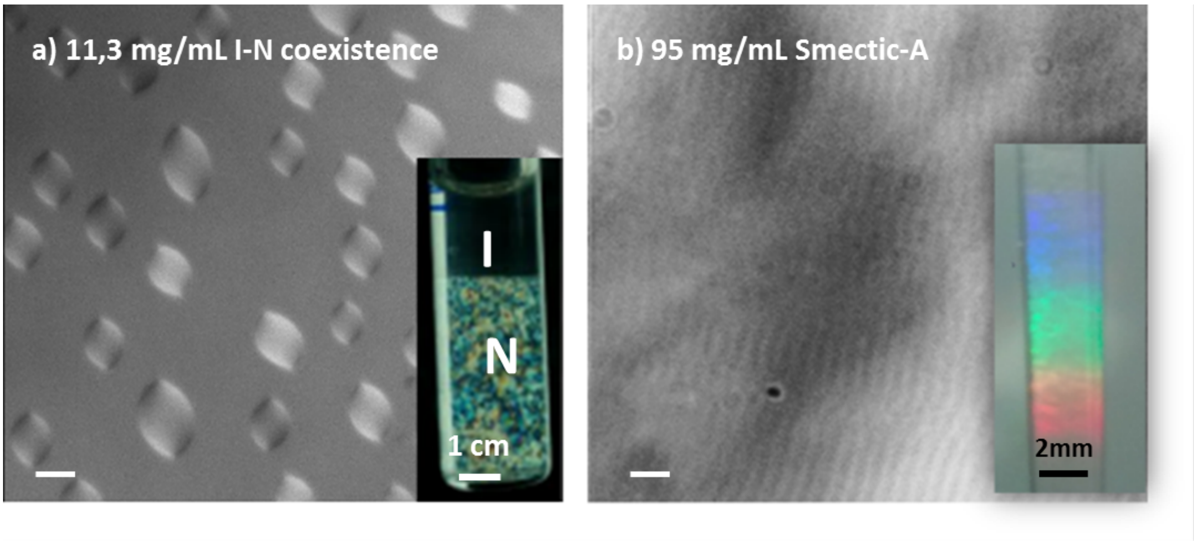

Figure 4.2: *Polarized microscopy pictures of fdY21M samples. a) Nematic tactoids in a background of Isotropic phase. Inset: bulk isotropic-nematic phase transition. b) Smectic Phase, evidenced by a layered pattern. Inset: refraction of white light due to the Smectic pattern. All pictures are taken with a 100x magnification oil immersion objective, Numerical Aperture (NA) 1,4. Microscopy scale bar: 5 μm.*

ize microscopy can be used to determine the liquid crystal phase transitions. However, this is not the case of the SmA-SmB phase transition, as both phases have the same layered pattern. In this case, we need to rely on X-ray experiments [19]. To study the single-particle dynamics forming the system, we added labeled fdY21M virus into non-labelled matrix of the same type of particles to have a ratio of 1 labeled viruses into 10^5 non-labeled. The individually fluorescent labeled viruses were visualized using the techniques already mentioned in Chapter 2, and the further analysis by particle tracking has been done using a Matlab algorithm (Appendix).

We extract the raw dynamic information from trajectories which are produced by the image analysis, as shown in figure 4.3. From left to right we see random diffusion in the Isotropic phase, oriented diffusion in Nematic, jumping-like diffusion in Smectic-A phase and non-moving particle in what we consider to be the Smectic-B phase as will be discussed later. The z-axis is defined by the director of the matrix. All trajectories have been rotated such that the original y coordinates lies on the z-axis. We are able to identify parallel ($||$) and perpendicular ($\perp$) diffusion.

In the next section, we will show calculated features such as the *mean square displacement*

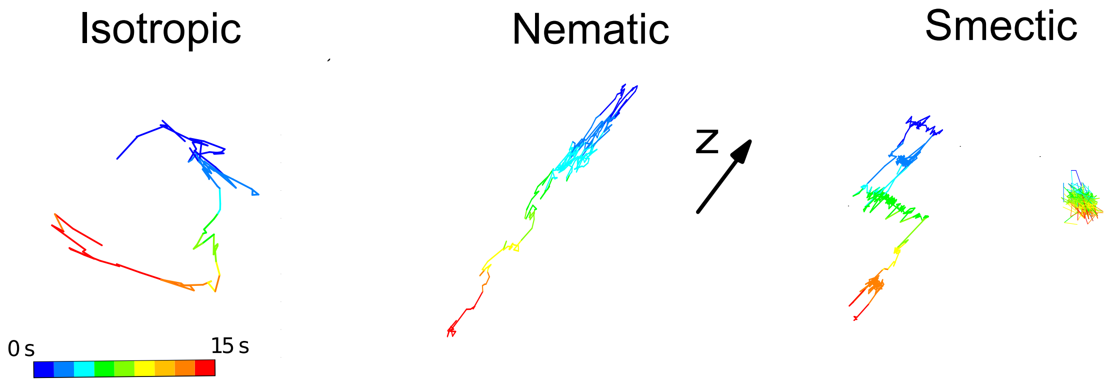

Figure 4.3: *Typical trajectories in the Isotropic, Nematic and Smectic phases obtained from the particle tracking algorithm. For isotropic phase random trajectories are observed, for Nematic phase are oriented in one direction and in the Smectic phase we observe the typical jumps from layers and the residence time of the particle within the layer. The z axis indicates the orientation along the director. The color scale indicates the evolution of the position in time.*

and *self-van Hove function* which are calculated from such trajectories, throughout the full phase diagram.

4.3 Physical and dynamical behavior of fdY21M through the concentration range

4.3.1 Self-Van Hove calculation

We start by calculating the self-van Hove function which gives the probability of displacement z after a time t,

$$G(z,t) = \frac{1}{N}\sum_{i=1}^{N} \delta[z + z_i(0) - z_i(t)] \tag{4.1}$$

For Brownian particles the self-van Hove function takes the form of a Gaussian, with a

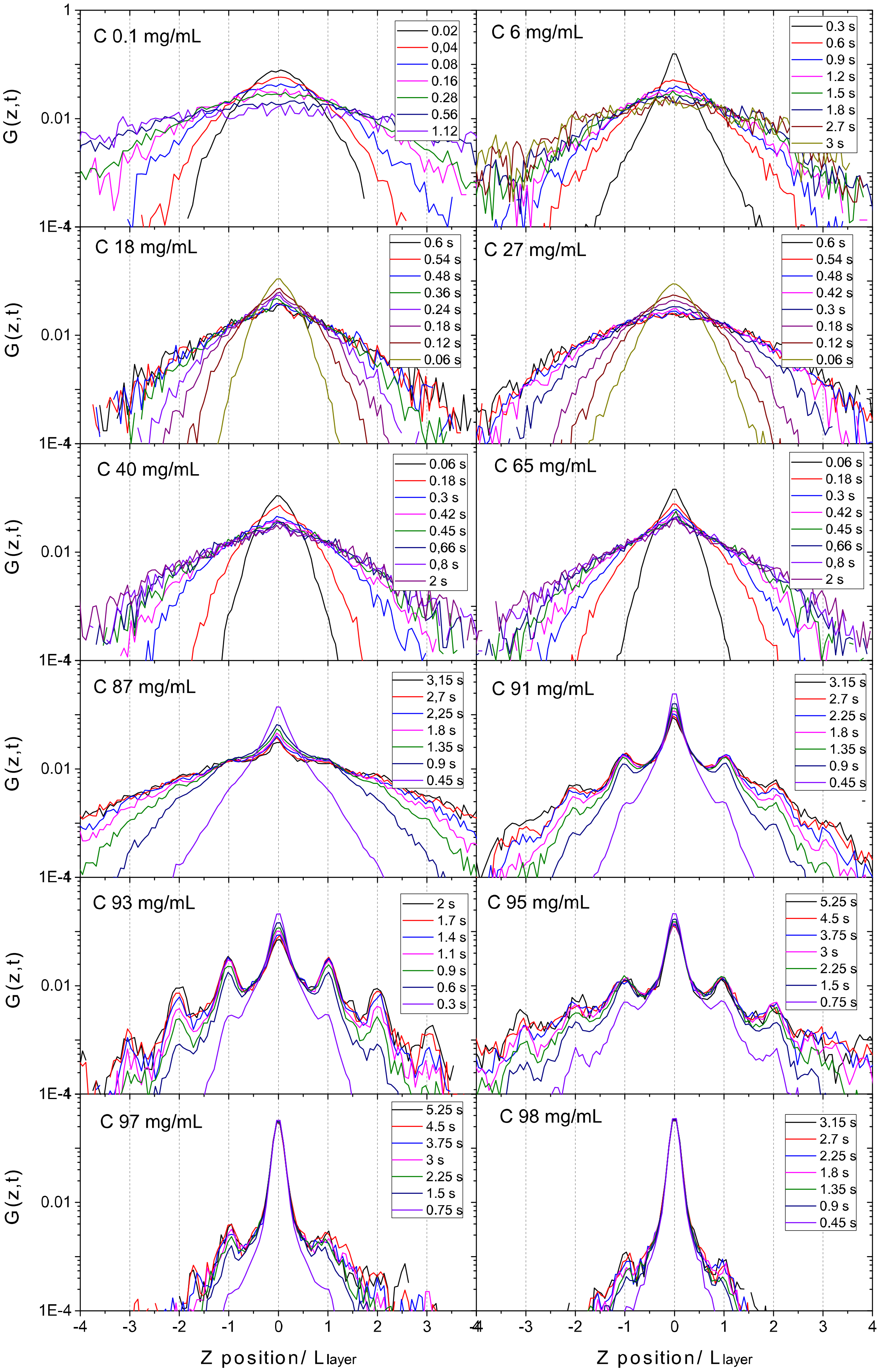

Figure 4.4: *Self-Van Hove probability density function over different time steps for different concentrations through all mesophases of stiff fdY21M. In the Nematic (18, 27, 40 and 65 mg/mL) and Smectic (87, 91, 93, 95, 97 and 98 mg/mL) phases, the parallel self-van Hove is represented. Dashed vertical lines indicate the adjacent layers at one rod length. Position is normalized by the* L_{layer}, $\lambda = 0.92\ \mu m$

probability that smears out with time. In a crowded environment the function will change its shape, and is therefore very sensitive to changes in dynamics and structure of the system. The concentration dependence of the self-van Hove function is shown in Fig.4.4. Indeed, at very low concentration ($0.1mg/mL$) we observed a Gaussian curve, which is frustrated when approaching the I-N undergoes a *roof-tent* shape. In the Nematic phase after the I-N phase transition, for which we only plot the parallel self-van Hove function, the Gaussian shape is recovered. With increasing concentration, approaching the Smectic phase, the Gaussian shape is lost again, and the self-van Hove function starts to exhibit peaks at integral multiples of the particle length [29, 72]. The peaks get sharper when increasing the concentration throughout the Smectic-A. This is a signature of the background potential which is imposed by the Smectic ordering. When reaching the Smectic-B phase, the absence of diffusion is reflected in the self-van Hove function, which does not change over time due to the freezing of dynamics.

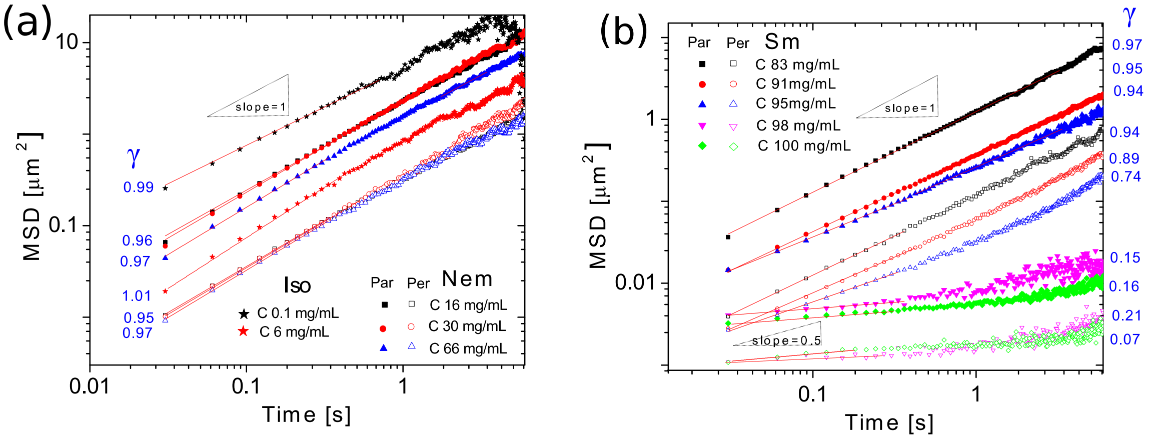

Figure 4.5: *Log-log representation of some of the parallel (solid symbols) and perpendicular (open symbols) MSDs. a) Nematic and Isotropic (star symbols) concentrations b) High dense concentrations (from Smectic to Nematic phase). Each MSD is calculated for around 800 particles.*

4.3.2 Mean Square displacement

The MSD quantifies the average distance that a particle travels in a given time. Most generally, it depends on the diffusion rate D_i and on time as t^{γ}, where the exponent $\gamma > 1$ indicates super-diffusive behavior and $\gamma < 1$ sub-diffusive behavior,

$$\langle r_i^2(t)\rangle = 2dD_i t^{\gamma_i}, \tag{4.2}$$

where d is the dimension of the system and i represent the direction with respect to the director ($||$ and $\perp$ for parallel and perpendicular respectively). In Fig.4.5 we plot the mean-squared displacement (MSD) as a function of time for the full range of concentrations studied: from the dilute Isotropic to the deep Smectic phase. For most concentrations, the MSD exhibits a linear behavior, but in the Isotropic phase close to the I-N phase transition and deep in the Smectic phase, we can distinguish two-time windows at short and long times, well defined by a change of slope. This can be interpreted as an effect of confinement when approaching the crystalline phase, which is overcome with time by the particles which escape from their local cage induced by the crowded environment.

Diffusion coefficients and exponents have been obtained from the fit of the MSDs using Eq. 4.2. For consistency of the results, we have therefore tuned the time range of the fit to always maintain a high fit quality with a minimum value required for the reduced chi-square.

First we will describe the results obtained for the diffusion coefficients D_i. We observe a non-monotonic evolution of the diffusion rates with concentration, as shown in Fig.4.6a. Initially, D_{iso} decreases sharply from the dilute isotropic phase to the semi-dilute regime. Immediately after the I-N phase transition, $D_{||}$ increments dramatically promoted by the alignment of the rods. The increase of concentration in the Nematic phase causes a slow down of $D_{||}$, due to the gain of order packing after the phase transition where the rods strongly align. On the contrary, $D_{\perp}$ drops after the I-N phase transition and stays further constant. These results are in agreement with simulations [118] and also previous experiments [26]. The diffusion is even more restricted entering in the Smectic-A phase, due to the smectic ordering which favors the *jumping like behavior* through layers, as we have shown already in the Self-Van Hove functions.

Furthermore, we plot in Fig.4.6a in blue, the *total diffusion rate* given by $D_{tot} = D_{||} + 2 * D_{\perp}$, indicating that indeed also the total diffusion increases after the I-N transition, while it smoothly decays from the deep Nematic phase throughout the N-Sm phase transition and the Smectic-A phase. Finally, the D_{tot} drops to zero in the Smectic-B phase.

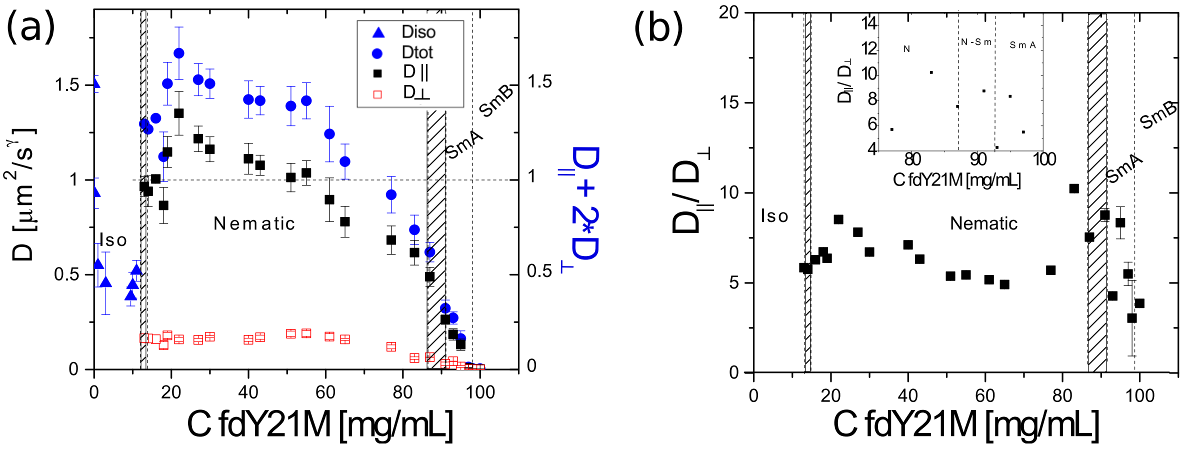

Figure 4.6: *Concentration dependence for a) The* $D_{\|}$ *(black solid squares),* $D_{\perp}$ *(red open squares) and* D_{tot} *(blue symbols) b)* $\frac{D_{\|}}{D_{\perp}}$ *for stiff fdY21M (black squares). Inset zooms in the N-Sm Phase transition. Dashed vertical lines delimit the phase transition regimes. Error bars indicate the St.Deviation*

In addition, in Fig.4.6b we plot the ratio $\frac{D_{\|}}{D_{\perp}}$ as a function of concentration. Starting at the I-N transition, a maximum in $\frac{D_{\|}}{D_{\perp}}$ evolves due to the increasing of the $D_{\|}$, as mentioned above. Surprisingly, we observe also a jump in the $\frac{D_{\|}}{D_{\perp}}$ in the concentration just before the N-Sm Phase transition (85 mg/mL) and in the first concentration at the phase transition (87 mg/mL). This could be a *pre-transitional effect*, and suggests that N-SmA transition is driven by increased *configurational entropy* in the parallel direction rather than free volume gain within the layers. When reaching the Smectic-A mesophase $\frac{D_{\|}}{D_{\perp}}$ tends to decrease as the $D_{\|}$ decreases due to the Smectic ordering.

Regarding the diffusion exponents γ_i, we plot the evolution with concentration as shown in Fig.4.7. At very low concentrations in the Isotropic $\gamma \cong 1$, which is characteristic of diffusive behavior. However, around the I-N Phase transition, we observe a dip of the diffusivity. After the I-N phase transition, it fluctuates around one throughout the Nematic phase. Finally, when entering the Smectic-A phase, the exponents for both directions decrease, gradually reaching values below 0.5. This is typical behavior for glassy dynamics [53, 70] and at even higher concentrations it drops to zero, which is related to the absence of dynamics. This is in agreement with the fact that in the Smectic-B phase particles are crystalline-like within the Smectic layers [19].

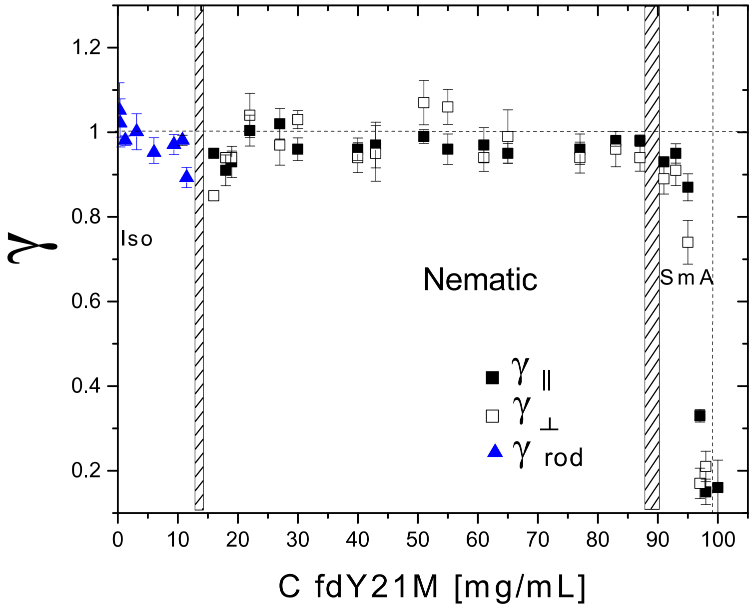

Figure 4.7: *Diffusion exponent $\gamma_{||}$ (black solid squares), $\gamma_{\perp}$ (black open squares) and γ_{iso} (blue triangles). Dashed vertical lines delimit the phase transition regimes. Error bars indicate the Standard Deviation*

The study of the diffusion exponents and coefficients gives a hint of the behavior of the system. However, together with these studies, we need a different approach to characterize the dynamics. In following sections, we will do an analysis and quantification of dynamics beyond the results previously presented. This is done for all phase transitions, starting from the I-N, then N-SmA and finally SmA-SmB.

4.4 Isotropic-Nematic Phase transition

The I-N phase transition of fd virus is a first order phase transition [20,119] where the Isotropic and Nematic phases coexist. The dynamics at the I-N phase transition is distinctly different for each phase [24, 63], as the free volume in the Isotropic phase is much lower than in the Nematic phase. Increasing the concentration in the Isotropic phase, the diffusion is frustrated as explained by Doi [51], reaching the semi-dilute regime where the particles diffuse through a tube created by its neighbors. For densely packed colloidal spheres in the glass state, it is

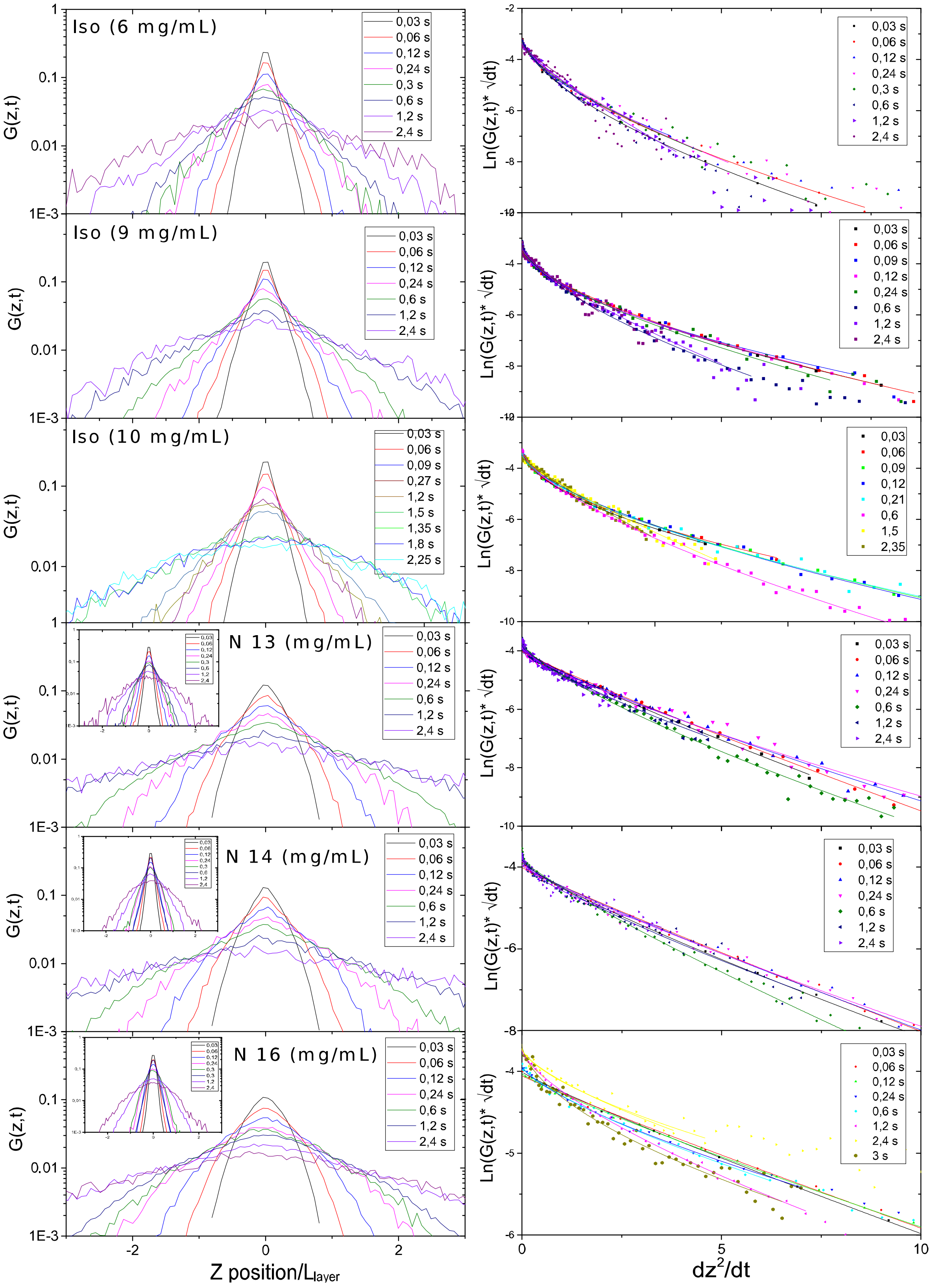

Figure 4.8: *Parallel self-van Hove functions (left) and fitting of the normalization (right) at concentrations around the I-N Phase Transition at Isotropic (6,9 and 10 mg/mL) and Nematic (13,14,16 mg/mL). Fitting has been done with* $y = a_1 x^{a_2}$*; being* $a_2 = 1$ *and* $a_2 = 0.5$ *if it is Gaussian or Levy distribution respectively. Insets represent the perpendicular self-van Hove function at the Nematic phase.*

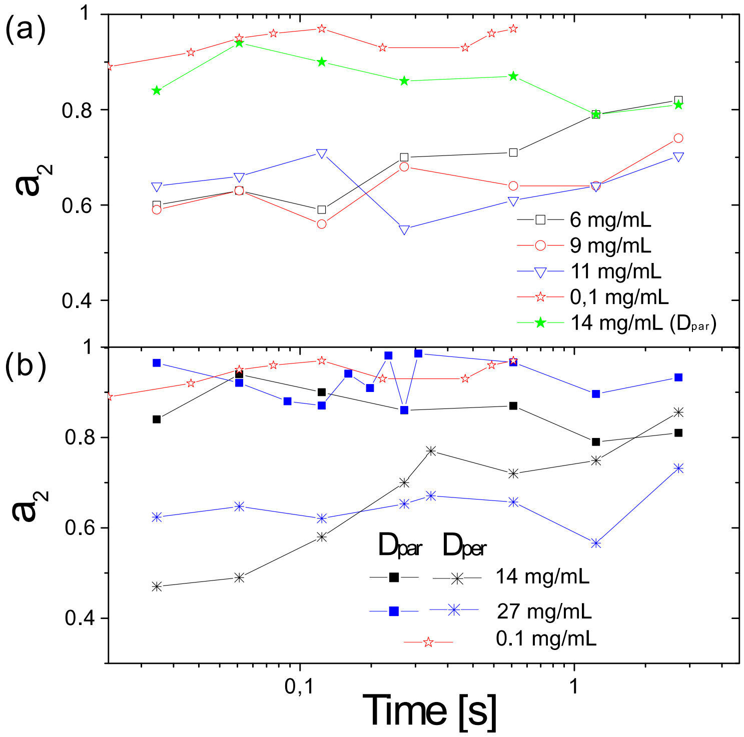

Figure 4.9: *Parameter a_2 obtained from the fitting of the normalized self-van Hove function as a function of time. a) Isotropic concentrations b) Nematic parallel (solid symbols) and perpendicular (star symbols). The open red stars represent the reference close to the dilute regime* $0.1\ mg/mL$*, where the behavior is almost Gaussian so values of a_2 are close to 1.*

shown that the dynamics are heterogeneous. This is reflected in the self-van Hove function, which behaves as Lévy-flight distribution [120–122] in contrast with Brownian particles that have a Gaussian shape. The change in the shape of the self-van Hove function is connected with the diffusivity of the system [123, 124].

In Fig.4.8, we have represented the self-van Hove function (left) and the corresponding normalization (right) at different concentrations around the I-N phase transition. In the semi-dilute isotropic regime (6, 9 and 10 mg/mL) just before the I-N phase transition, the self-van Hove function takes a *roof-tent* or Lévy-flight shape. After the phase transition, in the Nematic phase the parallel self-van Hove recovers to Gaussian-like. Contrary, the perpendicular self-van Hove function remains non-Gaussian.

We characterize the evolution from Gaussian to a Lévy-flight distribution by analyzing the Self-Van Hove (described in details in Chapter 1), with a method developed by Wouter den

Otter (University of Twente, private communications). We normalize the self-van Hove function by multiplying the probability by $\sqrt{dt}$ and dividing the position by $dz/(\sqrt{dt})^2$. This will take out the effect of time, so the curves will be comparable, and the fitting is done by using the following expression:

$$Ln(G(z,t)\sqrt{dt}) = a_0 - a_1(\triangle z^2)^{a_2}; \tag{4.3}$$

where a_2 is 0.5 for Lévy-flight and 1 for Gaussian respectively, and a_1 is related to the inverse of the D_i when $a_2 = 1$.

We focus first on the time dependence of the a_2 parameter since it is related with the diffusivity of the system, represented in Fig.4.9, taking the Gaussian behavior at 0.1 mg/mL as a reference. In the Isotropic phase at 6 mg/mL the a_2 parameter is initially low and recovers to $a_2 = 0.8$. Close to the I-N at 11 mg/mL it remains roughly constant. In the Nematic phase, a_2 is relatively high $0.8 < a_2 < 1$ for the parallel diffusion. On the contrary, the perpendicular diffusion is below 0.8 and recovers at longer times at 14 mg/mL, and does not change for 27 mg/mL which is deeper into the Nematic phase.

Finally, we represent the parameters a_1 and a_2 for parallel diffusion, as a function of concentration for 3 different times: short (0.03 s), middle (0.24 s) and longest time (2.4 s), as shown in Fig4.10. The a_1 parameter decreases with concentration and after the I-N transition remains rather constant. The a_2 parameter exhibits Gaussian behavior at very low concentrations in the Isotropic phase, with values $a_2 \cong 1$ and drops just before the I-N. In the Nematic phase after the I-N phase transition, the a_2 parameter for the parallel diffusion jumps to higher values and increases continuously with concentration to values close to 0.9 or Gaussian behavior. Furthermore, the data exhibit a big decay after I-N for short times, while at long times the curves before and after I-N converge.

This transition from restricted dynamics with a low value of a_2 to a diffusive state with more free volume in the Nematic phase is the dynamic signature we were after for the I-N phase transition.

Thus, we conclude that this behavior is caused by *tube effect* in the dense Isotropic phase before the I-N Phase transition, where the high particle packing restricts diffusion. This is

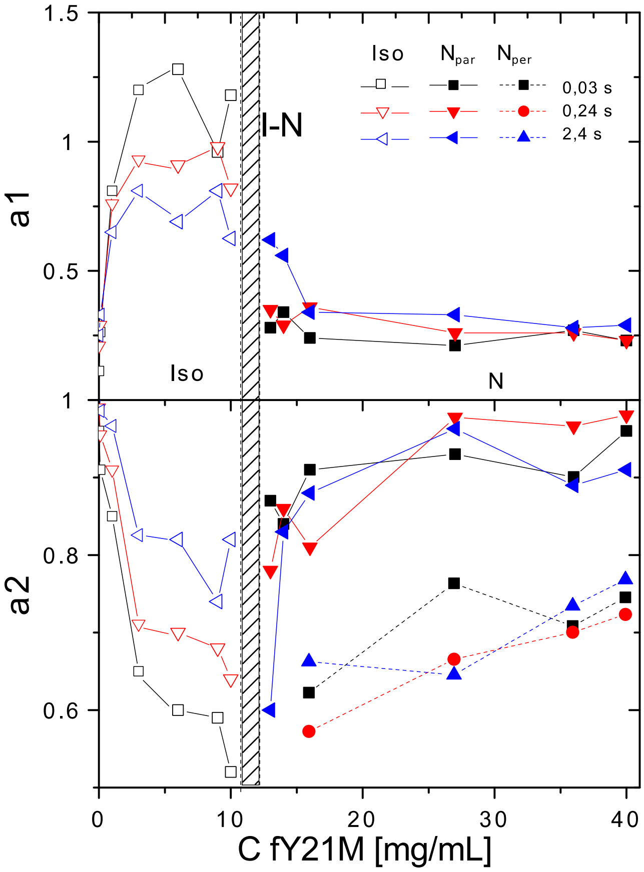

Figure 4.10: *Concentration dependence of a_1 and a_2 parameters obtained from the Normalized self-van Hove function at different time steps: 0.03 s (black), 0.24 s (red) and 2.4 s (blue). The slash lines determine the I-N phase transition.*

further confirmed with a general calculation of the deviation from the Gaussian behavior, the non-Gaussian parameter,

$$\alpha_2(\Delta t) = \frac{\langle \Delta x^4 \rangle}{3\langle \Delta x^2 \rangle^2} - 1, \tag{4.4}$$

where the second and fourth moments of a 1D $P[\Delta x(\Delta t)]$ are combined, being zero for a Gaussian distribution. In Fig.4.11 we show the values of α_2 as a function of time in the Isotropic phase. We observe that α_2 changes its behavior from dilute Isotropic to the semi-

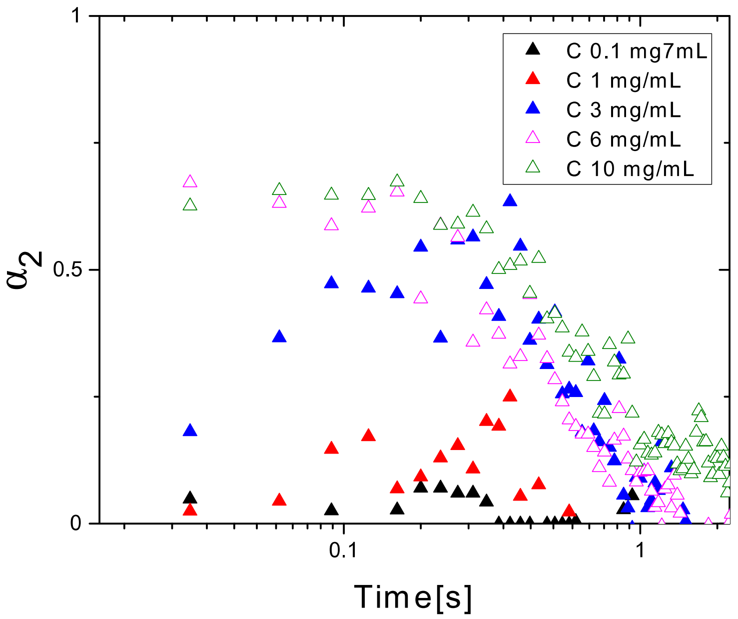

Figure 4.11: *Time dependence of the non-gaussian parameter α_2 calculated for different concentrations in the Isotropic phase.*

dilute Isotropic regime. At high concentrations in the Isotropic phase, there is a rise of α_2 which indicates the slowing down of the dynamics, approaching the phase transition. Interestingly, this behavior has been observed by Weeks *et al.* for the glass transition of spheres [53]. In his work Weeks showed how close to the glass transition there is a rise of α_2 and it dramatically changes the behavior in the glass state, where α_2 shows immediately a decrease and then it drops at longer lag times, as we observed for 6 and 10 mg/mL in our results. The main difference is that our system does not undergo to a glass state, but this glass state behavior is prior to the I-N phase transition.

4.5 Nematic-SmecticA Phase Transition

Contrary to the I-N phase transition which is clearly first order as demonstrated by the existence of tactoids, the Nematic-Smectic phase coexistence is not that evident. Generally, DIC microscopy is used to identify characteristic layered pattern of the Smectic phase, which can be distinguished from the Nematic texture characterized by the birefringence and the absence of layers.

In our sample, we found a N-Sm phase coexistent between 87 and 91 mg/mL, which is consistent with literature [19, 29]. At 87 mg/mL we observe clearly Nematic regions mixed with small Smectic regions, and at 91 mg/mL the Smectic region dominates while small Nematic regions can be distinguished. In this range of concentration, we want to study the underlying dynamical behavior of the rods to demonstrate that the order phase transition can be dynamically identified.

4.5.1 Analysis of dynamics throughout the phase transition

We proceed to the specific analysis of dynamics of the N-SmA Phase transition. The most noticeable difference in the dynamics between the N-Sm phase transition is that in the Nematic the motion is continuous while in the Smectic phase particles exhibit jumps.

In figure 4.12 we show four different types of trajectories that we find at 87 and 91 mg/mL: a) Continuous Nematic-like diffusion; b) *smooth smectic* trajectory, where a transition between layers has intermediate points, such that our algorithm cannot identify as a jump; c) pure smectic trajectories where jumps are clearly recognized (the residence time τ is indicated by the green line); d) Mixed trajectories, in which we observe both Nematic and Smectic-like behavior. These are most likely particles that get into or out of a defect, see below.

In Fig4.13a we represent the trajectories that are characteristic of the N-Sm Phase transition. We color code them (green: pure Smectic, red: pure nematic and pink: smooth Smectic) and overlay them with DIC pictures. These types of trajectories are distinguished using the step-detect algorythm, which identifies the sharp transitions of the Smectic jumps from the continuous Nematic diffusion. The smooth smectic are trajectories which the jumps have a very short residence time and the transitions start to be less sharp, so then the program

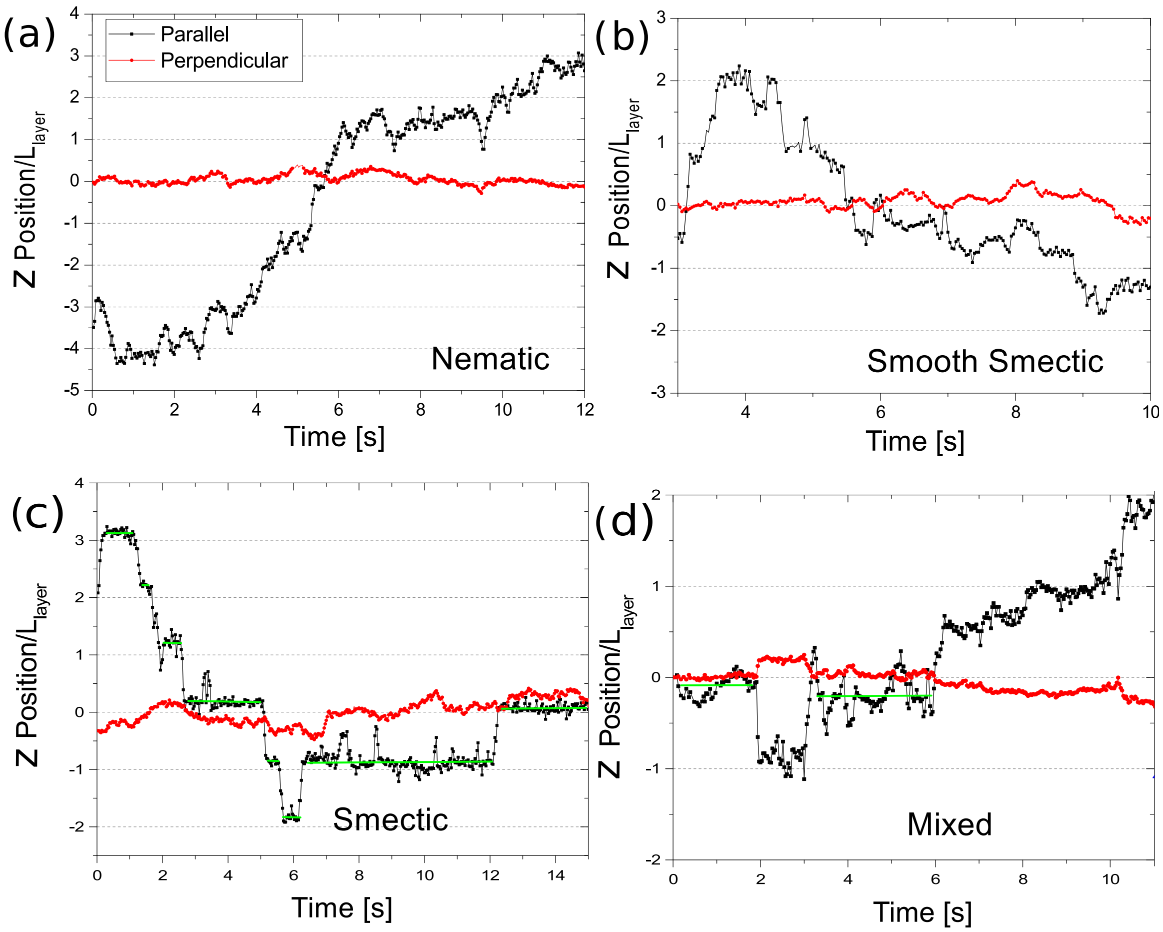

Figure 4.12: *Typical trajectories found in the N-Sm phase transition (87 and 91 mg/mL): a) Nematic, b) Smooth Smectic c) Smectic d) Mixed trajectories. Parallel (black line) and perpendicular (red line) diffusion are represented as a function of time. For Nematic and smooth Smectic jumps are not recognized by the Step-detection program contrary to the Smectic were clear jumps are observed. The position is normalized by the* $L_{layer} = 0.92\ \mu m$. *Horizontal lines indicate adjacent layers.*

cannot identify them. As we can observe for 87 mg/mL, we have two types of regions: no Smectic layers with Nematic-like trajectories, and Smectic layers with smooth Smectic-like trajectories. Mainly we get pure Smectic, pure Nematic, and smooth Smectic trajectories. At 91 mg/mL, we have regions of clear coexistence of Smectic Smooth Smectic, and we have a few number of Nematic trajectories. The mixed trajectories are not considered since they have been observed only in highly defected regions and will be discussed more extensively later in this Thesis.

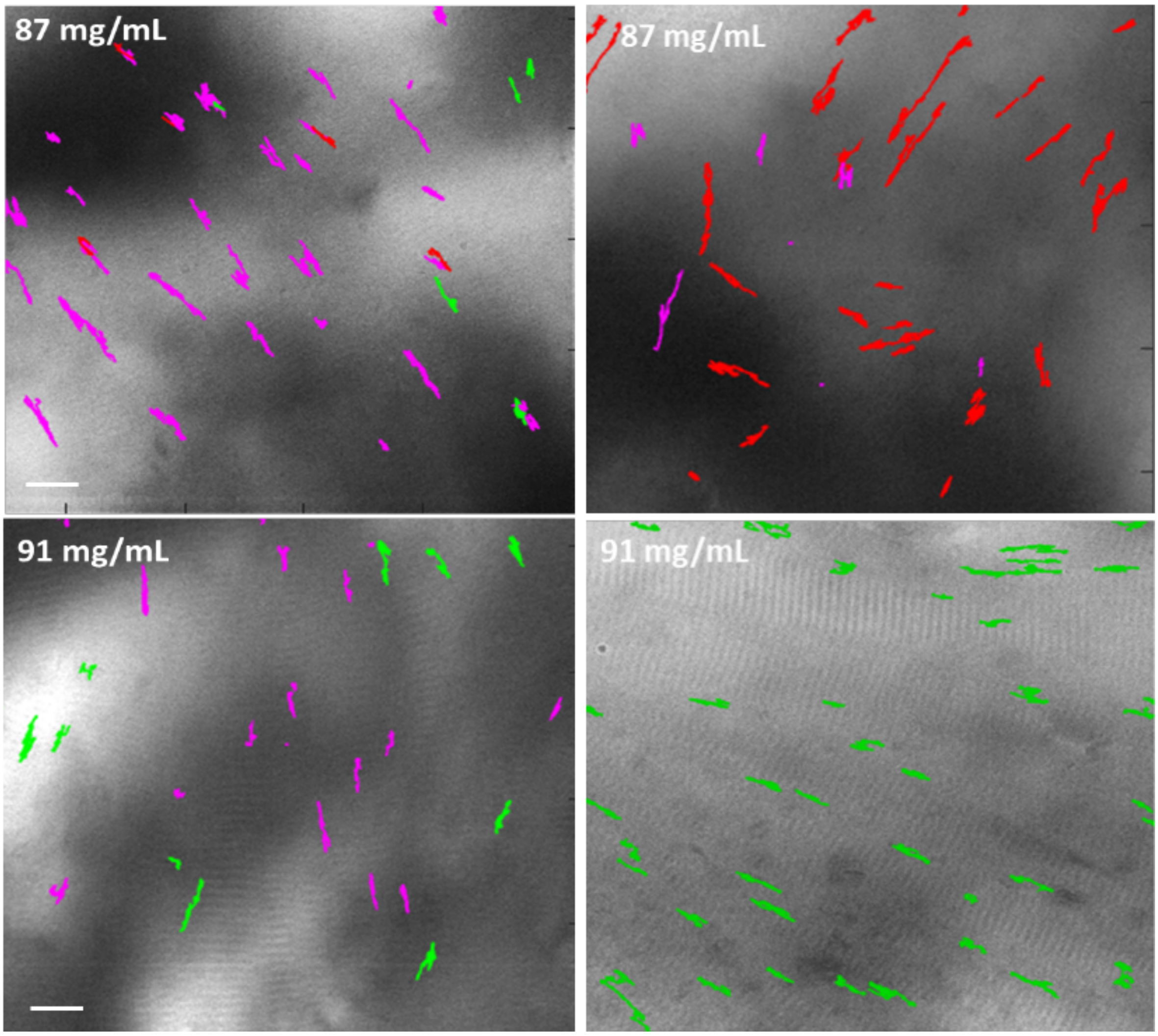

Figure 4.13: *Overlaying DIC picture of and fdY21M trajectories. Upper figures: first concentration N-Sm phase transition (87 mg/mL). Bottom figures: second concentration N-Sm phase transition (91 mg/mL). Green trajectories represent pure Smectic trajectories, violet trajectories are Smooth Smectic trajectories, and red trajectories are pure Nematic. At this concentration, Smectic layers start to fade (left), and there are regions where they are not observed (right). Scale bar indicates 5 μm.*

These observations suggest a N-SmA dynamical phase coexistence. However, we need to quantify the differences between the trajectories labeled as pure Nematic and smooth Smectic, as the step-detection is not conclusive. The program may have limitations due to the short time residences found in the smooth smectic trajectories. We again evoke the use of the self-van Hove, as it is distinctly different for both types of trajectories, as shown in Fig.4.14.

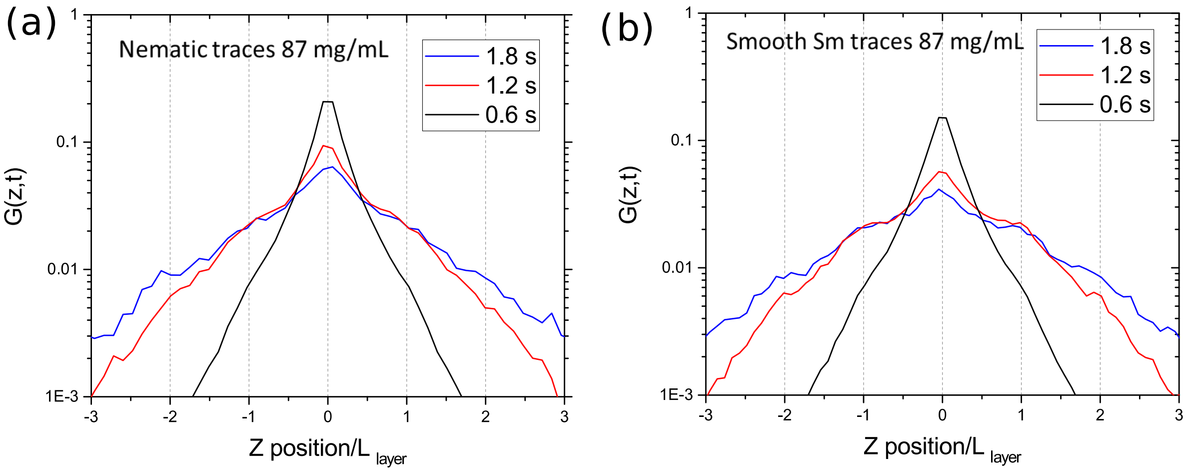

Figure 4.14: *Self-Van Hove function after the distinction of the dynamics for 87 mg7mL. a) Profile for the Self-Van Hove of the pure nematic like trajectories. Number of particles: 117 b) Profile of Self-Van Hove function of smooth Smectic trajectories. Number of particles: 541. Typical discrete peaks are shown at one layer distance for the smooth Smectic Self-Van Hove. 5ms data is included to increase statistics.*

In Fig.4.14a we plot the self-van Hove corresponding to the Nematic trajectories (red) and in Fig.4.14b the smooth Smectic-like trajectories (pink). Despite the fact that for smooth Smectic trajectories the jumps are smooth, discrete peaks show up in the self-van Hove function at one adjacent layer distance, which is not present in the self-van Hove of the pure Nematic trajectories. However, this difference is not as clear as for the pure-Smectic self-van Hove function where sharp peaks are exhibited.

Once the trajectories are categorized, we plot the fraction of the different trajectories as we go from the Nematic into the Smectic-A phase, as shown in Fig.4.15. In the Nematic phase, pure Nematic trajectories predominate. At 87 and 91 mg/mL we have a coexistence of both classes of trajectories. This is our dynamics proof of Nematic-Smectic phase coexistence as we set out to do. Moreover, the limitation to clasify the smooth smectic could be the accuracy of the step detection algorithm for Smectic jumps at the phase transition, where residence times are very short. As said before, the Mixed trajectories, which are the ones that diffuse in or out from a defect, are in small percentage and only appear in highly defected regions in the Smectic-A phase.

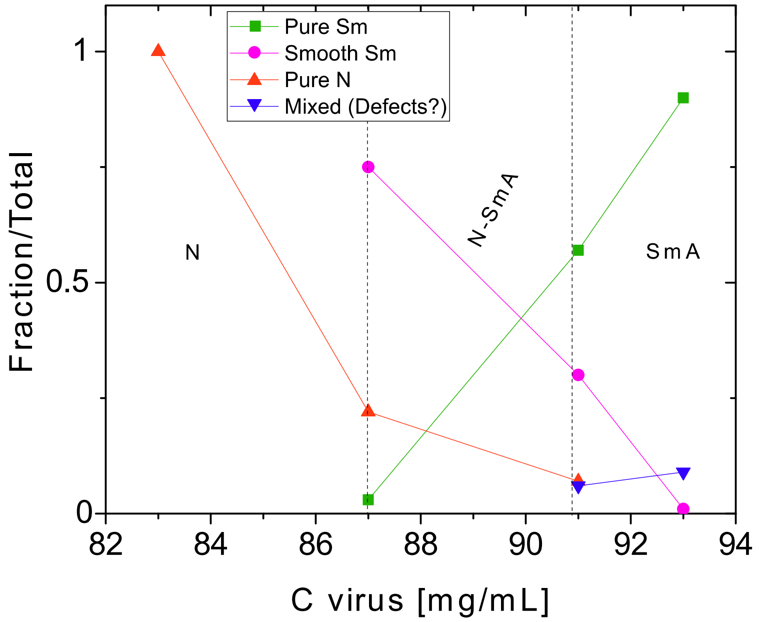

Figure 4.15: *Ratio of pure smectic (green squares), pure Nematic (red triangles), Smooth Smectic (pink circles) and mixed (blue triangles) over the total number of positions as a function of concentration. Dashed vertical lines indicate phase transition limits. Number of particles used at each concentration is around 300.*

4.5.2 Calculation of Smectic Ordering Potentials

In addition to the dynamics, we characterize the N-SmA phase transition by first quantifying the energy barriers imposed by the Smectic ordering, as they strongly influence the dynamics. The Smectic potentials U_{Layer} are obtained from the probability $P(z)$ of finding the particle with respect to the middle of the layer parallel to the director and subsequently using the Boltzmann factor,

$$P(z) \sim e^{-U_{Layer}(z)/k_bT}. \tag{4.5}$$

where k_B is the Boltzmann constant. $P(z)$ is experimentally obtained from the fluctuations within the layer as shown in Fig.4.3. For this purpose, we use a step-detection algorithm which finds sharp transitions of one-rod length between two points within the trajectory which we

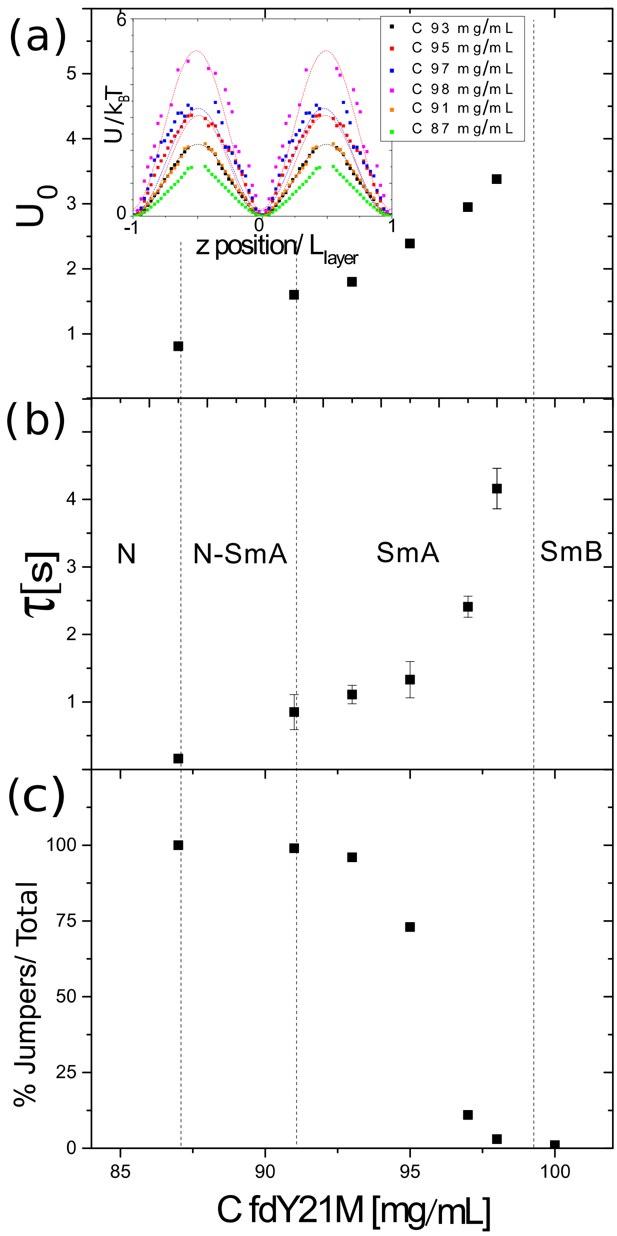

Figure 4.16: *Concentration dependence of a) Smectic potential barriers U_{Layer} devonvoluted from the psf. Inset shows raw data for all Smectic concentrations; b) Residence time τ; c) Ratio of jumpers over no-jumpers. The vertical dashed lines represent the phase transitions.*

call *jump*. With this methodology, we identify many time windows corresponding to the time that the particles stay in the layer between jumps (or the so-called the *residence time* τ), and we measure the fluctuation within the layer.

The values of the potentials obtained from deconvolution of the raw data from the point spread function (see Appendix), are represented as a function of concentration in Fig.4.16a. U_{Layer} decreases with decreasing concentration, due to a higher packing between layers. At the concentration in the N-Sm phase transition close to the Nematic phase ($87mg/mL$), the value of U_{Layer} drops below $1k_bT$. A similar trend is observed in the residence time τ_{res} as shown in Fig.4.16b , which is the average time that a particle stays within the layer. The τ_{res} follows the same trend that the scape rate of Kramer's escape theory [125]. Moreover, the ratio of jumpers over a total number of particles is represented, as shown in Fig.4.16c. The number of particles that jumps through the layers correspondingly decreases with increasing concentration.

4.6 Smectic A-Smectic B Phase Transition

At high concentrations in the Smectic phase, the dynamics freezes as we showed by looking at the concentration dependence of the diffusion coefficients and exponents in the first section of the chapter. It is conceivable that this is related to the formation of the crystalline Smectic-B phase. So far, the way to recognize the Smectic-B phase is by using SAXS [19]. While in the Smectic-A mesophase particles have short range ordering or liquid like within the layer; in Smectic-B a long range crystalline order is found. Here we will dynamically recognize the possible co-existence of Smectic-A and Smectic-B phases looking at their different dynamical behavior.

Before we discuss the analysis of the dynamics, we further investigate the structure of the phase using DIC microscopy. This technique, instead of quantifying the packing of the rods which is obtained by SAXS, quantifies the packing between layers which is characterized by the layer spacing λ. We obtain λ from the FFT (fast Fourier transform) of the DIC pictures. The value of the radius from the center of the FTT to the first and second harmonic intensity signal is related to the value of the layer spacing λ (Fig.4.17). For each concentration, we have measured 12-15 values of layer spacing.

The concentration dependence of the layer spacing λ and the normalized layer spacing λ/L_{rod}, are shown in (Fig.4.18). There is a slight change of slope between the SmecticA and the SmecticB phase, which can be related to a different packing density, due to the confine-

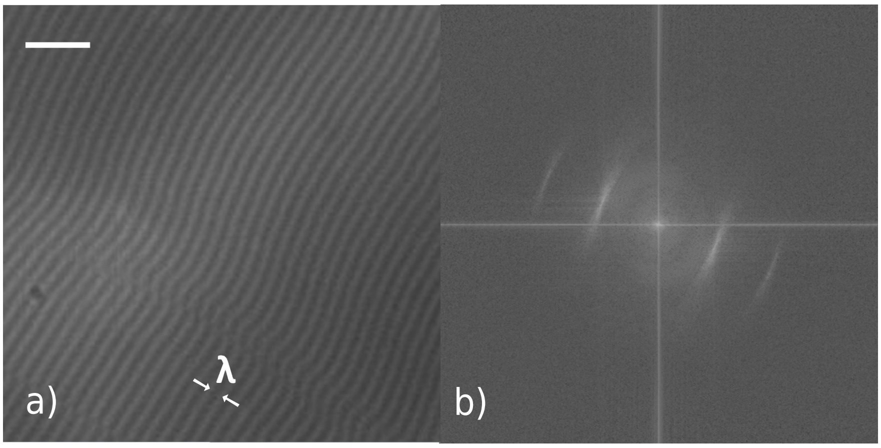

Figure 4.17: *a) Region of interest (ROI) of a DIC picture of the Smectic phase formed by the host system fdY21M at 98 mg/mL. Layer spacing λ at this volume fraction is 0.95 μm. Scale bar indicates 5 μm. b) Corresponding Fast Fourier Transform (FFT) of original field of view left picture (2048x2048, binning 1, 100x, exposure time 50 ms, NA=1.4) of the Smectic system at 98mg/mL. The quantification of the lengths of the Smectic layer spacing has been done performing the FTT of the DIC pictures.*

ment within the layers induced by the high rod density [19]. At concentrations higher than 110 mg/mL, within the range of Smectic-B mesophase, λ/L_{rod} reaches 1, which means that the system is highly packed. These results, however, are not consistent with the previous measurement, where the difference of slope of λ_L between SmA and SmB phases is not that dramatic [19].

We now want to relate this difference in the packing with the dynamic behavior. As mentioned before, D_i and γ drop to zero at concentrations corresponding to the Smectic-B phase. This is also reflected in the values of τ, which diverges due to the residence time of the particles, which do not move from the layers, as shown in Fig.4.16. Nonetheless, we do have to be cautious with this latter statement due to the limited total time of observation, due to practical issues (photobleaching, memory, etc...). In this total time, most of the particles do not exhibit jumping-like behavior (non-jumpers). This poses the question if for those particles we do not observe jumps due to the limited time of observation (15 seconds), or they are completely stuck in the layer because they belong to the Smectic-B phase.

Hence, we want to distinguish the particles that jump and the particles that do not jump due to the lack of dynamics. We assume that there will be a considerable difference between the fluctuations within the layer of the particles that jump (even if do not track the jumps during

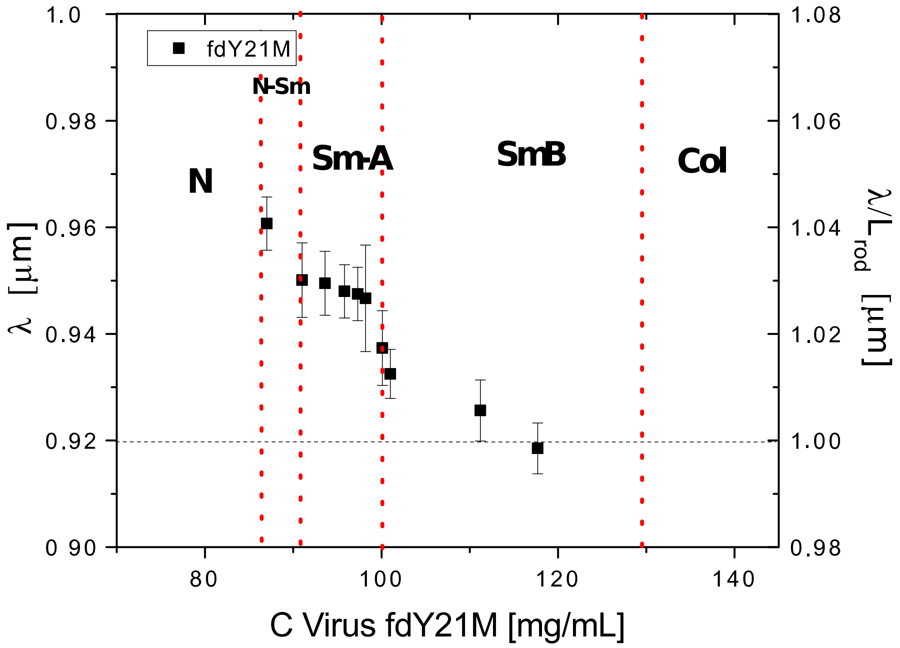

Figure 4.18: *The layer spacing λ as function of concentration. Left axis indicate the raw data and right axis the normalization $\frac{\lambda}{L_{rod}}$, $L_{rod} = 0.92\mu m$. The Smectic layered pattern starts to be observed after the SmecticB-Columnar phase transition at around 138 mg/mL and it vanishes when the Nematic-Smectic phase transition finishes at 87 mg/mL.*

the time window of the movie), and the particles that are in the Smectic-B and consequently do not show any dynamics. Thus, if we analyze the dynamics, we can track this difference and classify the type of particle. It is important to remark that we take as a reference for the Smectic-B phase (no dynamics) the data at 100 mg/mL, to compare the results obtained within the layer.

First, we make a distinction between the particles that exhibit jumps during the total time of the movies and the ones that do not exhibit any jump. Then, we obtain the dynamics of the jumping particles within the layer from isolated time windows during the residence time τ, represented by the green line in Fig.4.19b. Also, we obtain the dynamics of the non-jumping particles from the full trajectory, as shown in Fig.4.19c.

In figure 4.20 the linear representations of the MSD_{Layer} parallel and perpendicular for jumping and non-jumping particles are represented. Indeed, the MSD shows two different behaviors. For non-jumping particles only at 93 mg/mL, we observe some motion while for

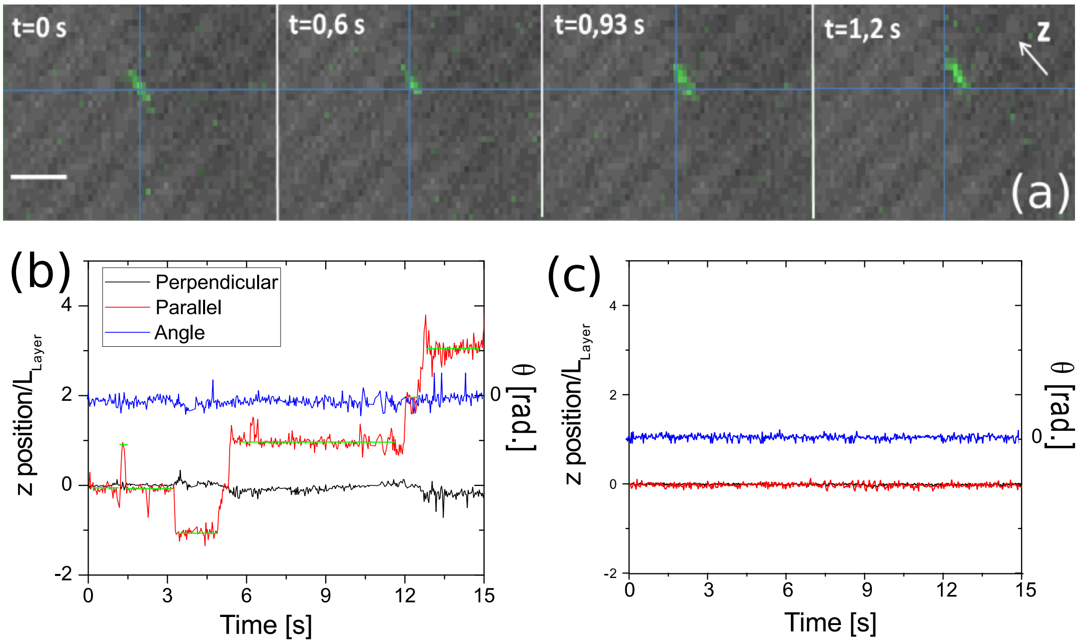

Figure 4.19: *Diffusion within the layer examples. a) DIC and fluorescence overlaying pictures at different time steps of a particle that diffuse within the layer. The blue cross is the reference starting point. The white arrow indicates the director* ***n****. Scale bar: 2 μm. b) Smectic-like trajectory as a function of time. The green line represents the time residence window where the analysis within the layer is performed. c) Typical trajectory of a non-jumping particle, which stays within the layers during the total movie time.*

higher concentrations the MSD remains at approximately zero. At the same concentration, we see almost free but sub-diffusive behavior for the particles that we classify as jumping particles.

The diffusion coefficients have been extracted from the slope of the MSD_{Layer}, using Eq.4.2. The $D^{||}_{layer}$ and $D^{\perp}_{layer}$ for jumping-particles have values that follow the same trend, but they are somewhat lower than for full trajectories due to the discrimination of the jumps. Compared to the full trajectories, the main difference is that the diffusivity γ is glass-like for the dynamics within the layer, as shown in Fig4.21.

On the contrary, the diffusion rates within the layer for the non-jumping particles show that from 95 to 98 mg/mL motion is almost prohibited, as we observe for the full SmecticB at 100 mg/mL. Also, γ drops below 0.5 for the glassy state which confirms that these particles are in the Smectic B phase, as shown in Fig.4.21. Interestingly, this is first observed at 95 mg/mL for the parallel diffusion, which means that the parallel diffusion is the first to be fixed

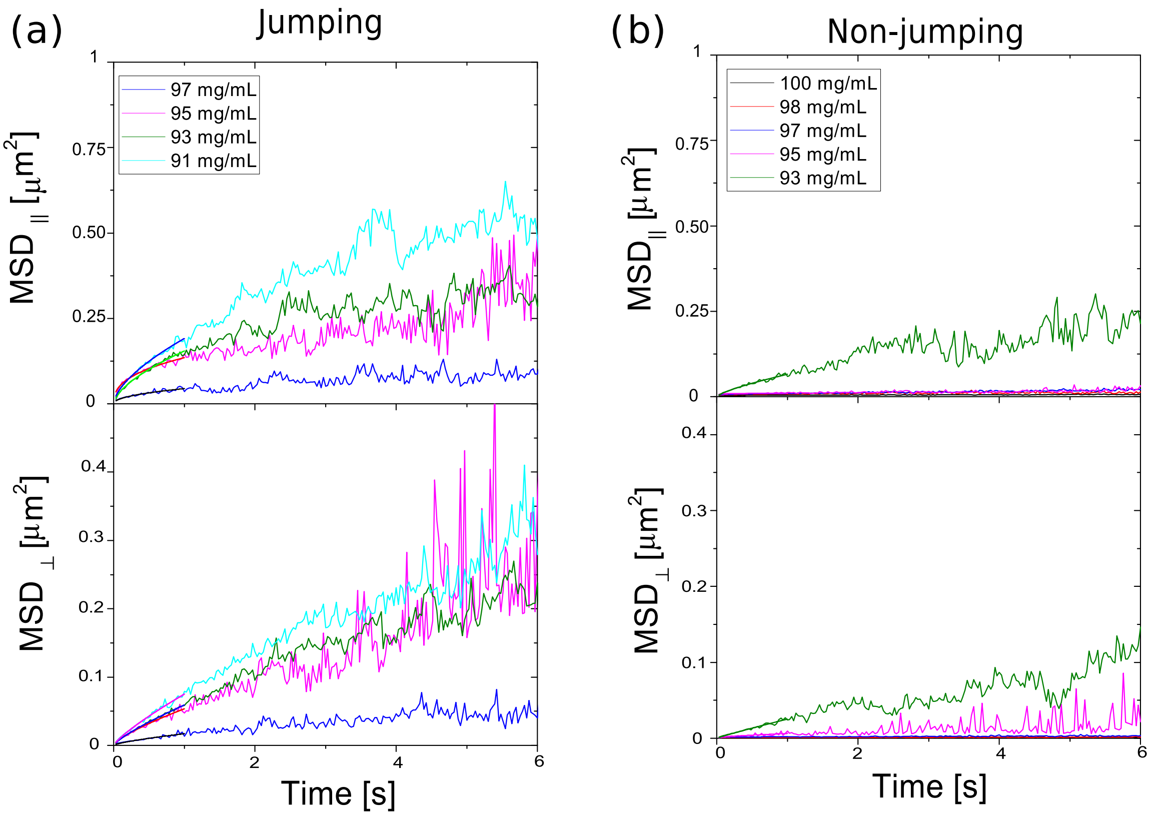

Figure 4.20: *MSD raw data within the layer for a) jumping particles and b) non-jumping particles. Non-jumping particles are in the range of Smectic-B concentration for the Host fdY21M. Subdiffusive behavior is reflected in the change of slope of the MSD. Each MSD is calculated for around 300-350 particles. Solid lines indicate the fitting with the power law* $\langle r_i^2(t)\rangle = 2dD_i t^{\gamma_i}$.

on its crystal lattice point. Therefore, it is safe to assume that the non-jumping particles belong to the Smectic-B regions. We can now complement the phase diagram as shown in Fig.4.21 with the fraction of non-jumping particles which reaches 1 when entering the pure Smectic-B, as shown in Fig4.22. This figure clearly shows that there is phase coexistence of SmA-SmB in a quite broad concentration range.

However, at this concentration, the homogeneity of the sample can affect the results. One could argue that this dynamic co-existence is due to the poor homogeneity when preparing the sample. Although we follow an experimental protocol for sample homogenization, it is hard to tell at this state of the sample.

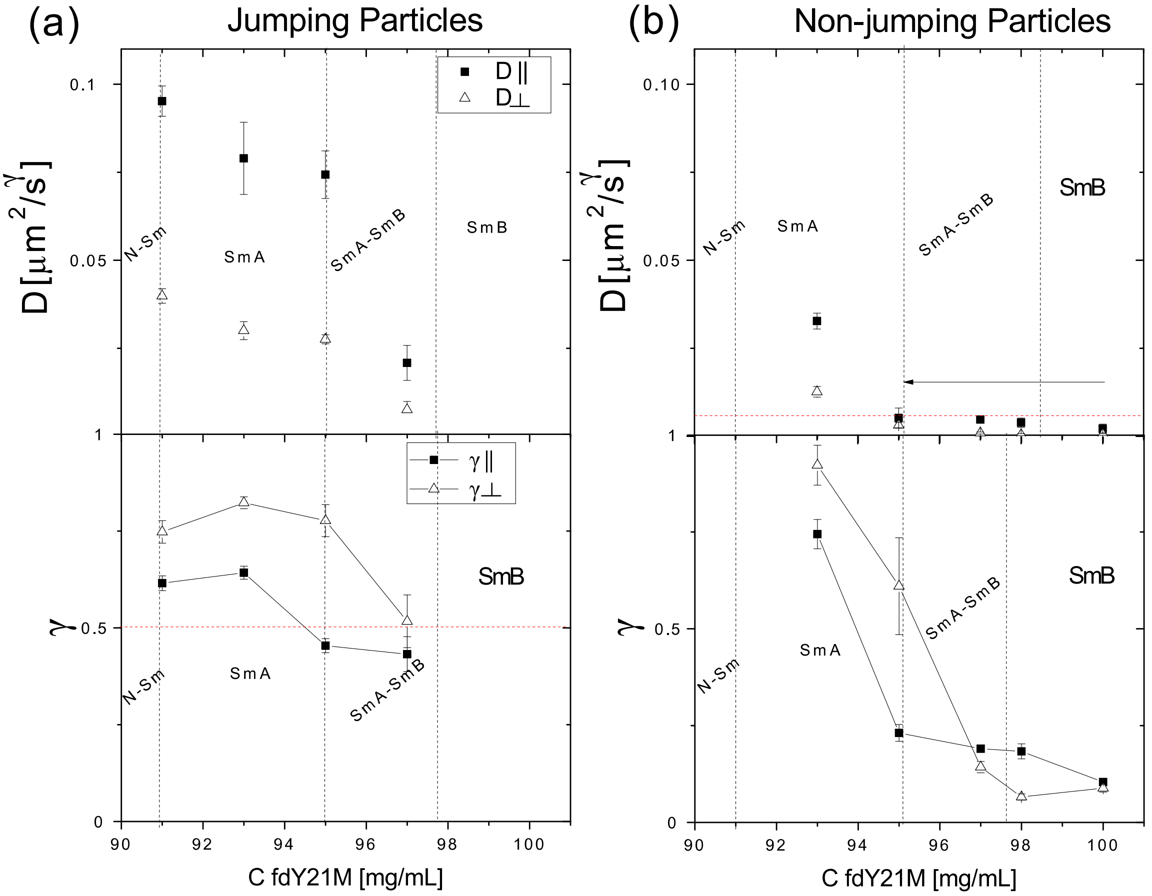

Figure 4.21: *Concentration dependence of D_i (upper figures) and γ_i (bottom figures) within the layer for a) jumping particles b) non-jumping particles within the total time of the movie. Parallel diffusion is represented with black solid squares and perpendicular with open black triangles. Horizontal dashed line indicates the value for particles in SmB phase. The arrow indicates the range of concentration where SmB dynamics are found. Horizontal dashed line indicates the value at which the glass transition occurs. Vertical dashed lines indicate the phase boundaries. Each data point is calculated for around 400 particles.*

4.7 Discussion and conclusion

In this chapter, we have presented an overview of the dynamics of the rod-like fdY21M particles at the different phase transitions: I-N, N-SmA, and SmA-SmB.

In Sec.4.4 we use the self-van Hove function to characterize the dynamic signature of the *I-N phase transition*. We found that the Brownian motion is very much restricted in the Isotropic phase close to the I-N phase transition as characterized by $a_2 \rightarrow 0.5$. The same behavior has

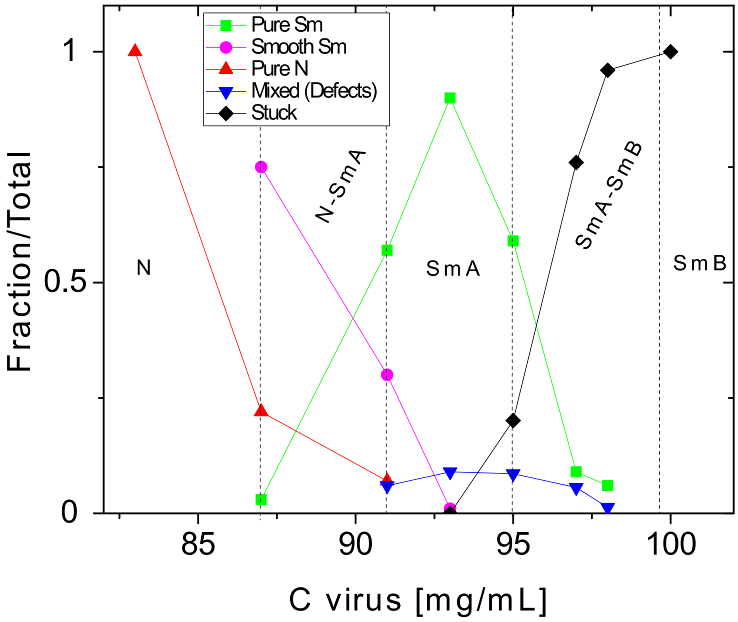

Figure 4.22: *Ratio of pure smectic (green squares), pure Nematic (red triangles), Smooth Smectic (pink circles), mixed (blue triangles) and SmB particles (black diamonds) over the total number of positions as a function of concentration. Dashed vertical lines indicate phase transition limits. Number of particles used at each concentration is around 300.*

been observed for colloidal glasses [53, 70], which hints to heterogeneous dynamics. Hence, this effect could be a signature of the *tube effect* [51], where particles are confined by their neighbours until they reorient to find the path they can diffuse through. The Gaussian behavior is recovered after the phase transition in the Nematic phase for the parallel diffusion, which is promoted by the orientational order of the phase [26]. The perpendicular diffusion remains sub-diffusive.

In Sec.4.5 we use the different behavior of the trajectories in the Nematic phase (continuous motion) [26] and Smectic phase (jumping-like motion) [28, 29] to characterize dynamically the N-SmA phase transition. Phase transitions can be first order, where both mesophases are in coexistence in equilibrium (as it is clearly observed for I-N Phase Transition). On the contrary, second order phases transitions are continuous and do not exhibit phase coexistence. We distinguish dynamic coexistence in the range of the N-SmA phase transition, which is also observed by DIC microscopy. Hence, the experiments support that the N-SmA phase transition is first order as proposed in previous studies [8, 9]. We tried also to characterize the *smooth* *smectic* trajectories, for which the program cannot recognize the jumps because they are not as sharp as the the pure Smectic ones. The self-van Hove function is used to do so (Fig.4.14). Even though the self-van Hove for the Smooth Smectic trajectories exhibits discrete peaks observed at one adjacent layer distance, they are not as sharp as the pure Smectic trajectories. It makes difficult the comparison with the pure Nematic phase.

Finally, in In Sec.4.6 we investigate dynamics at the *SmA-SmB phase transition*, for which the *layer spacing* λ_{layer} suggests a different packing of the layer between both phases, in addition to the lateral particle packing studied by SAXS [19]. We show that this change of packing density affects the dynamics as the diffusion rates and exponent drop to zero. When comparing the dynamics within the layer for *jumping* and *non-jumping* particles, we find a dynamic coexistence in a region with an appreciable width. Thus, a complete phase diagram which represents the fraction of particles in each mesophase and at the phase transitions is presented in Fig4.22. At each phase transition, we have a coexistence of two populations of trajectories, corresponding to the phases at both sides of the transition. However, one could argue that our observations are due to insufficient mixing after dilution, especially at SmA-SmB phase transition where the sample is very dense. Although there is a procedure of homogenization during the sample separation, there could be regions where the sample is not perfectly homogenized.

4.8 Appendix

For the acquisition of fluorescence movies of our system, we used two different exposure times: 20 and 5 ms. The corresponding frame rates for our instrument resolution are 33 and 180 fps for 20 and 5 ms respectively. For the data at 5ms, we used a region of interest (ROI) of approximately 1200x430 pixels. Residence time (τ_{res}) and potential are strongly related, since the potentials are calculated from the fluctuation within a determine τ_{res}. However, as shown in Figure 4.23, τ for 5 ms is lower than for 20 ms movies, while the potentials obtained for 5 ms and 20 ms are consistent. Low exposure times allow us to make fast movies (which means increasing the frame rate), but the length of the movie decreases. Our effective time window for 5ms movies is 3-3.5 seconds (depending on the movie), although the movies are 6 seconds long. Despite the fact that we use the same conditions as for 20 ms, at this exposure time the

Signal to Noise Ratio (SNR) or contrast value between the intensity of the particles and the background noise decreases. Hence, the effect of photobleaching becomes more apparent.

If we look at 20 ms movies, we have a distribution of residences times where we find values above 3 or 4 seconds, but also shorter times. When we calculate the average of this probability, we take into account all of these different values.

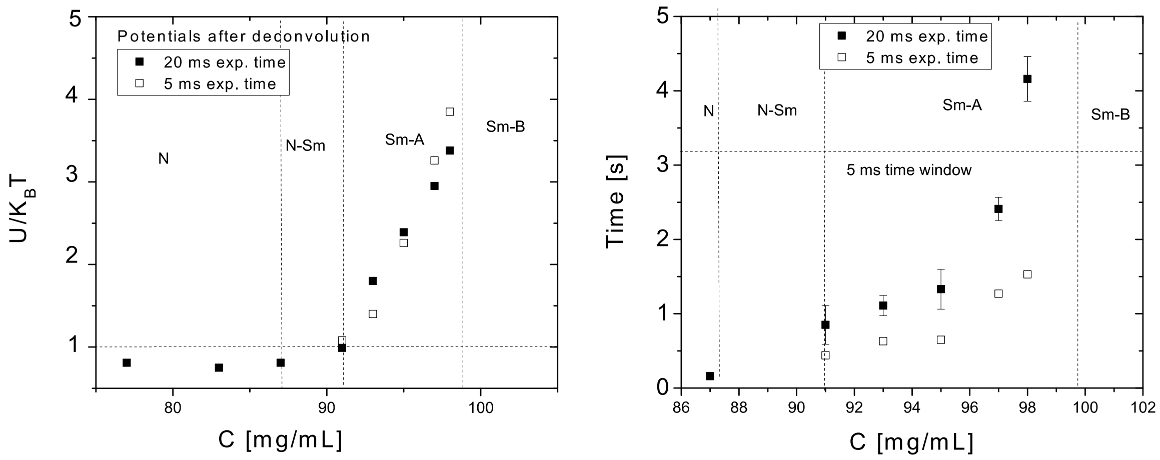

Figure 4.23: *Concentration dependence of Potentials and τ_r for 5 and 20 ms expsosure time.*

The fact that at 5 ms our time windows is reduced to 3 seconds results in a cut off for the long residence times, see Fig 4.24. Hence, particles that stay in the layer a time longer than 3 seconds will not be accounted as a jumper, but as stuck particles, because within these 3 seconds, they do not jump. However, the short residence times are taken into account (those values are also in 20 ms movies), biasing the final result.

An advantage of using high time resolution is that we can resolve small intermediate jumps. Thus, at small exposure times, we can track smaller time residence events. However, the fluctuations that we find within this small time residence are the same, giving potentials that are consistent with the 20 ms data.

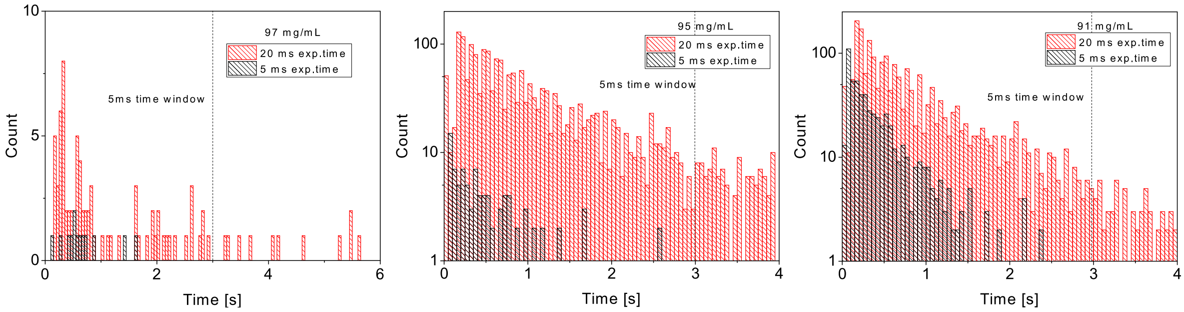

Figure 4.24: *Histograms of residence time in pixels at 97, 95 and 91 mg/mL for 5 and 20 ms exposure time. The vertical dashed line indicated the two different time windows for each exposure time.*

5

Single Particle dynamics of Guest-Host Smectic system of colloidal filamentous particles

In this chapter, we investigate the dynamic behavior of long guest rod-like particles (M13KO7) immersed in liquid crystalline phases formed by shorter host rods (fdY21M). We use direct visualization and tracking at single particle level using fluorescence microscopy, thanks to the presence of labeled viruses. We quantify Nematic-like diffusion of the guest particle for the low concentration of the host Smectic-A phase, confirming that they are not commensurate in the Smectic layers. At higher concentrations, the long particles feel the stronger Smectic potential, and typical discrete peaks in the self-Van Hove functions are observed. In the crystalline smectic-B phase, the long guest particles which are not commensurate with the layer spacing, are still mobile as they generate their own voids in their adjacent layers. These results suggest that dynamics can be controlled by tuning the guest particle size and the packing density of the host system.

5.1 Introduction

Highly dense ordered and crowded systems generally cause a slowing down of the Brownian diffusion of its constituents [54, 126, 127]. There are many studies of this anomalous diffusion which mainly focus on the diffusion of a tracer through an amorphous unstructured host [128]. In many systems, however, there is structure present mainly through self-assembly. Thus the question arises as for how diffusion of a guest particle is altered when the host is ordered. In nature, self-organization of systems into lamellar-like structures is ubiquitous, such as the lateral diffusion of membrane proteins within cell membranes [129]. Many biological systems exhibit lamellar or smectic-like ordering [97] such as chloroplasts and retinal rods [130]. As transport through such structures still needs to take place, the question is whether and how transport of guest particles, which are not part of the structure forming materials, takes place through such highly ordered structures.

Similarly, it has been a long-standing question how diffusion in colloidal crystals takes place, where local mobility [131] at the crystal lattice points as well as vacancies play an important role. In most studies of the transport of guest particles through a structured background, the guest particles are smaller than the typical length scale of the host system, see e.g. simulations [132, 133] and experiments [56, 134–136].

In this chapter, we address the opposite limit from an experimental point of view, e.g. how the mobility of a guest particle is affected by a surrounding energy landscape that has a smaller length scale than the guest particle? For this study, we have defined a model system by introducing tracer amount of long, non-commensurate, guest rods in a host smectic phase comprised from shorter host rods, as schematically represented in Fig5.1. Having long guest particles whose length is higher than the host layer spacing for which $L_{layers} \simeq L_{host}$, implies that the guest rods have to be accommodated in more than one smectic layer, exceeding the typical length scale of the host ordering potential.

It mimics the transport of a *guest particle* through layered structures, the so-called permeation, while it represents diffusion in a less stringently ordered phase than 3-d crystals. As we will consider purely hard core interactions, we assume that the complexity of the experimental model is reduced to a purely entropic problem, where only repulsion interactions between particles will lead a change from an ordered phase to am more ordered phase by increasing the free energy of the system.

From the fact that the particle is non-commensurate only in one layer we expect that the ordering potential that sets the smectic layers will not be the same as for the host particle, and therefore also that the parallel diffusion will be affected. We also expect that the diffusion within the layer will be affected, as the particles have effectively close neighbors stemming from at least two adjacent layers.

Systems based on rod-like fd viruses are ideally suited for this study as they exhibit the full range of liquid crystalline phases [64, 75]. Their size of almost 1 μm allows for detailed fluorescence microscopy studies, while a biological toolbox can be exploited to make particles of different lengths and stiffnesses. This system has been used earlier to study host-in-host diffusion in the nematic [63], smectic phases [27, 29] and columnar phases [96], but also for guest (bead) host (nematic) systems [137]. We will study the diffusion of the mutant M13KO7 as a guest particle in a Smectic ordered phase of the stiff fdY21M. M13KO7 has a contour length of 1.2 μm, which is 1.3x longer than the contour length of fdY21M viruses. When forming Smectic layers, fdY21M particles have a layer spacing of around 1μm so that we expect that the long guest M13KO7 is *accommodated* in more than one Smectic layer. As we have seen in chapter 2 and the work of Pouget *et al.*, anomalous hopping type diffusion between the Smectic layers has been observed for a the Smectic phase of pure fdY21M, rather than diffusion within the layer. This hopping type diffusion takes places in quasi-quantized steps of one-rod length. Thus, the particles exhibit Brownian diffusion confined in a background ordering potential.

The chapter is organized as follows. We start by introducing our guest-host Smectic system and the methodology we use to characterize it. In the first section, we calculate the effective potential for the particles and then investigate its influence on the self-van Hove function, which is a very sensitive measurement to observe the effect of structure on the diffusion. In the second section, we discuss the mean square displacement both for the full trajectory of the particles and locally within the layer, which means that we consider the motion only within the Smectic layer. The results are always compared with the data that we already showed in chapter 4 for the host system. Finally, in section 5.6 we propose an interpretation of the results on the basis of the misfit between the guest particle and the layers that contain it.

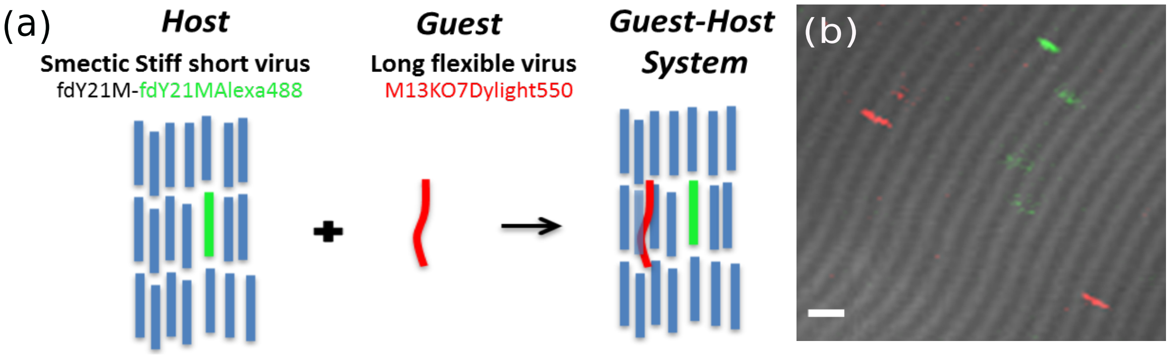

Figure 5.1: *(a) a scheme of the Guest-Host system used in this work. The host system is a smectic phase of fdY21M viral rods, in which we dispersed tracer amounts of labeled short-host (green, fdY21M) and long-guest (red, M13K07) rods, which are 1.3 times longer and about 3 times more flexible than the host rods. (b) Overlay of a DIC image, displaying smectic layers, and Fluorescence microscopy image, displaying the differently labeled particles. Scale bar indicates 1 μm length.*

5.2 Design and detection of Guest-Host Smectic system

In this study, we have used two mutants of fdwt to create our experimental *guest-host system*: fdY21M as host liquid crystalline system and M13KO7 labeled with fluorescence dye as the guest particle. The diameter for both viruses is $d = 6.6$ nm, and due to a genetic modifications in the amino acids of the pVIII coat protein, both mutants have different contour lengths and stiffness. For fdY21M, which we will call short-host, the contour length is $L = 0.92$ μm and for M13KO7, which we will call long-guest, it is L= 1.2 μm [20], so that the ratio $L_{M13KO7}/L_{fdY21M} = 1.3$. The length is characterized by Transmission Electron Microscopy (TEM). To visualize the rods by fluorescence microscopy, we labeled fdY21M with Alexa488-TFP (Invitrogen, MW=884.91 g/mol), and M13KO7 with Dylight549-NSH ester (ThermoFischer, MW=1040 g/mol). The procedure of labeling has been explained in Chapter 3. Both labeled particles were added in a ratio of about 1 labeled particle in 10^5 non-labelled particles (Fig. 5.1). With this ratio, we have around 100 labeled particles in our field of view (1208x1080 pixels) in the range of concentration of the Smectic phase. The *host system* fdY21M was prepared as explained in Chapter 4.

We performed experiments throughout the full phase diagram as described in Chapter 4. Samples were prepared by putting a drop of the sample between two spacers of a height of about 10μm, covering it with a cover slip and shearing it by slight up and down motion for about 10 seconds before the sample was sealed. Note that for smectic samples we observed the segregation with time of the long guest particle into highly defected regions of the sample or in regions containing impurities. This process occurs in more than a few weeks (Fig.5.2). In contrast, the labeled host particles do not show this tendency. Hence we conclude that this segregation is driven by the length mismatch [138], and not by an effective different diameter [46, 139, 140] due to the labeling. Moreover, the amount of labeled particles, and especially of long-guest particles, is so small (ratio $1 : 10^5$) that we assume that the phase behavior of the host system is not affected by adding the tracer particles.

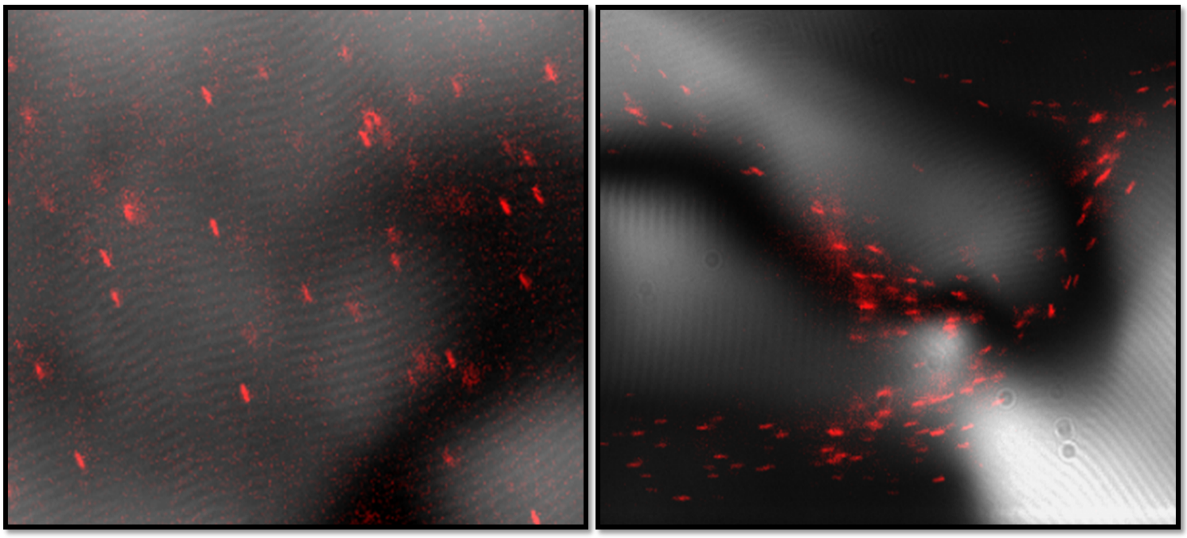

Figure 5.2: *Left: Overlaying of Fluorescence picture of M13KO7 particles with DIC picture at 100x magnification one day after sample preparation. Right: Same sample one week after. We observe how M13KO7 particles tend to aggregate in a inhomogeneous region of the sample.*

Fluorescently labeled viruses were visualized using an inverted microscope (IX-71 Olympus), equipped with a high-numerical aperture (NA) oil objective (100x PlanAPO NA 1.4) and a mercury lamp as excitation light source (X-cite series 120 Q). A dual emission image splitter (Optosplit II Andor) was used to project two identical fields of view, corresponding to the two emission wavelengths, onto an ultra-fast electron-multiplying camera (sCMOS Andor camera). The exposure time was 20 ms, while the maximum length of the movies was 15 seconds. After approximately 6-7 seconds photobleaching of the Alexa488 dyes become apparent. Per concentration, we collect in total around 800 trajectories using a particle tracking algorithm as explained in details (Appendix 1).

Figure 5.3 shows two typical trajectories in the middle of Smectic-A phase (93 mg/mL) for M13KO7 guest (top plot) and fdY21M host (bottom plot). There are a few apparent differences: (1) the long-guests do not display sharp jump events as compared with short-hosts, but still diffuse strongly along their long-axis; (2) diffusion within the layer is more hindered for long-guest than for short-host fdY21M particles. We could also observe that maximum displacement is bigger for the long-guest M13KO7 particles, but this needs to be quantified.

We will try to quantify these observations by comparing the potentials, the self-van Hove functions and diffusive behavior of the guest and host particles.

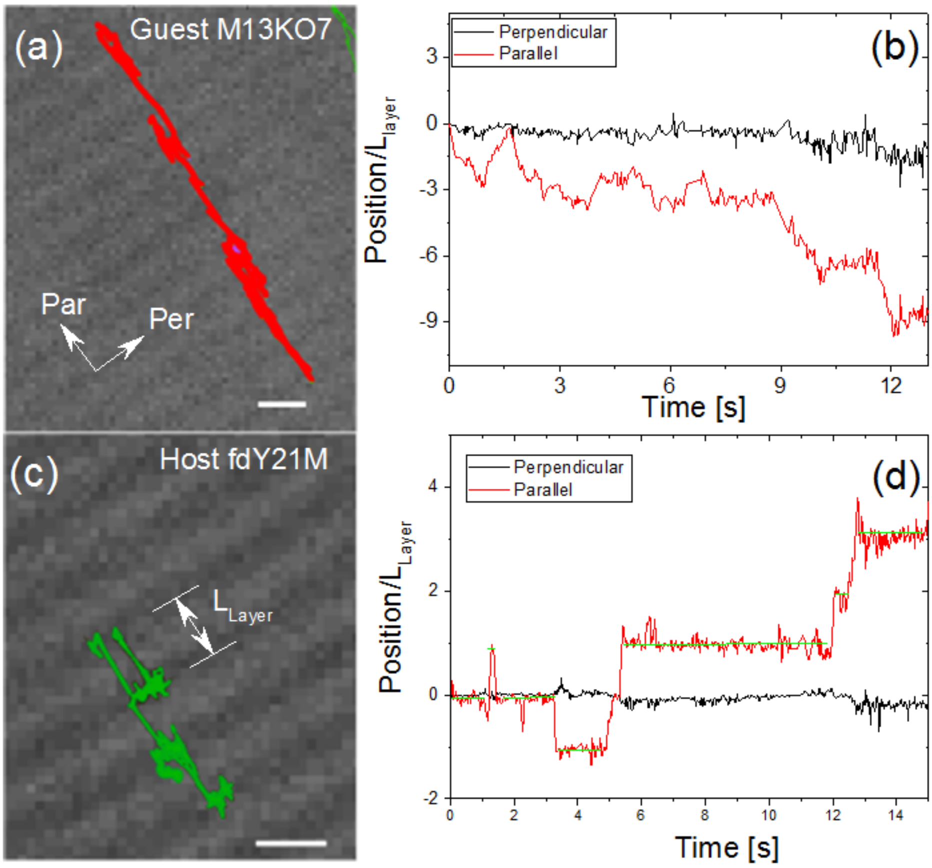

Figure 5.3: *Typical trajectories for guest-M13KO7 and host-fdY21M in the Smectic Phase. [fdY21M=93 mg/mL]. (a) Overlay of a DIC picture and a M13K07 guest trajectory for which rapid diffusion is observed through the layers. (b) Corresponding displacements of the M13K07 rod, parallel (red) and perpendicular (black) to the normal of the smectic layer. (c) An example of a trace for a fdY21M host particle in the lamellar phase of layer spacing Llayer. (d) Associated displacement where jumping type diffusion process is clearly evidenced. The green lines are obtained by the jump-recognition algorithm and define the residence time,* τ_{res}, *that rods spend within a smectic layer before a hopping type event. Scale bars represent 1* μ*m.*

5.3 Calculation of the Smectic ordering potentials

We start the evaluation of our results by calculating the potential that is effectively felt by the non-commensurate particles. The Smectic phase is characterized by an effective periodic energy landscape in one dimension due to the layered ordering. The potential barriers increase with increasing concentration. Thus, the particle has to overcome this barrier to jump from one layer to the adjacent one, exhibiting *"hopping type"* diffusion. We anticipate that this ordering potential will not be experienced to the same extent by the long-guest particles. As explained in Chapters 3 and 4, the Smectic potentials U_{Layer} can be obtained experimentally from the probability $P(z)$ of finding the particle with respect to the middle of the layer parallel to the director (or the fluctuations within the layer) (Fig.5.3) and subsequently using the Boltzmann factor,

$$P(z) \sim e^{-U_{Layer}(z)/k_BT}. \tag{5.1}$$

where k_B is the Boltzmann constant. Fig. 5.4a displays the concentration dependence of U_{Layer} for both particles. While for the short-host the potential increases around the N-SmA transition, as expected, the onset of U_{Layer}^{LG} for the long-guest is shifted to much higher concentrations. Thus, even if there is a background periodic potential, at this density packing of the system the guest particle can permeate through the Smectic layers. U_{Layer}^{LG} continues to increase after the SmA-SmB, while for the short-guest the diffusion freezes and no potential can be obtained anymore. The raw data observed in the inset has been deconvoluted from the optical smearing using the psf(point spread function) that we get from the immobile particles, as we explained in Chapter 2. Moreover, both particles have the same concentration dependence, since the slope is the same from both of potential decays. This is directly reflected in the ratio of jumping particles (particles that do not exhibit jumps within our time window) over non-jumping particles (particles that we are not able to observe jumping within our time window), see Fig. 5.4b. The ratio of jumpers for the short-host starts to decrease after the N-SmA transition and reaches 0 at the SmA-SmB transition, while for the long-guest the decay sets in at higher concentrations and jumpers can still be found in the SmB phase. Similarly, the average residence time τ, which is calculated from the histogram of residence times for all

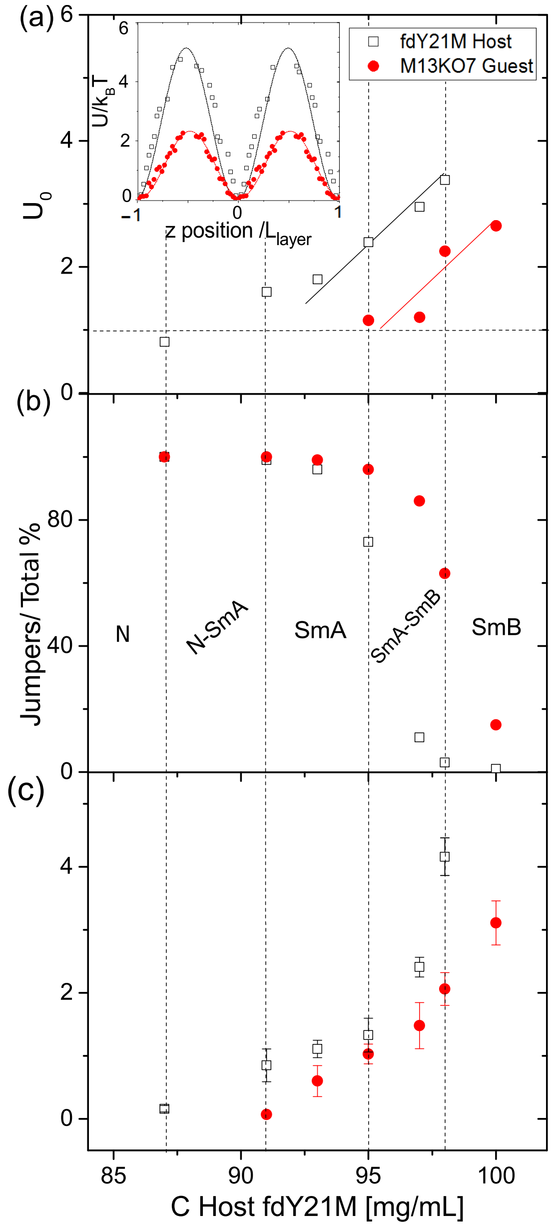

Figure 5.4: *Concentration dependence of a) Smectic potential barriers* U^{LG}_{Layer} *are lower than for the short-host* U^{SH}_{Layer}*, deconvoluted for optical smearing. Solid lines represent the slope of the data. The arrow indicates the difference in concentration for the onset of the smectic potential. The inset shows raw data at [98 mg/mL]; b) Ratio of jumpers over no-jumpers; c) Residence time t. The vertical dashed lines represent the phase transitions. The open squares are the data for the fdY21M short-host particles, and the solid circles are the data for the M13KO7 long-guest ones.*

particles diverges around the SmA-SmB transition for the short-host while it further increases throughout that transition for the long-guest, see Fig. 5.4c.

5.4 Study of self-dynamics: the self van Hove function

We now would like to see how the differences between the potential barriers U^{LG}_{Layer} and U^{SH}_{Layer} affect the diffusion of the particles. The data presented in the previous section suggests that the long-guest is not-commensurate within the host Smectic phase, so we expect a significant impact on the dynamics. This can be most clearly judged from the Self-Van Hove function. This function gives the probability density function for a displacement z during a time t.

$$G(z,t) = \frac{1}{N}\sum_{i=1}^{N} \delta[z + z_i(0) - z_i(t)] \tag{5.2}$$

Eq. 5.2 provides valuable information about the dynamics of particles as it represents the solution at the single particle level for the diffusion permeation equation [1] through the layers. For Brownian particles, the Self-Van Hove function is given by a Gaussian distribution which smears over time.

In the scenario of a smectic background potential, it exhibits distinct peaks at integral multiples of the layer spacing [27, 29]. In Fig 5.5 we plot a comparison of the parallel self-van Hove function between the host and the guest particles at three concentrations in the Smectic-A phase. For the host particle indeed we observe distinct peaks for the lowest concentration of $[91\ mg/ml]$. The long-guest particles display weak humps, so the long-guests do "feel" the potential even though they are not-commensurate. However, the peaks are much less distinct. This shows that the self-van Hove function is the most sensitive measurement to observe the effect of a background potential. For the middle concentration of $[93\ mg/ml]$, peaks are more distinct, but by far not as defined as for short-host particles. Finally, for the last concentration

---

[1] The permeation through the Smectic is also a consequence of the vacancies available in adjacent layers. In 2013, Grelet and Lettinga [28] proposed a phenomenological expression for the permeation, derived by coupling the displacement of a segment of a smectic layer u to the compressibility modulus $\tilde{B}$ via the permeation parameter λ_b. As they explain, the fundamental solution of this diffusion equation at single-particle level is the self-van Hove function (Eq.5.2)

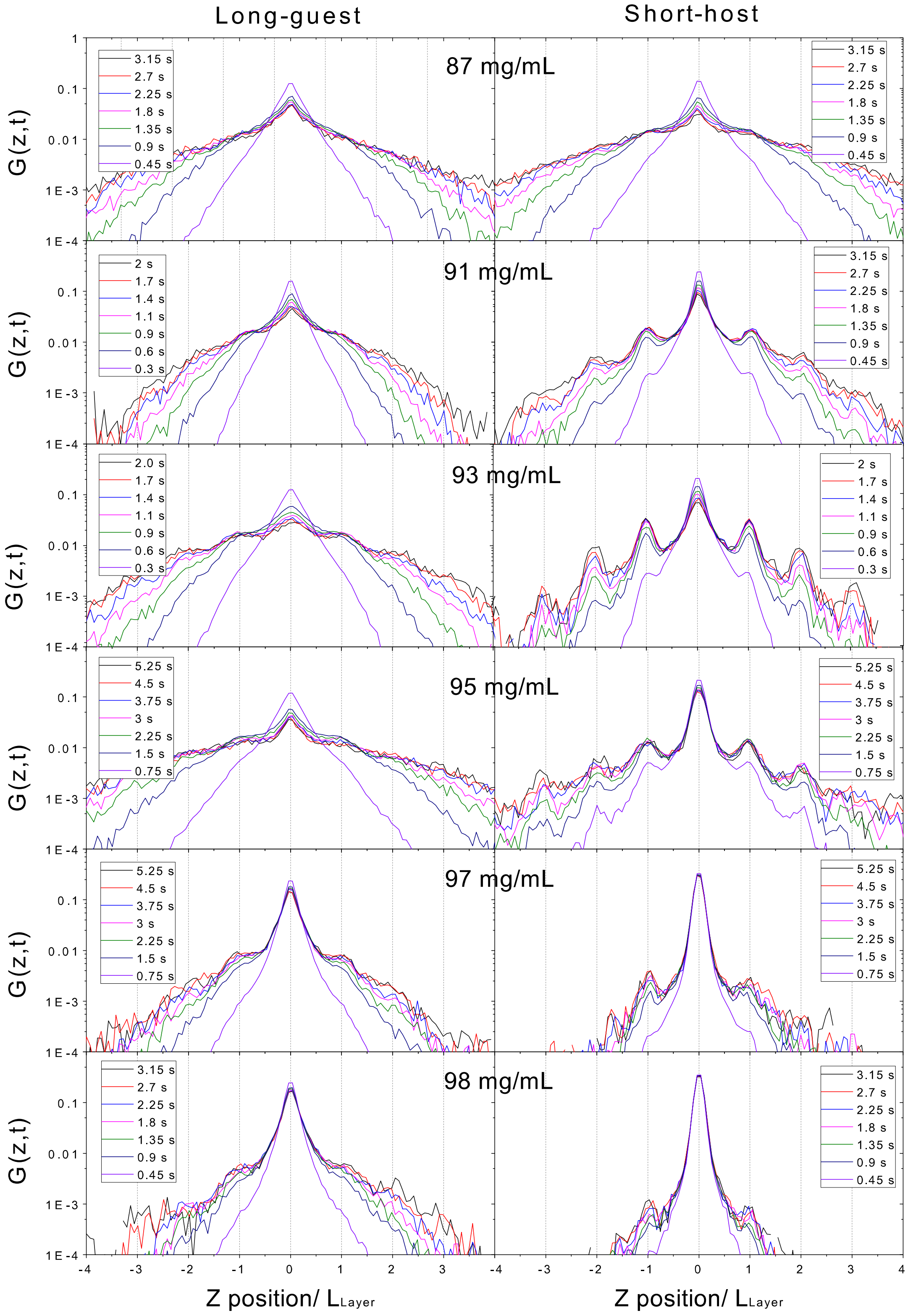

Figure 5.5: *Self-Van Hove function or probability density functions in space at different concentrations for guest (left) and the host (right) particles at different concentrations for the parallel diffusion. The functions are normalized to one and the position is normalized by the thickness of the smectic layer* λ*. Vertical lines indicate the position of the adjacent layers with to respect* z_0.

of [97 mg/ml] the self-van Hove of the short-host is almost frozen, while a smearing is still observed for the long-guest.

These observations hint to an enhanced diffusion in the direction parallel to the rod along the normal of the layers. This will be further exploited in the next section where we discuss the mean square displacement.

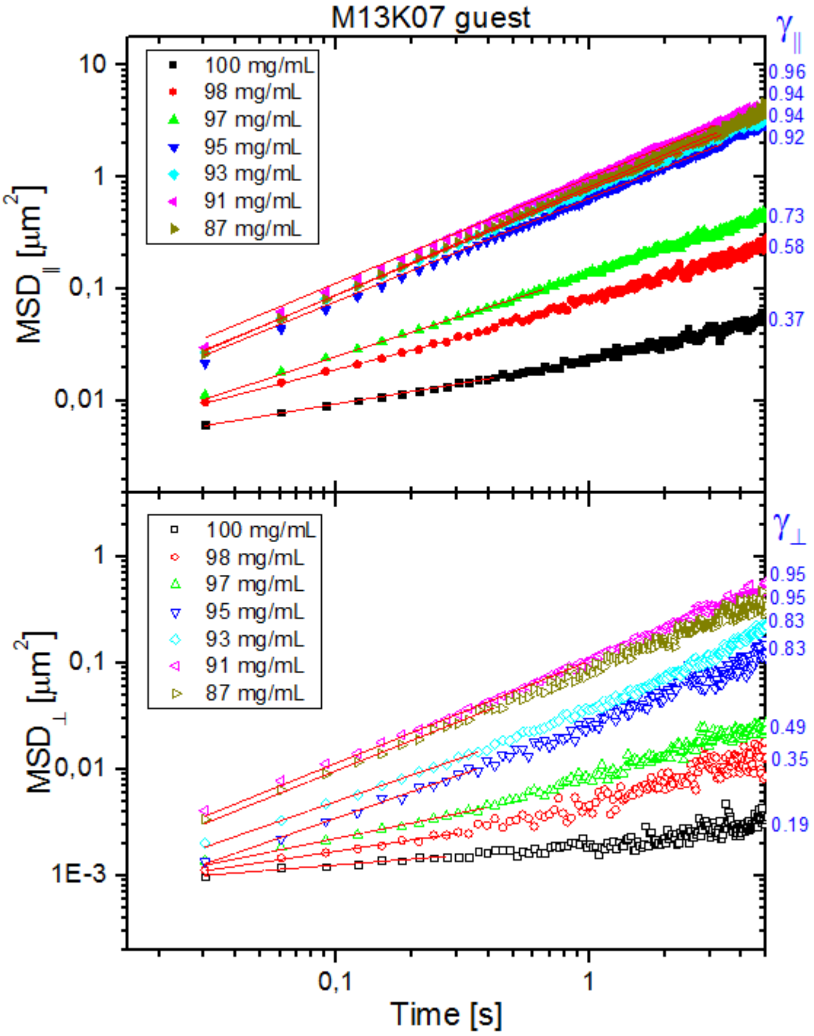

Figure 5.6: *Log-log representation of the mean square displacement (MSD) parallel (top) and perpendicular (bottom) to the director plotted as a function of time for the long guest M13K07 particles in the range of high host concentrations. In blue is indicated the diffusion exponent* γ *obtained from the numerical fit (red lines) according to Eq.5.3*

5.5 Study of self-dynamics: mean square displacement

5.5.1 Dynamics of the full trace

We have now established that the long-guest particles do feel the ordering potential of the smectic phase but to a much smaller extent. Also, the self-van Hove functions hint to a faster diffusion. The potentials and the self-van Hove function are the basis to understand the physics of the most common transport property, namely the *mean-squared displacement* (MSD). In complex systems, the time evolution of the MSD can most generally be described by a power law:

$$\langle r_i^2(t)\rangle = 2D_i t^{\gamma_i}, \tag{5.3}$$

where γ_i is the diffusion exponent, D_i the diffusion rate and i represents the direction with respect to the director (*Par* and *Per* for Parallel and Perpendicular respectively). Diffusion coefficient D_i depends on t^{γ}. When the exponent $\gamma > 1$, it is called superdiffusion, while for $\gamma < 1$ it is sub-diffusive. Both are considered anomalous diffusion. The mean square displacement is calculated from the particle trajectories. In Figure 5.6 we have represented in log-log scale the MSD for the Smectic concentration range, with their respective diffusion exponents for long-guest M13KO7 particles. Diffusion coefficients and diffusion exponent have been obtained from a fit of the data in the linear representation with Eq. 5.3. Only for very high concentrations and for perpendicular diffusion we observe an upturn of the curve in the log-log representation.

There are a few clear distinctions between the diffusion of the short-host and long-guest particles. The long-guest particles exhibit slightly lower $D_{\parallel}$ than short-host particles throughout the Nematic range, while $D_{\perp}$ is much lower and therefore more hindered, as shown in Fig 5.7. On the contrary, after the N-Sm transition $D_{\parallel}$ for the short-host sharply decreases, while for the long-guest $D_{\parallel}$ even seems to increase. The perpendicular diffusion $D_{\perp}$ for both rods is similar in the smectic phase. The anisotropy in the diffusion is directly reflected in the ratio between $D_{\parallel}/D_{\perp}$ which is plotted in Figure 5.7c. While this ratio is already higher in the nematic phase, due to the more restricted perpendicular diffusion of the long-guest, it shows a

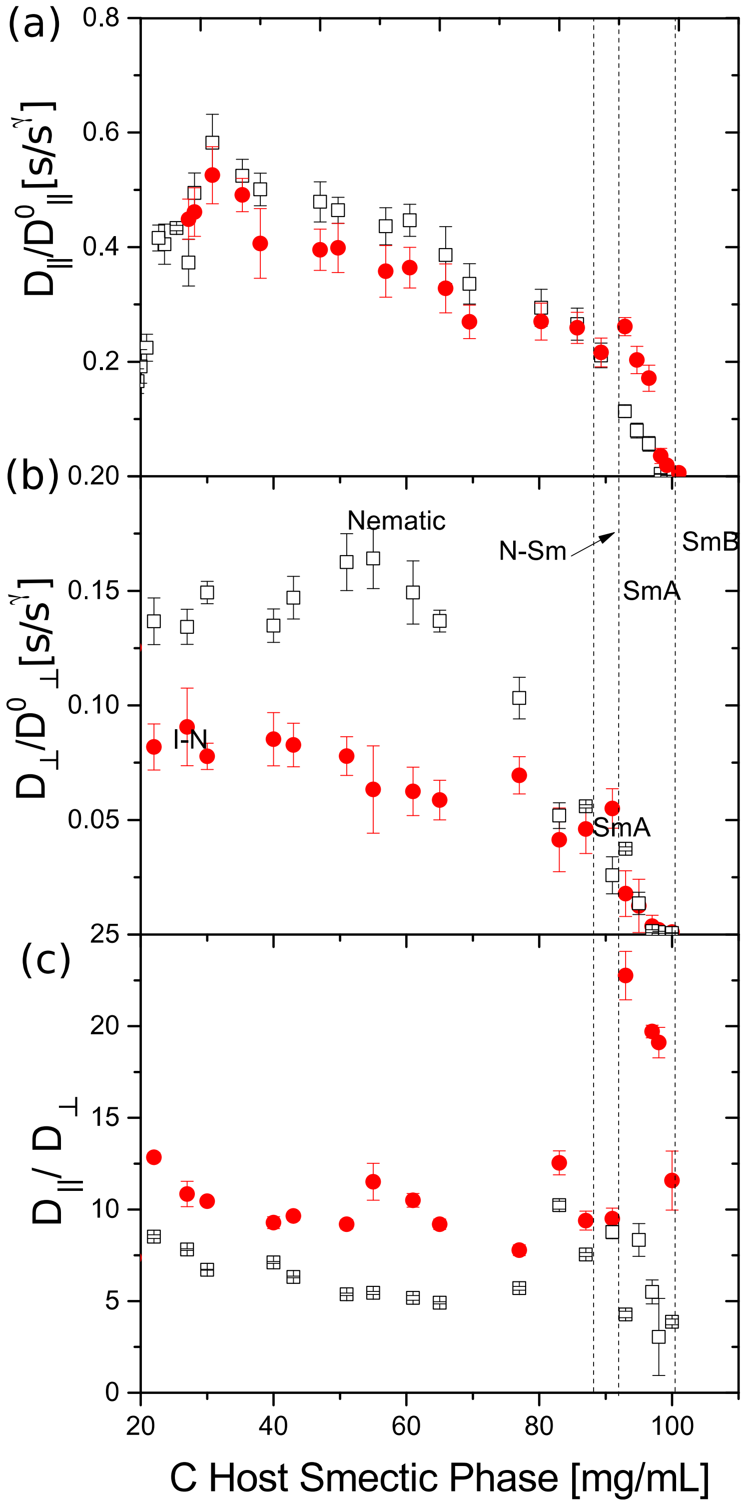

Figure 5.7: *Diffusion rates calculated from the slope of the Mean Square Displacement normalized by the diffusion coefficients at infinite dilution* $D^0[\mu m^2/s]$ *a)* $D_{\parallel}$ *b)* $D_{\perp}$ *as a function of concentration for short-host (open black squares) and long-guest (solid red circles) c) The ratio* $D_{\parallel}$ / $D_{\perp}$ *as function of concentration for host fdY21M (black open squares) and guest M13KO7 (red solid circles). The dashed lines indicate the concentrations at which the phase transitions occur.*

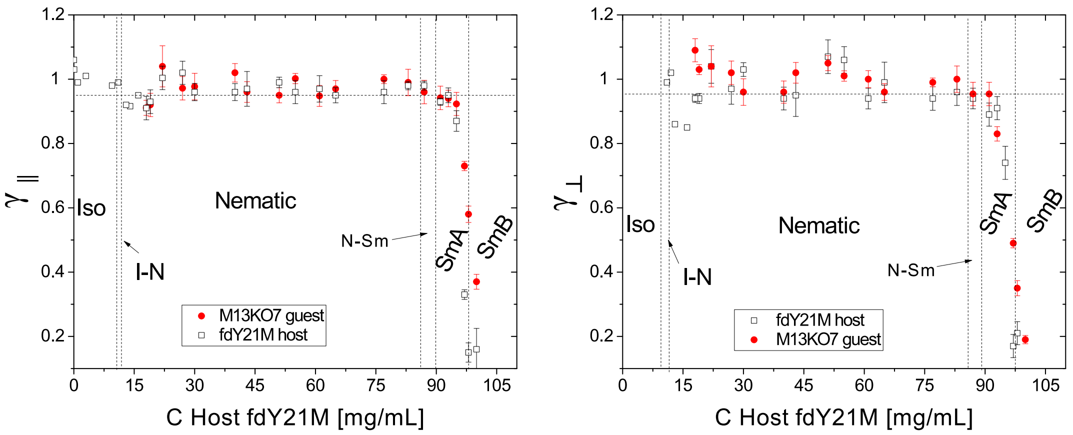

Figure 5.8: *The $\gamma_{||}$ (left graph) and $\gamma_{\perp}$(right graph) obtained from the mean square displacement ($MSD = 2Dt^{\gamma}$), as a function of concentration for host fdY21M (black open squares) and guest M13KO7 (red solid circles). The horizontal dashed line indicates the value at which the particle has diffusive rate, for $\gamma = 1$. Values for $\gamma < 1$ are sub-diffusive and $\gamma > 1$ superdiffusive. The vertical dashed lines indicate the phase transition boundaries.*

strong increase for the long-guest when entering the smectic phase, while the increase for the short-host is far more restricted. $D_{||}$ and $D_{\perp}$ values have been normalized by the corresponding theoretical values at infinite dilution, using $D^0_{||} = \frac{k_B T}{\gamma_{||}}$ and $D^0_{\perp} = \frac{k_B T}{\gamma_{\perp}}$, where $T = 278K$,k_B is the Boltzmann's constant and γ is the friction constant. For M13KO7 particles the theoretical values are M13KO7: $D^0_{||} = 1.89\ \mu m^2/s$, $D^0_{\perp} = 0.95 \mu m^2/s$, and for fdY21M $D^0_{||} = 2.32 \mu m^2/s$, $D^0_{\perp} = 1.16 \mu m^2/s$.

The trends are the same for the diffusion exponent for the parallel diffusion $\gamma_{||}$. The short-host becomes sub-diffusive at a lower concentration than the long-guest, which is a feature that is also reflected in the potentials plotted in Fig. 5.4. $\gamma_{\perp}$ is less sensitive to the differences. It is interesting to remark that at high concentrations (100, 98 and 97 mg/mL) we observe a change in the slope of the log-log MSD in both directions. There is an increase in the slopes, and thus a decrease in γ, which implies that the confined particles escape from a cage.

The fact that no significant difference is observed between semi-flexible long guests and stiff short hosts in the perpendicular diffusion is rather unexpected. Indeed, it has been shown that self-diffusion within the layers is far more pronounced for stiff rods as compared to more flexible ones of the same size [29]. The reason is that parallel, and perpendicular diffusion is correlated, and that M13K07 guests do feel a weaker ordering potential than the constitut-

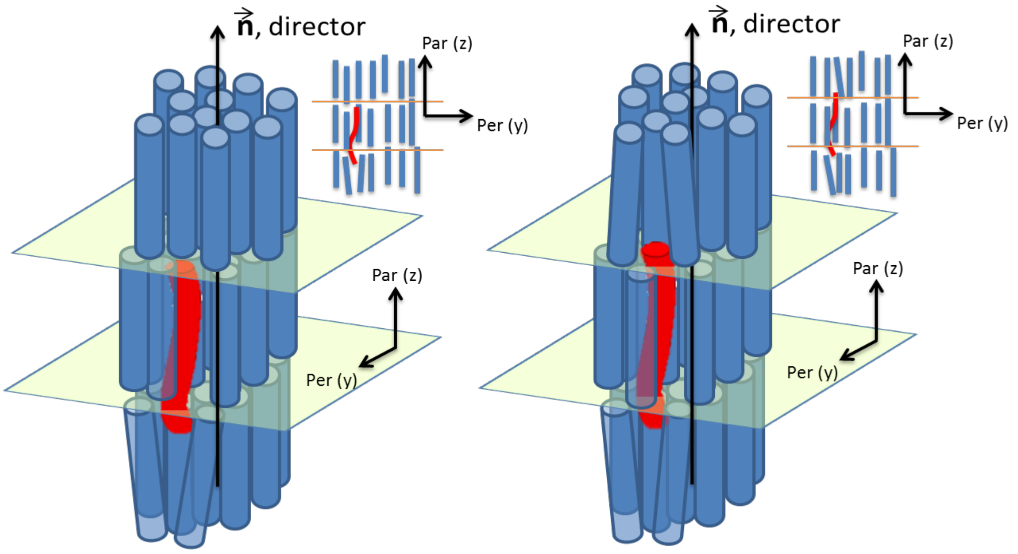

Figure 5.9: *Representation of the different location for the guest particle M13KO7 in the smectic background of fdY21M. In the first conformation, guest M13KO7 (red) is only in contact with two of the layers, when in the image of the right it is located within three layers.*

ing host particles, accounting then for their relative promoted lateral diffusion. This is also reflected by the diffusion exponents showing a less enhanced sub diffusivity than the host particles at the same concentration (Fig.5.8).

5.6 Discussion and Conclusion

The proposition that the diffusion rate of Brownian particles decreases with increasing particles size is not generally true. We proved this effect by evidencing a promoted permeation of non-commensurate long guest rods through self-assembled smectic layers of shorter host particles. We show in this chapter that big Brownian particles can diffuse faster than small particles, when the length scale of a background potential fits the small particles, but not the bigger particles: the long-guest M13KO7 diffuses faster through smectic layers of short-host fdY21M than the host particles themselves, as can be seen in Fig.5.7a, Fig.5.4b and c. The long-guest particles are even mobile in the crystalline Smectic B phase. Thus, we can conclude that permeation is favored for non-commensurate particles. Indeed, also the potential barriers that are effectively felt by the long-guests, U^{LG}_{Layer} are lower than for the short-host U^{SH}_{Layer}, see Fig.5.4a. This does not mean, however, that there is no potential. Even at the lowest concentration in the smectic, the discrete peaks in the self-van Hove function confirm that a mean potential is felt by the long-guest particles, see Fig.5.5. It suggests that the long-guests "feel" the Smectic ordering potential even though they are not-commensurate within the Smectic-layer.

In order to interpret the enhanced permeation of the long particles, it is important to realize that a potential barrier in the SmA is not a static value but rather the result of fluctuations in the density within the layer. Particles can jump in between layers only when there is a void. With increasing concentration, the number of voids decreases and hence the barrier increases. Non-commensurate particles will always be present at least in two layers at the same time so that it does not need to "wait" until a void is created, hence $U^{LG}_{Layer} < U^{SH}_{Layer}$. In the smectic B, which has a crystalline order in the layer, the long-guest particle has to create a void to be accommodated. Hence it is not surprising that it will still be able to diffuse, while the short-host are fixed to their crystal lattice. This process is indicated in the cartoon of Fig.5.9. We assume that there is a coupling of the parallel and perpendicular motion of the guest particle so that the perpendicular diffusion is promoted when the particle diffuses through the smectic layers of the host system.

A particle can, therefore, jump when a transient void exists in the adjacent layer. At higher concentrations, the number of voids decreases and hence the potential barrier increases. As non-commensurate long rods are always present in at least two layers at the same time, they generate their voids facilitating their permeation.

For this process, the flexibility of the long-guest will certainly enhance the diffusion. This is in agreement with results obtained for the columnar phase, where semi-flexible fdwt exhibit higher number of half-jump events than for stiff fdY21M [96].

6

Induced super-diffusion in defected regions of dense Smectic phase

Anomalous diffusion is observed in confined systems and geometries, such as the glass transition or crowded systems. Here, we study the diffusion of long guest tracer particles observed in highly defected regions of a host Smectic phase of filamentous bacteriophages. The defects appeared when two smectic domains with different orientation meet in a grain boundary. These defects are called extrinsic defects since they appear to compensate the deformation. Direct visualization of the guest traces has been performed by fluorescence microscopy, and the grain boundaries regions have been recognized by DIC. The guest particles exhibit two types of behaviors: pure nematic like behavior within a grain boundary and particles that diffuse from the Smectic phase into a grain boundary, displaying a mixed Smectic-Nematic behavior. For these last particles, we find an induced super-diffusion as a result of a driven motion due to confinement, and lateral diffusion is highly restricted. With time, phase separation of the guest particles is observed, preferably located within grain boundaries.

6.1 Introduction

Transport properties in Soft Matter depend sensitively on microstructure. Hence, the structure of the host phase in which a Brownian particle is embedded dramatically influences the dynamics of the particles within the system. This is often observed in biology, where for example, anomalous diffusion in living cells or bacteria predominates due to crowding. The best-known effect is the sub-diffusion of a tracer which is hindered by the crowded system [126,127]. However, there are also examples of particles within a biological system which exhibit super-diffusion due to self-propulsion [141, 142]. Moreover, external forces can bring colloids out of equilibrium in a controlled way, such as shear flow, electric or magnetic fields, and confinement. We generally find confinement scenarios in crowded systems. The structure of these confined systems can be altered by the introduction of topological defects, as it happens for silica rods [45] or the hexatic columnar phase of fd viruses [64]. It has been studied that super-diffusion emerges in confined, crowded systems mainly for geometrical reasons [143–145]. In colloidal crystals, rapid diffusion in dislocations is observed, giving a dynamical heterogeneity, and a random walk in 1D is promoted [146, 147].

Inspired by the example of the colloidal crystals, one could ask about the dynamics of a particle within a dislocation in a Smectic liquid crystal. A considerable amount of investigations has been focused on the nature of the defects of the liquid crystals, concretely in the Smectic phase [148–150]. However very few investigations on single-particle dynamics within the Smectic defects [151, 152] are known, where Brownian diffusion through defects is studied. In these studies, they observe a spontaneous diffusion caused by the appearance of grain boundaries that affect the continuity of the Smectic layers.

The two principal line defects or dislocations in the Smectic are the edge and screw dislocations, as shown in Fig 6.2. Both of them can be defined as a local breaking of the translational order which involves a local variation of the layer symmetry, studied by F.C Frank in 1958 [153]. The edge dislocations are characterized by the breaking of continuity of a Smectic layer, where a new layer appears. The screw dislocations impose a change of orientation of the Smectic layer through the axial direction of the sample, and the rotation in the lateral packing of the molecules becomes localized at defect sites.

The imposed twist is accommodated in the smectic by taking the form of a series of regularly spaced blocks of smectics with a constant angle of rotation between adjacent blocks.

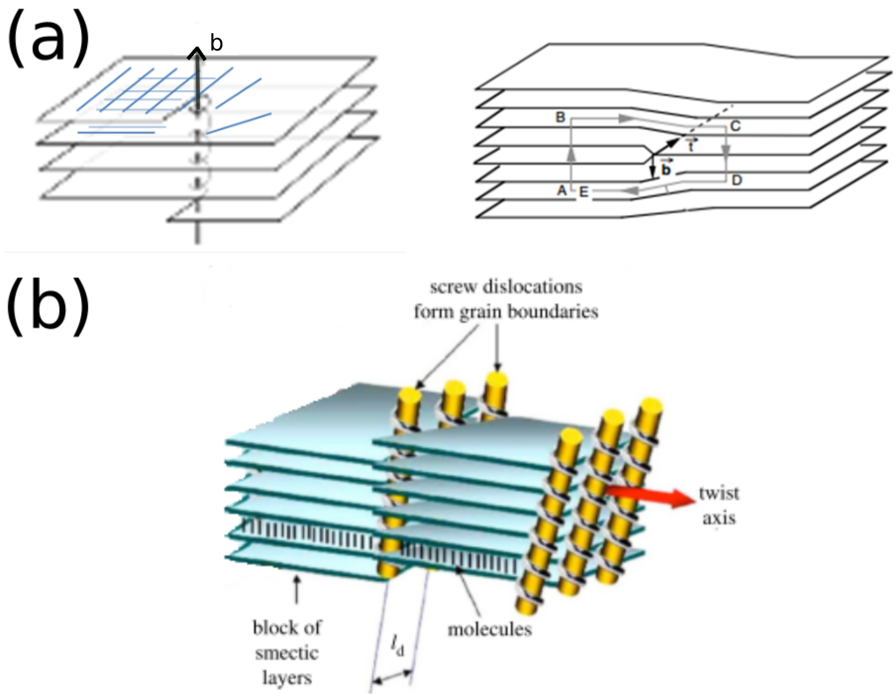

Figure 6.1: *a) Scheme of (left) a screw dislocation and (right) an edge dislocation [154]. The Burger's vector is represented by* ***b*** *b) Scheme of a Twist Grain Boundary (TBG) formed by screw dislocations [155].*

They are defined by the Burger's vector **b**, which represents the magnitude and direction of the distortion. In an edge dislocation, the Burger's vector is perpendicular to the line direction, contrary to the screw dislocations where it is parallel to the line direction.

However, experimentally in the Smectic phases of rod-like colloidal particles we observe *grain boundaries* when there is a disturbance of the packing between two domains, which may consist of various *dislocation* arrangements [155]. The smectic phase resists the twist deformations because it destroys the layering continuity, which is the configuration of lowest energy of the system. Thus, defects must be introduced when such a deformation is imposed. These defects are called extrinsic defects since they appear to compensate the deformation. The defects allow for blocks of defined size of the smectic phase to be rotated about one another through the introduction of rows of screw dislocations that form grain boundaries. One of the optical features due to the TGB is the Moiré pattern, observed by optical microscopy when two Smectic planes with different orientations overlap [154]. However, the distinction of single line defects is not straightforward, since a TGB can be formed by a configuration of a screw and also edge dislocations.

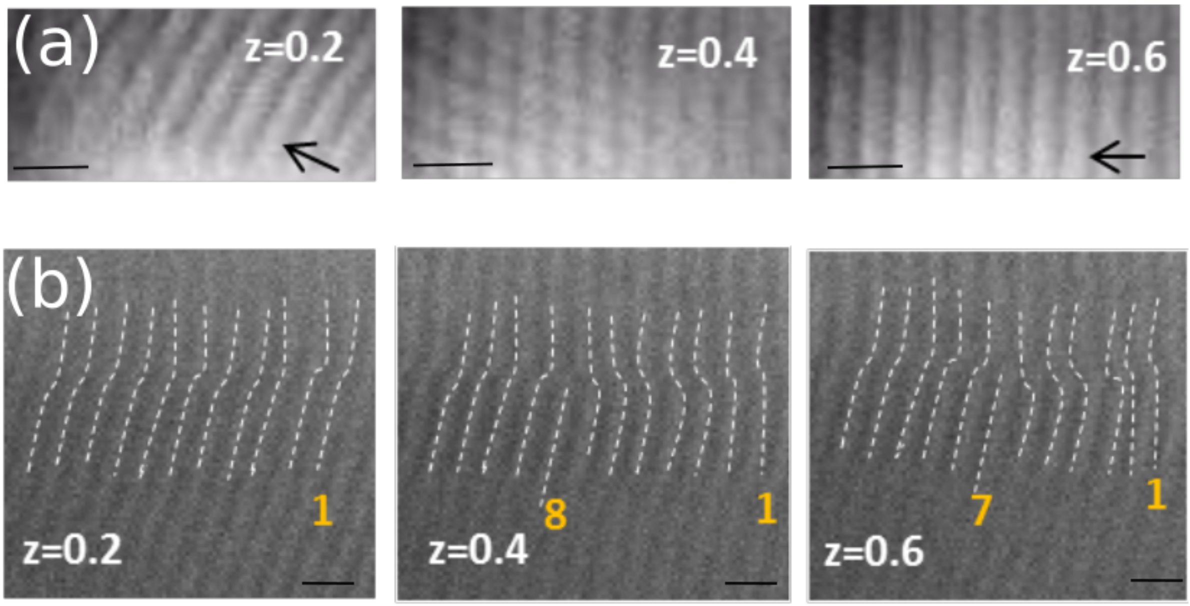

Figure 6.2: *DIC pictures at different z positions through the sample a) picture of the Smectic phase where a Moiré pattern can be observed. The black arrow indicates the director along which the particles are oriented b) edge dislocations where a Smectic layer appears breaking the continuity (dashed white lines). The yellow numbers indicate the position of the layers. The z (μm) indicates the planes normal to the director, at which each picture has been taken. Scale bar indicates* 2 μm

As we have mentioned for colloidal crystals, one might expect that structural defects in the Smectic phase could facilitate the diffusion. In Chapter 4, we have studied a guest-host system, where we observed how the long guest particles locate into defects rather than the host particles. Motivated by these observations, we explore here the role of defects on the dynamics of these guest particles located in the defects of the Smectic host system.

This chapter is organized as follows: in the first section, we present the system and the conditions for the analysis. In the second section, we present the two most important events that take place within and through the defects. We calculate the dynamics, and we compare the results with the already calculated data for the Smectic monodomains (data from Chapter 4). Finally, we suggest an interpretation of the results.

6.2 System: guest-host defected Smectic system

The Smectic phase exhibits two main types of defects: the screw and the edge dislocations, which form the grain boundaries. In the guest-host system presented in Chapter 4, we have observed that the long guest particles (semi-flexible M13KO7, $L = 1.2\ \mu m$), are predominantly located within the defects of the Smectic phase formed by the short host particles (stiff fdY21M, $L = 0.92\ \mu m$). The data were taken at 98 and 100 mg/mL within the Smectic phase of the guest-host system, where highly defected regions are observed.

The conditions of data acquisition are the same as for the guest-host system (see Chapter 4): Fluorescently labelled viruses were visualized using an inverted microscope (IX-71 Olympus), equipped with a high-numerical aperture (NA) oil objective (100x PlanAPO NA 1.4) and a mercury lamp as excitation light source (X-cite series 120 Q). A dual emission image splitter (Optosplit II Andor) was used to project two identical fields of view, corresponding to the two emission wavelengths, onto an ultra-fast electron-multiplying camera (sCMOS Andor camera). The exposure time was 20 ms, while the maximum length of the movies was 15 seconds. After approximately 6-7 seconds photobleaching of the Alexa488 dyes became apparent.

The grain boundaries can be distinguished using DIC microscopy, as shown in Fig6.2. Since the observation is in 2D, we look at single grain boundaries between domains. The corresponding fluorescence images are taken in the same region of interest and overlaid with the DIC picture to locate individual particles within the background structure. The data acquisition was performed one day after sample preparation. For analysis of the dynamics, the trajectories that are identified in a defected region are represented one by one using the Matlab algorithm, as shown in Fig.6.3. At these concentrations, Smectic-like trajectories are expected. However, when a particle is within a defect or diffuses from a Smectic region into a defect, its trajectory exhibits different behavior, as we will demonstrate in the next section. In Figures 6.4 and 6.5 we show more examples of these two types of motion observed in the sample.

It is important to remark that this analysis has been performed by using as reference the overlay of DIC and fluorescence movies, corresponding to each trajectory. The number of particles analyzed was 188 for 98 mg/mL and 175 for 100 mg/mL

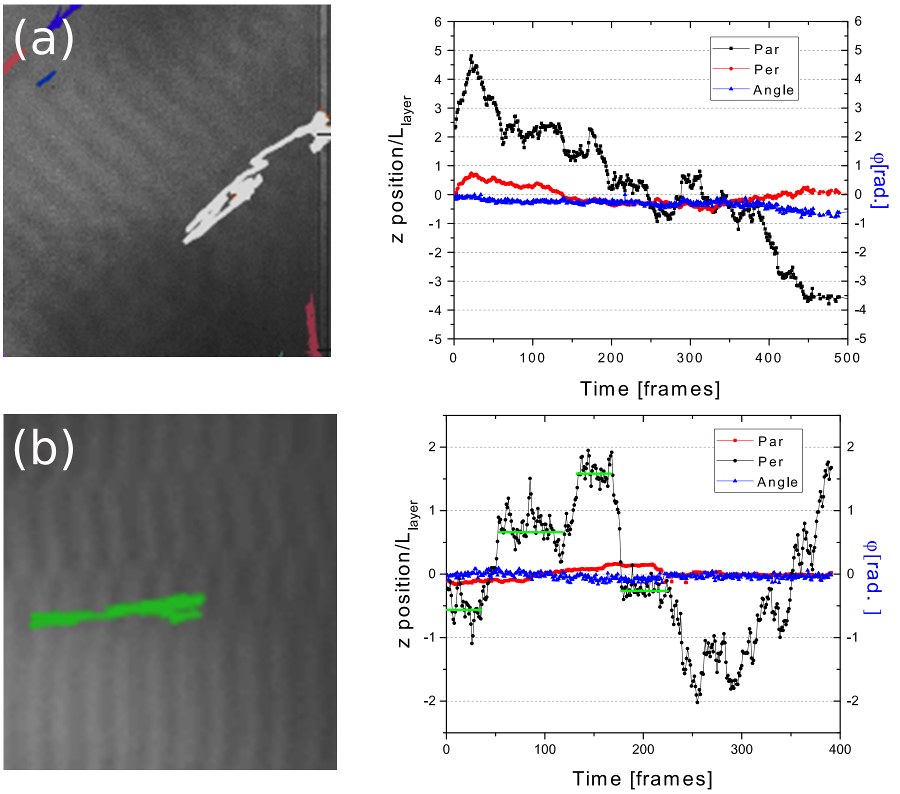

Figure 6.3: *a) Example of a particle that is located within a line defect that exhibits continuous or Nematic-like motion (left) DIC and fluorescence pictures overlay of particles located in a grain boundary (right) parallel and perpendicular position as a function of time b) Examples of a mixed trajectory (left) DIC and fluorescence picture overlay (right) examples of the position as a function of time, where the first part displays jumps and the second part is nematic-like The green lines indicate the time residence* τ_{res} *between two jumps.*

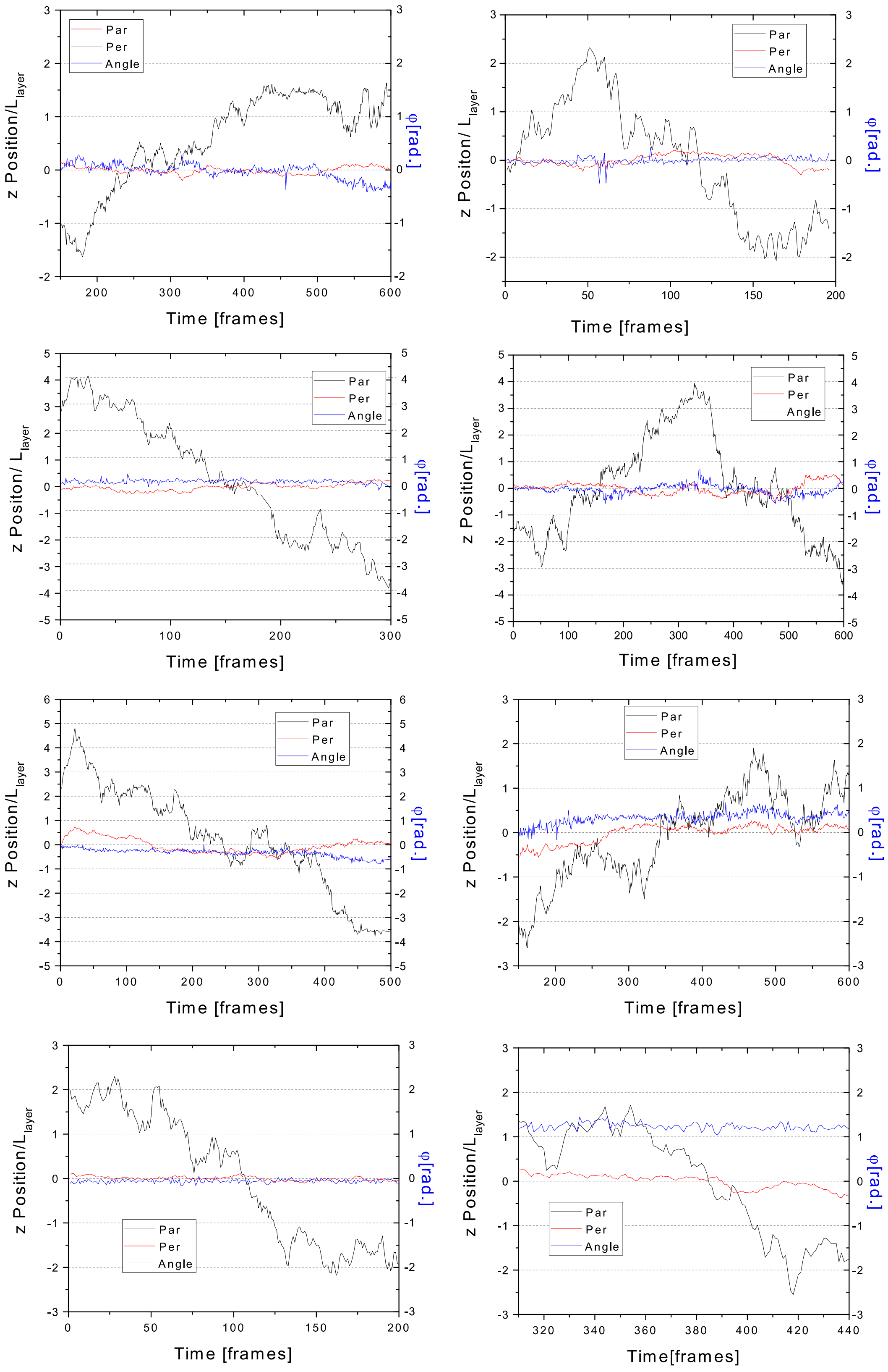

__Figure 6.4:__ Nematic-like trajectories as a function of time (frames) for particles located within defects. The parallel direction is represented by the black line, the perpendicular direction by the red line and the angle by the blue one. The position has been normalized by the layer spacing. Horizontal dashed lines indicate one layer distance.

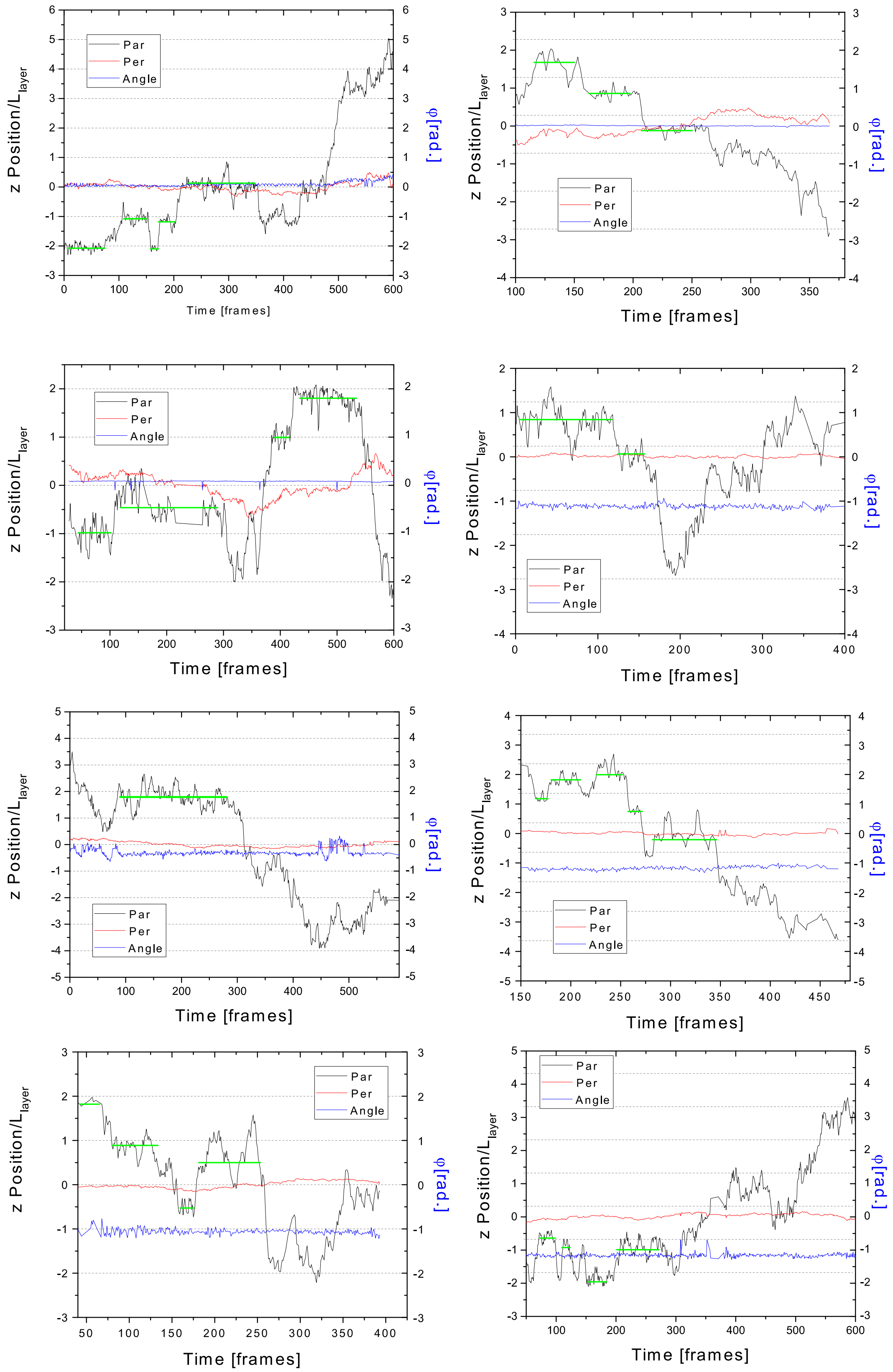

Figure 6.5: Mixed trajectories as a function of time (frames). The parallel direction is represented by the black line, the perpendicular direction by the red line and the angle by the blue line. The position has been normalized by the layer spacing. The green line represents the residence time within a layer between two jump events. Horizontal dashed lines indicate one layer distance.

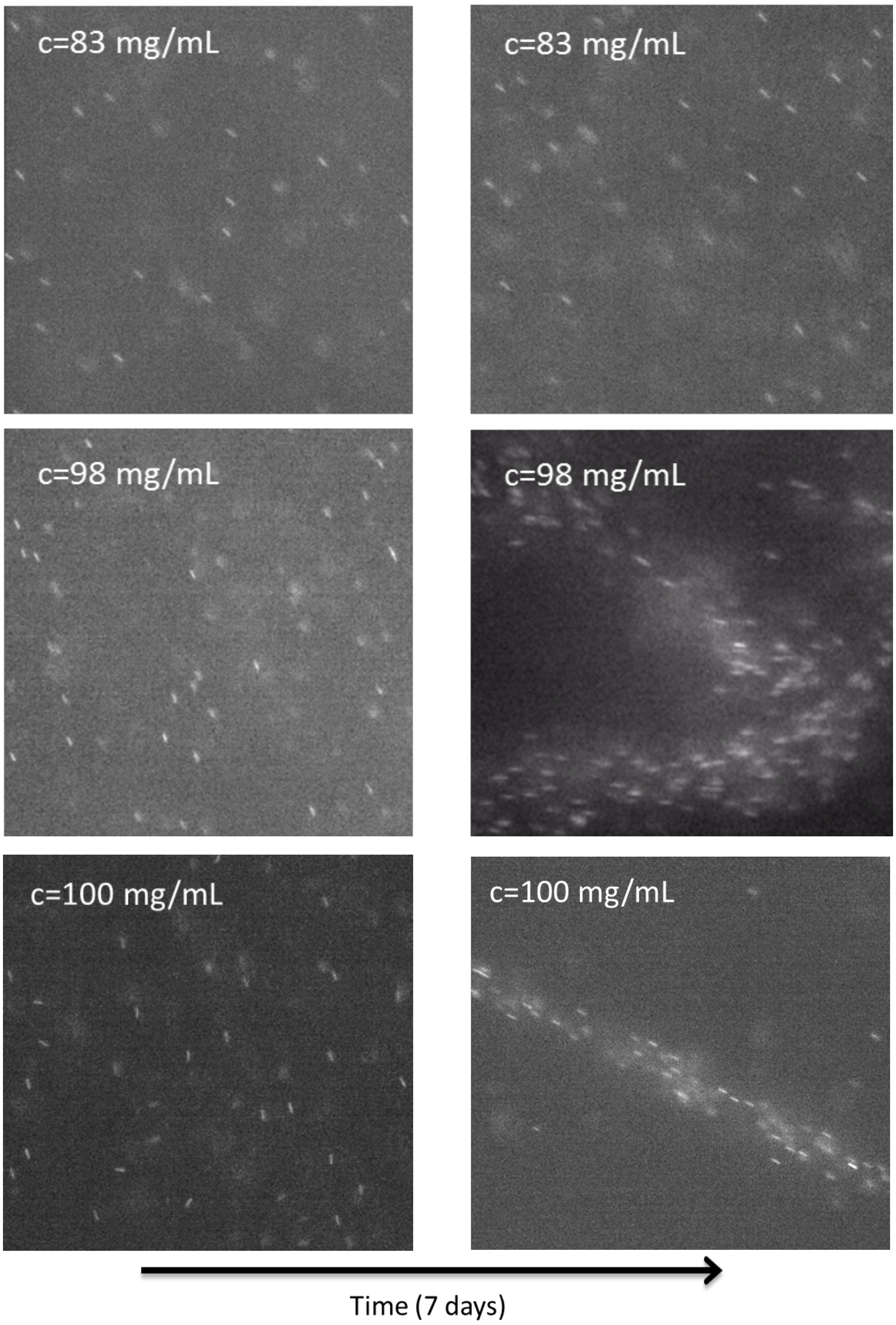

Figure 6.6: *Fluorescence images of guest M13KO7 one day (left) and one week (right) after sample preparation in the Nematic phase at 83 mg/mL (top figures) and in the Smectic phase at 98 mg/mL (middle figures) and 100 mg/mL (bottom figures). The scale bar indicates 2 μm.*

Furthermore, we observe a phase separation of the guest particles with time, within 5 to 7 days after the sample preparation. This phase separation occurs due to the size mismatch of the guest and host particles. This size mismatch is the origin of the faster diffusion of the guest particles, as studied in Chapter 4, but also of the preference of guest particles to be located into defects. After one week, we observe that most of the guest-particles are separated in regions and exhibit motion. However, the dynamics in this state of the sample are not comparable with previous data due to partial drying of the sample. This phase separation has not been observed in the Nematic phase (at 83 mg/mL), as shown in Fig.6.6. This phase separation in the deep Smectic phase may be favored by the location of the guest particles within the defects.

6.3 Measurement of dynamics of particles within grain boundaries

The dynamics of the Smectic phase is influenced by the Smectic potentials, which leads to a jumping-like behavior. At high concentrations in the host Smectic phase, the long guest particles display discrete jump-events, as shown in Chapter 4. A different behavior hints to a change of structure of the sample, as it is the case of the defected regions. We have used two concentrations (98 mg/mL and 100 mg/mL) due to the presence of more defect regions, and because at lower concentrations, the long-guest particles start to exhibit less prominent jumping-like diffusion, which complicates the distinction between the motions within a defect and in a monodomain.

We start the analysis of the results by the distinction between the two main types of events that we observe in the highly defected regions. In Fig6.3 we showed the two characteristic trajectories for the mentioned events: *particles diffusing within a defect* or *particles diffusing into a defect*. We observe particles that are located within a grain boundary and whose trajectories are Nematic-like, contrary to the expected jumping-like behavior within the Smectic domains. Moreover, there are particles whose trajectories are partly smectic-like and nematic-like. We call this behavior *mixed trajectories*, and it has also been observed for a small percentage of host particles (see Chapter 3).

The analysis of these two types of behavior in a defected region has been done separately for the full Nematic-like trajectories and the mixed trajectories. The distinction between Nematic-like and mixed trajectories is possible using the step detection algorithm, which was already used in Chapter 3 for the analysis of Nematic and Smectic behavior in the N-Sm phase transition. We have collected enough events to calculate the average over all events for both types of dynamics in defects. At 98 mg/mL 103 Nematic-like events have been observed, while for 100 mg/mL 96 events. For the mixed trajectories 85 event have been identified at 98 mg/mL and 7 for 100 mg/mL.

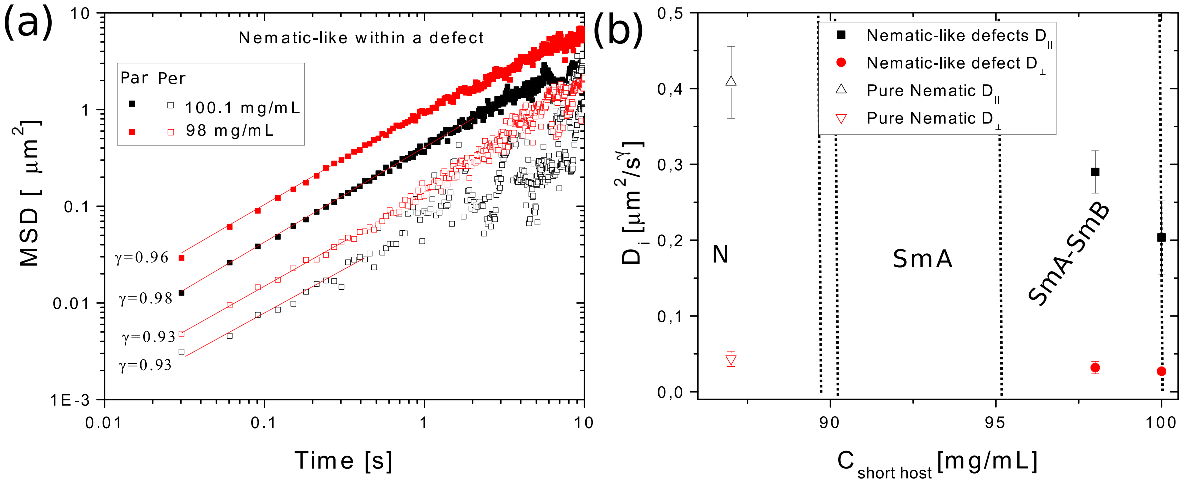

Figure 6.7: *Dynamics for a Nematic-like particle within a defect a) log-log MSD as a function of time for parallel (solid) and perpendicular (open) direction at 100 (black) and 98 mg/mL (red). The red lines correspond to the fit using a power law. The gamma values represent the slope of the MSD b) D_i obtained from the fitting. Solid symbols represent the data of the Nematic-like particles within a defect and the open symbols the data obtained in the previous chapter for the first Nematic concentration after the Smectic phase. The error bar is the standard deviation of the different values obtained from all the movies at a fixed concentration.*

6.3.1 Nematic-like behavior within the defects

We have observed that most of the long-guest particles that are located within a grain boundary, exhibit a continuous motion which is characteristic for the Nematic phase. However, this motion is confined within the defect.

In Fig6.7a we represent the log-log Mean squared displacement for the Nematic-like particles within a defect, from which we have obtained the D_i and the γ by fitting with a power law such as $MSD = 2D_i t^{\gamma}$. The results for D_i as a function of concentration are shown in Fig6.7b. We compare the D_i to the behavior of the first concentration of the Nematic phase after the N-Sm phase transition. For the particles within defects that exhibit Nematic-like behavior, there is no significant difference between 98 and 100 mg/mL. However, the $D_{||}$ in the Nematic like trajectories presents higher values than for the data that has been analyzed in Smectic monodomains (data presented in Chapter 4). On the contrary, the $D_{\perp}$ is of the order of the values in the Smectic monodomains (around 0.01 $\mu m^2/s$), and seems compatible for the values of $D_{\perp}$ in the Nematic phase.

Regarding γ, we observe a distinct diffusive behavior for the Nematic-like particles that diffuse within a defect, and previous results in the Smectic monodomains where it is clearly sub-diffusive. For the nematic-like diffusion within defects, the $\gamma_{||}$ and $\gamma_{\perp}$ are only slightly below 1, which corresponds mainly to a diffusive behavior. Our interpretation for these results is that the nature of the core may be a different phase than the Smectic, forming a channel that induces a Nematic-like diffusion.

6.3.2 Mixed trajectories: motion from a Smectic domain into a defect

We will now turn to the analysis of the particles that exhibit mixed trajectories. This type of particles exhibits a jump-like behavior, related to the location in a smectic monodomain, which suddenly develops into continuous motion in one direction (Fig.6.3b). Thus, we separate both behaviors using the step detection algorithm and analyze them separately.

We represent the log-log MSD's for both parts of the trajectories in Fig.6.8. There is a significant change in the dynamics between both parts of the trajectory by looking at the MSD. The first significant difference is the diffusion exponent γ. The γ of the Nematic-like part of the mixed trajectories exhibits a different behavior from the Smectic part and also from the Nematic-like trajectories studied in Sec.6.3.1.

First, the $\gamma_{||}$ changes from diffusive to slightly super-diffusive behavior, as shown in the change of slope of the MSD in Fig.6.8a. At given time t, the particles experience a velocity $\mathbf{v}$ when they diffuse into the defect, which is bigger than zero, which causes the super-diffusive behavior. We are able to quantify the velocity, knowing the time t where the slope changes and using $D_{||}$ from the first slope of the MSD before it changes, such as $\frac{D}{\mathbf{v}^2} = t$, and taking the D_i of the first slope where $\gamma \cong 1$. For 98 mg/mL, $D_{||} = 0.208\ \mu^2/s$ and $t = 0.35\ s$ so then, $\mathbf{v} = 0.77\ \mu m/s$. For 100 mg/mL, $D_{||} = 0.06\ \mu^2/s$ and $t = 0.34\ s$, giving $\mathbf{v} = 0.42\ \mu m/s$.

Moreover, the results of the γ for the smectic part of the mixed trajectories are consistent

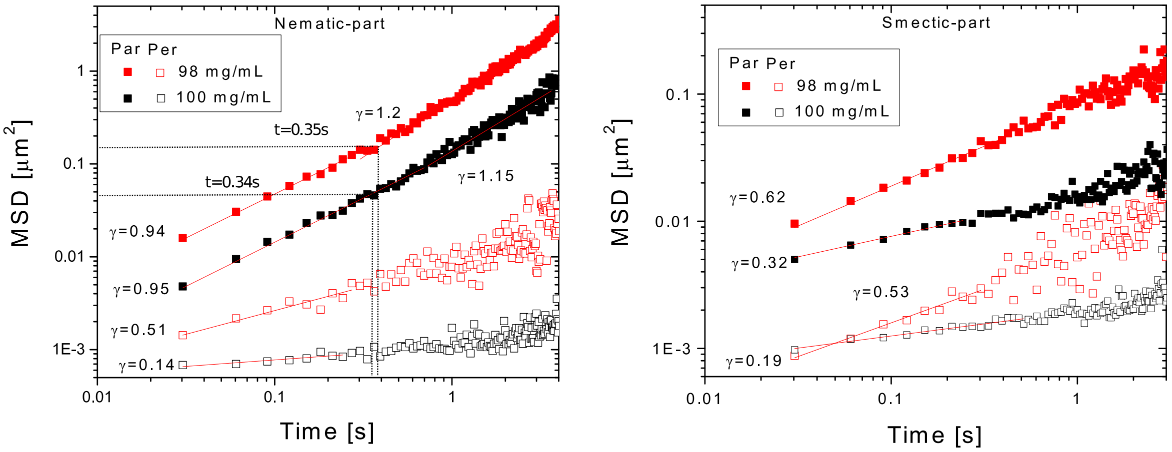

Figure 6.8: *Log-log representation of the MSD of a) Nematic part and b) Smectic part of the mixed trajectories. Solid symbols represent the parallel direction, and the open symbols represent the perpendicular direction. The red lines correspond to the fit using a power law. The gamma values represent the slope of the MSD.*

with the previous results in the Smectic domains for the guest M13KO7, studied in Chapter 4. The particles exhibit a sub-diffusive behavior where the motion is determined by the Smectic potentials of the host system.

Regarding the D_i, there are clear distinctions between both behaviors. The D_i is obtained from the fit with the power law $MSD = 2D_i t^{\gamma}$ of the first slope of the MSD of the Nematic part, where $\gamma \cong 1$. We observe an increase of $D_{\|}$ for the Nematic-part of the mixed trajectory. $D_{\|}$ for the Smectic part is distinctly lower, by about 5 times, and consistent with the values that we got before for Smectic monodomains. The $D_{\perp}$ of the Smectic part is of the order of the Nematic part.

Finally, we compare the results from the Nematic part of the mixed trajectories and the Nematic-like trajectories within the defect. Interestingly, the $\gamma_{\perp}$ for the Nematic-part of the mixed trajectories exhibits a strong sub-diffusive behavior in comparison with the Nematic-like particles within defects and also with the pure Nematic phase. This would hint a strongly restricted diffusion in the perpendicular direction. In Fig.6.9 we compare the D_{rates} of the Nematic trajectories within a defect and the Nematic part of the mixed trajectories. We observe that the $D_{\|}$ is slightly higher for the nematic part of the mixed trajectories. However, the $D_{\perp}$

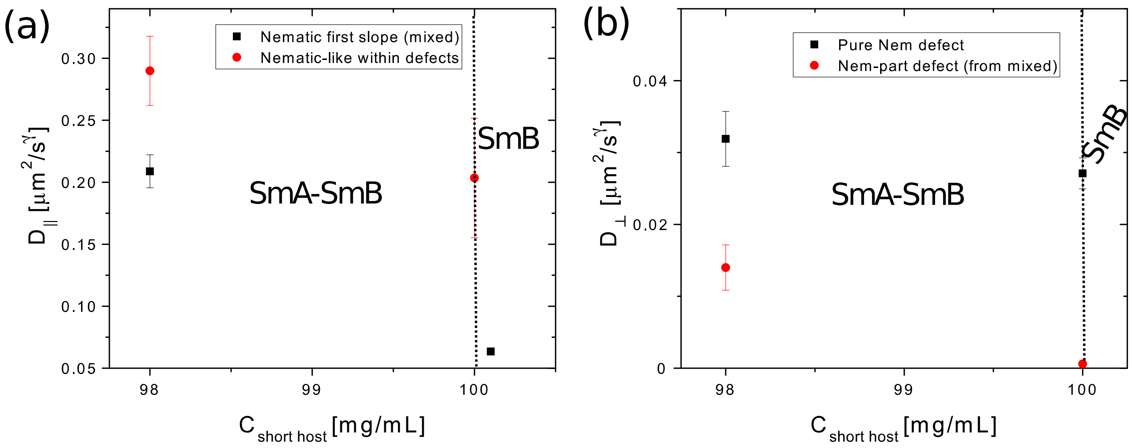

Figure 6.9: *Comparison of a) $D_{||}$ and b) $D_{\perp}$ between pure Nematic particles within defects (black squares) and nematic part of the mixed trajectories. The error bar represents the standard deviation from the values obtained from all particles analyzed at each concentrations.*

for the Nematic part is lower of the mixed trajectories is much lower than for the pure Nematic of particles within a defect.

The previous results correspond to two principal types of behaviors found in the defect regions: the pure nematic-like particles that are located within a defect, and the particles that have partially Smectic and Nematic behaviors, where this mixed behavior is due to the diffusion from a Smectic region into a defect. In the case of the partially Smectic and Nematic particles, they diffuse from a Smectic domain into a defect. This change of domain could explain the slightly super-diffusion behavior, so then it becomes a driven motion with a velocity $\mathbf{v}$, as it is for the ballistic motion when $MSD \sim t^2$.

6.3.3 Re-orientation events

We have observed a third type of event within the highly defected regions, which is the reorientation of the particle during diffusion. However, only a small fraction of the particle reorients (we have tracked 7 events of reorientation), so that the statistics are poor. This type of behavior has been already observed by Naderi *et al.* in the columnar mesophase of fd viruses [96].

In Fig6.10 we show an example of a reorientation event. In this case, the reorientation of

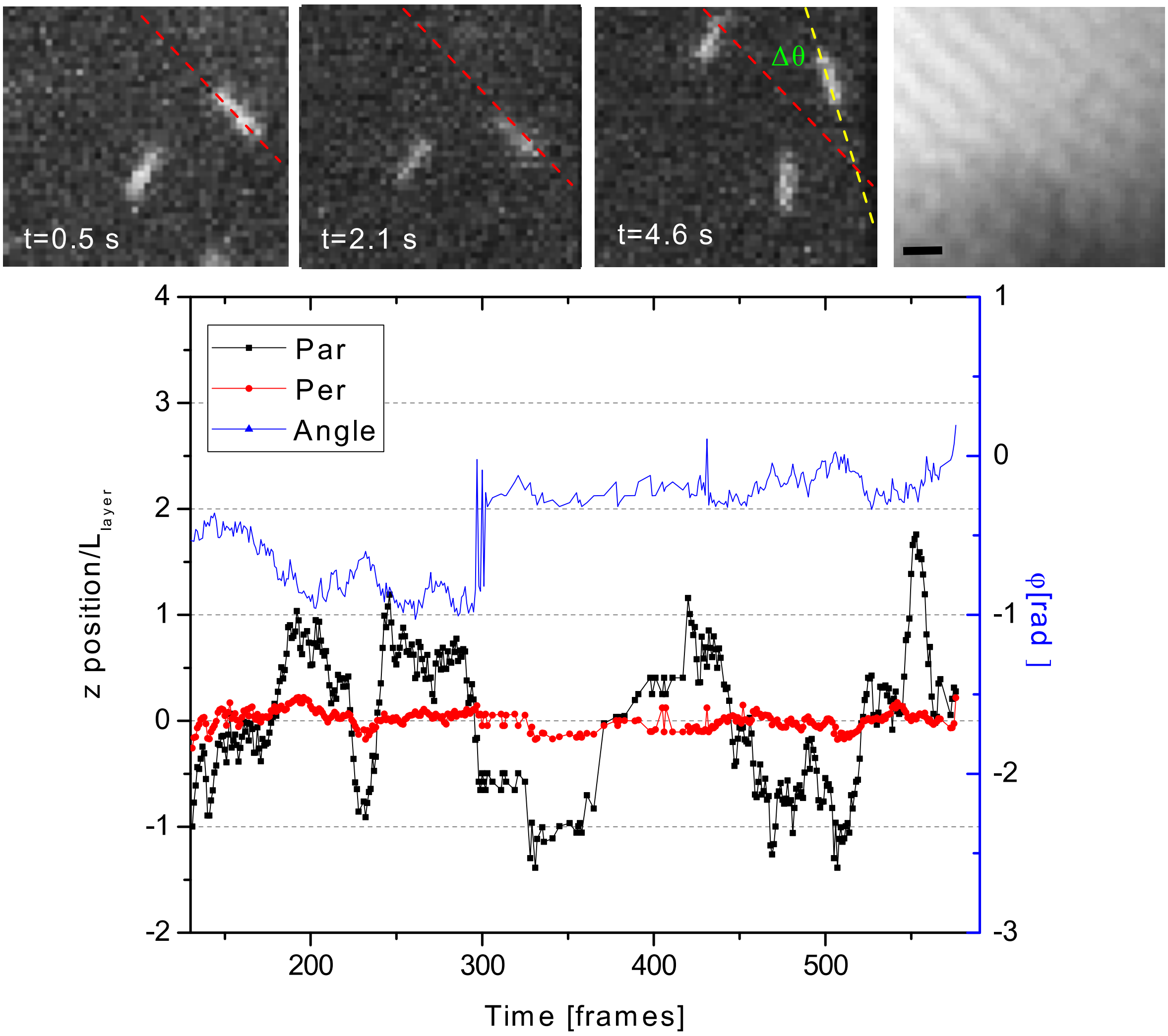

Figure 6.10: *Reorientation event of a long-guest particle within a region where two orientations of the Smectic phase are observed (DIC picture, right). Fluorescence images show the raw data where the dashed red line is drawn perpendicular to the long axis of the labeled particle and indicates its position at the initial time and the yellow dashed line indicates the final position of the particle after the reorientation. $\Delta\theta$ indicates the angle between the initial and the final positions. Scale bar indicates 1 μm*

this particle is related with the possible dislocation (see DIC picture). However, in most of these reorientation events, it is complicated to tell what causes the reorientation due to the resolution of the microscopy techniques.

6.4 Discussion and conclusions

In this chapter, we have studied the diffusion of tracer long-guest rods in a defected smectic liquid crystal formed by shorter host rod particles. The analysis of the dynamics is focused in the defected regions that appear at high concentration in the Smectic phase of the host system. We have quantified diffusion within and into defects of the long-guest particle. We have shown the two types of behavior predominate: particles that exhibit a continuous motion are confined in a line defect of a grain boundary; and particles that escape from the Smectic confinement through or into a line defect, for which the trajectories display both Smectic and Nematic-like behaviors, as we have illustrated in Fig.6.3. The results for the D_i and the γ indeed suggest that for structural and geometrical reasons, the diffusion of the long-guest particle is affected when the particle diffuses within or into a defect due to the absence of smectic ordering.

In the case of the particle within a line defect or a grain boundary, the particle exhibits a Nematic-like diffusion throughout the full acquisition time. Also, this motion is restricted to the defected region. Moreover, compared to the smectic monodomains (data obtained in the previous chapter) the diffusion is higher for particles located within a defect.

The particles that exhibit first a Smectic-like behavior and which escape into defects perform a Nematic-like diffusion which goes from diffusive to slightly super-diffusive behavior. The $D_{\perp}$ and $\gamma_{\perp}$ for these particles are lower than for the Nematic particles within defects, suggesting that the $D_{\perp}$ is restricted due to the structural configuration of the defect. We propose that this super-diffusive behavior could be induced by a driven motion from the Smectic-like region to the defect. Hence, we observe that particles are expelled, causing a super-diffusive behavior, where after a time t a driving force starts to dominate. When a particle experience a velocity, at longer times a ballistic behavior is expected were t^2. However, the particles that go into a defect experience a driven-like motion which should have a t_{final} for this driven regime, due to the confined geometry of the line defect, which finally develops into the pure Nematic-like diffusion studied within the defects.

This behavior could also be compared with the model proposed by Selinger [152], in which interlayer diffusion is enhanced due to the presence of Screw dislocation. However, in this "spiral staircase" effect, we should also observe a change of orientation at the same time that the Nematic-like diffusion occurs as well as the particle going out of focus, which is not the case for most of our particles.

Furthermore, the question about the nature of the core of the defect is presented due to the different type of motion characterized as Nematic-like.

We did recognize a small number of particles that reorient. We suggest that this reorientation from one Smectic region to another with a different orientation is done through a defect. However, it is complicated to relate this kind of event to a specific type of defect due to the poor z-resolution of the DIC technique.

Finally, we suggest that the phase separation observed with time of the long guest particle in the deep Smectic phase of the host may be favored not only by the size mismatch but also the location of the guest particles within the defects.

7

Effect of length and flexibility on the Isotropic diffusion of fd filamentous particles

In the Isotropic semi-dilute regime, the free volume decreases dramatically due to the formation of rod entanglement. Hence, the rotational diffusion is highly restricted. In this chapter, we experimentally explore the effect of length L and persistence length P, on the diffusion of the stiff fdY21M and the flexible M13KO7, from dilute Isotropic to semi-dilute regime. Using single particle tracking, we quantify the self-translational and rotational diffusion. The results for the concentration dependence of the D_{rot} *scales as* $(nL^3)^{-0.3}$ *for fdY21M, and* $(nL^3)^{-0.6}$ *for M13KO7. The* D_{trans} *is promoted at high concentration for long and flexible particles while at low concentrations small particles are faster. Hence, we find that L and P have an opposite effect on* D_{rot} *and* D_{trans}*. Furthermore, by analyzing the self-van Hove function, we determine the diffusivity of the system. We show that flexible particles relax faster to Gaussian diffusion, being the flexibility a mechanism to release the constraint imposed by neighbor particles.*

7.1 Introduction

Slender rod-like particles are common in nature and colloid science. They form entanglement networks where the dynamics exhibits a complex behavior, as it occurs for example in cells [156]. This behavior is present in systems such as F-actin filaments [10], microtubule [157], fd viruses [20] and filamentous polymer [158].

This entanglement of particles occurs mainly in the semi-dilute regime where $L^{-3} < v < d^{-1}L^{-2}$. Within this range of concentration, the motion of a single rod becomes a *reptation* motion, where the particle needs to reorient in order to find the path to diffuse along the long axis. This is called the *tube effect*, first developed by de Gennes [159] and redefined by Doi and Edwards [51, 160]. Doi developed a simple model, where the diffusion of the rods is not hampered when it takes place along the direction of the long axis of the rods, while the rotational motion is reduced due to the confining presence of at least three neighboring rods. The only way that the rods can reorient by 'reptating' out of its cage is by diffusing along the long axis. Doi showed that this diffusion strongly reduces as a function of the concentration, as well as the length of the rod

$$D_r = k_B T \frac{Ln(L/d)}{\eta_s c^2 L^9} \tag{7.1}$$

where c is the concentration, L and d are the lengths and the diameter of the particle respectively, and η is the solvent viscosity. Studies on the rotational and translational diffusion of rods in the semi-dilute and dilute regimes have been performed for rigid rod macromolecules [52], rod-like polymers [161], and also rod-like viruses [57,59]. Recent simulations proved how the decrease of the rotational diffusion is significantly affected by the aspect ratio of rigid fibers [60,162–164]. It is known that the rotational diffusion depends strongly on concentration and the length of the particle, but the role of stiffness on dynamics in the semi-dilute regime remains unclear. Although, as with cooked spaghetti, flexibility would aid to reduce the confinement effect by neighboring rods.

The flexibility of rods stabilizes the isotropic phase, narrows the I-N coexistence region, and causes a decrease of the nematic order parameter at phase coexistence, as Khokhlov-Semenov predicted in their theory [36]. This is indeed observed for rod-like viruses, where the I-N phase transition takes place at smaller volume fractions for stiff fdY21M than for flexible fd-wt [22]. This shift is related to the free volume and how the particle can diffuse within the system.

In this chapter we will study the effect of length L and persistent length P on the self-dynamics of rod-like particles throughout the Isotropic phase: from dilute to semi-dilute regime close to the I-N phase transition. In the first section, we present the experimental system and the range of concentrations used. Then, we show and compare the rotational D_{rot} and translational diffusion D_{trans} coefficients for both particles, and we analyze the self-van Hove function to characterize the nature of the diffusivity at each concentration.

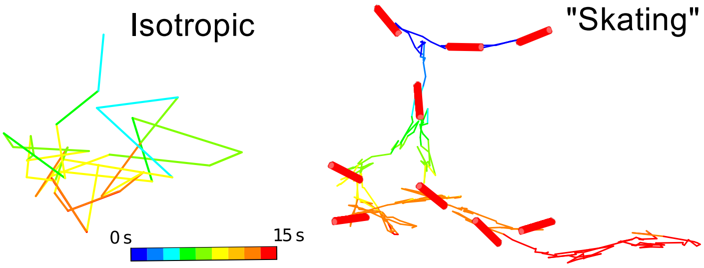

Figure 7.1: *Representation of raw trajectories of a) isotropic diffusion b) reptation or skating diffusion. The red cylinder represents the rod particle at each point where the particle needs to reorient to diffuse. The color scale indicates the evolution of the position in time.*

7.2 The System: semi-dilute isotropic phase of semi-flexible and stiff rod-like viruses

We use as experimental rod-like particles stiff fdY21M with a persistence length of $P = 9.9\ \mu m$ and contour length $L = 0.92\ \mu m$, and semi-flexible M13KO7 with $P = 2.2\ \mu m$ and $L = 1.2\ \mu m$. The M13KO7 viruses were labeled with Dylight549 dye and the fdY21M with Alexa488 dye, according to the protocol presented in Chapter 2. The particles are dispersed in TrisHCl-NaCl buffer at 110 mM Ionic strength and pH=8.2. The labeled viruses were added to a matrix of non-labelled viruses to have a ratio for each system of 1 labeled virus to 10^5 non-labelled viruses. Fluorescent labeled viruses were visualized using an inverted microscope (IX-71 Olympus), equipped with a high-numerical aperture (NA) oil objective (100x PlanAPO NA 1.4) and a mercury lamp as excitation light source (X-cite series 120 Q). The exposure time used was 5 ms, while the maximum length of the movies was 9 seconds, with and frame rate of 50 fps.

The concentrations used cover the full range of the Isotropic phase, starting from the dilute regime where $\nu < L^{-3}$ and semi-dilute regime where $L^{-3} < \nu < d^{-1}L^{-2}$. We characterized two types of trajectories for each regime as shown in Fig.7.1. The Isotropic trajectories are characteristic of the dilute regime where rods can freely rotate and $D^0_{\parallel} = 2D^0_{\perp}$. The skating trajectories are found in the semi-dilute regime, as the particles diffuse throughout the entanglement of neighbor rods. In next section, we present the characteristic dynamics for both types for flexible and stiff particles in these two ranges of concentrations.

7.3 Study of dynamics

One of the significant changes in the Isotropic phase when the concentration increases, is the decay of orientational degrees of freedom of the particles. The rotational diffusion freezes, being compensated by the increase of translational entropy after the phase transition [25, 26, 60]. This is directly reflected in the diffusion coefficients, as shown in previous chapters. In addition to the Mean-square displacement, we calculate the $\bar{P}_2$ parameter. The $\bar{P}_2$ parameter measures the time-dependence between the initial orientation u_0 and the orientation at time t. We need to consider the $< cos(\Theta_t)^2 >$ between the u and u_0, which is 0 when the rod is perpendicular to the initial orientation. Thus, $\bar{P}_2$ should decrease to zero at a different rate depending on the concentration.

The MSD and the $\bar{P}_2$ parameter are represented from the diluted to the semi-dilute regime, where Doi's theory can be applied, as shown in Fig.7.2. We observe a linear behavior of the MSD for all concentrations for fdY21M, while for M13KO7 at concentrations close to the I-N phase transition we observe a change of slope, after approximately 0.5 s. We normalize the MSD by the square of the length of the rods L^2, to obtain the time at which the particles have diffused by half rod length $L/2$, which depends strongly on concentration, as shown in Table 7.1.

The time dependence of the $\bar{P}_2$ parameter is represented for both viruses in Fig.7.2b. It shows an exponential decay that becomes stronger at lower concentrations, where the rods

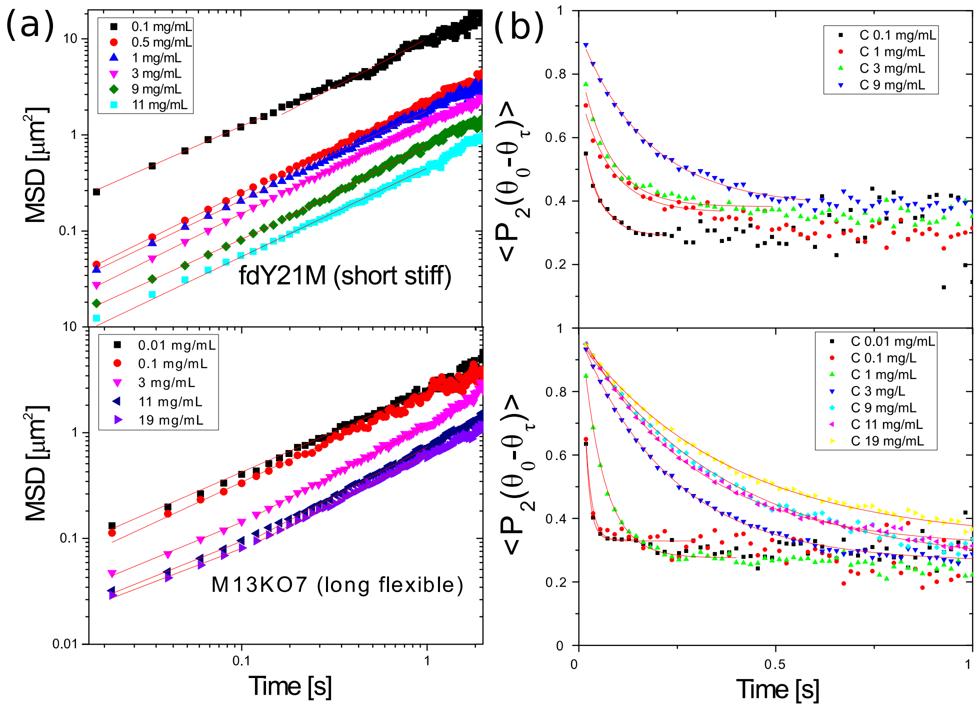

Figure 7.2: *Time dependence at different concentrations of a) Log-log representation of the MSD for the two viruses at different concentrations b) $\bar{P}_2$ parameter. The red line corresponds to the fit up to the time where the particle diffuses by $L/2$.*

Table 7.1: *Times at which the viruses have diffuse by half rod length $L/2$*

	Viruses	
C [mg/mL]	fdY21M	M13KO7
0.1	0.05 s	0.15 s
1	0.3 s	0.3 s
3	0.5 s	0.4 s
9	0.7 s	0.65 s
11	1.2 s	0.7 s

have more rotational freedom. The $\bar{P}_2$ parameter is fitted for each concentration up to the time where the rod has diffused by half rod length $L/2$, using the following equation:

$$\bar{P}_2 = \langle P_2(\Phi_t)\rangle\rangle = y_0 + exp(-2dD^0{}_{r,s}t), \tag{7.2}$$

where $d = 2$ indicates the dimension of the system and D_r is the rotational diffusion coefficient. The rotational and translational diffusion coefficients are shown in Fig.7.3. Rather than decreasing to zero, we observe an offset of the $\bar{P}_2$ parameter of 0.3 ± 0.1. We assume this could be an artifact due to the tracking in a 2D plane, or even a time resolution limitation in our data acquisition.

As expected, the translational diffusion depends on the size of the particle. For stiff fdY21M the diffusion in the isotropic phase is shifted as the phase transition occurs at lower concentrations. Also, it is of the order of D_{trans} for flexible M13KO7 in the semi-dilute regime, and it becomes higher at lower concentrations. For M13KO7, D_{trans} increases gradually and remains lower than fdY21M after 1 mg/mL, as shown in Fig.7.3a. The concentration dependence of the rotational diffusion coefficient is shown in Fig.7.3b. In the diluted regime, D_{rot} is higher for flexible M13KO7 and reaches a constant value of around 17 s^{-1}, then it decreases gradually, being higher than stiff fdY21M, up to the concentrations close to the I-N phase transition where it drops below fdY21M. At higher concentrations in the semi-dilute regime, the rotational diffusion for flexible particles is slightly lower than for stiff fdY21M. However, the results are not in agreement with Doi's prediction, as represented by the slope in Fig.7.3b. The decreasing rate of the D_{rot}/D_{rot}^0 as a function of rod density predicted by Doi's is 2 within the semi-dilute regime, while for the particles used in our experiments, the rates are considerably smaller, being 0.2 and 0.3 for fdY21M and M13KO7, respectively.

Furthermore, we analyze the self-van Hove function using the method of Wouter den Otter as explained in Chapters 1 and 3. This is done throughout all concentrations between the dilute and semi-dilute regime. We are interested in the behavior of the system at concentrations close to the I-N phase transition, where the *tube effect* is observed and also the called *reptation diffusion*. We normalize the self-van Hove function by multiplying the probability by $\sqrt{dt}$ and dividing the position by $dz/(\sqrt{dt})^2$. This normalization takes out the effect of diffusion over time, so the curves are comparable. The fitting is done by use the following expression:

$$Ln(G(z,t)\sqrt{dt}) = a_1(\triangle x^2)^{a_2}; \tag{7.3}$$

where a_2 is 0.5 for Lévy-flight and 1 for Gaussian respectively, and a_1 is related to the inverse of the D_i when $a_2 = 1$. In Fig.7.4 we represented the re-scaled self-van Hove function (as

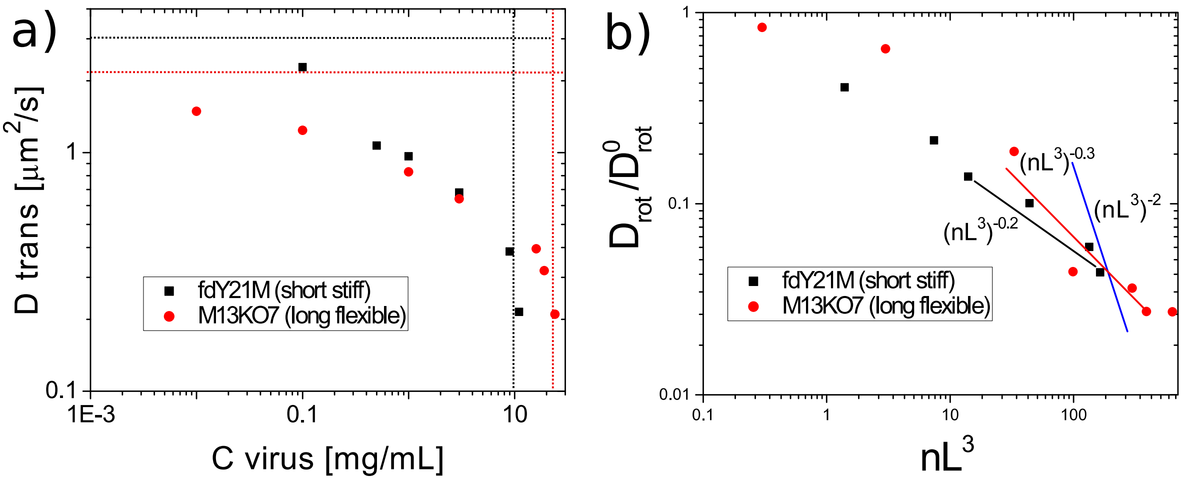

Figure 7.3: *Concentrations dependence of a) D_{trans} calculated from the slope of the MSD fit with a power law $y = ax^b$. The dashed colored lines represent the I-N phase transition for each system b) D_{rot}, calculated from the $< P_2(\Theta_t) >$ parameter function as $exp^{(-2dD^0{}_r t)}$. The blue line indicates the slope obtained from Doi's prediction, and the red and black lines are the slopes obtained from the fitting of the data for M13KO7 and fdY21M, respectively.*

explained in Chapter 1 and Chapter 3), for stiff fdY21M and flexible M13KO7 at different times at a concentration of 3 mg/mL. We clearly see the change of the shape, from exponential (black squared) to linear (blue triangles), as it goes from Levy-flight to Gaussian distribution with time. The fact that the data at 1.4 s is squeezed is due to the rescaling of the self-van Hove function, and shows a transition to a different diffusion rate D_{long}.

The values for the a_1 and a_2 parameters as a function of time for both particles are shown in Fig.7.5. At a low concentration in the Isotropic phase ($0.1 mg/mL$), the a_2 parameter fluctuates around 1, exhibiting Gaussian behavior as expected. As we increase the concentration, we observe a decrease of the a_2 parameter. Initially, at $1 mg/mL$ the a_2 parameter starts at around 0.6 and recovers to 1 for M13KO7 and at around 0.8 for fdY21M. For flexible M13KO7, at 3 and 9 mg/mL, the a_2 parameter relaxes again from values around 0.5 to 0.8-1, while for stiff fdY21M the a_2 parameter remains at lower values and it recovers at longer times to 1. At concentrations close to the I-N phase transition the values for both systems remain between 0.5 and 0.75, being always lower for stiff fdY21M at longer times. The a_1 parameter shows a dependence which is proportional to D_{trans}^{-1} when $a_2 = 1$, as explained in Chapter 1. At long

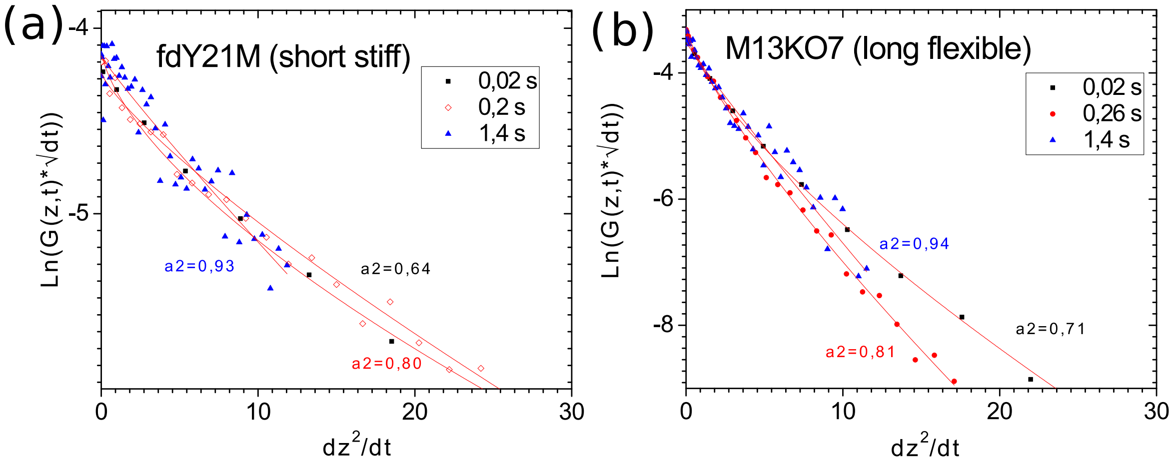

Figure 7.4: *Re-scaled self-van Hove function at 3mg/mL for the two types of rods: short stiff fdY21M (left) and long flexible M13KO7 (right). The effect of time has been suppressed with the scaling. Three times are represented: short time (black squares), medium time (red circles) and long time (blue triangle). The fits are represented by the red lines.*

times, for flexible long particles a_2 is higher than for short flexible particles, meaning that D_{trans} is smaller, being consistent with results shown in Fig.7.3a.

Moreover, the *reptation*, also called *skating diffusion* [24], is observed for both viruses at concentrations close to the I-N phase transition, as showed in Fig.7.1. The back and forward diffusion of the particle is represented in the trajectory in comparison with the trajectories observed in the dilute Isotropic phase. The change of orientation of the rod allows the particle to diffuse in a direction until the rod reorients again.

7.4 Discussion and conclusion

In this chapter, we have explored the effect of flexibility on the self-rotational and translational diffusion at concentrations, where the theory of Doi [51] can be applied. We use two rod-like viruses with different length and with a remarkable difference in persistence length, and we will discuss here the effect of both on dynamics.

We observe from the D_{trans} that short particles exhibit faster diffusion at low concentrations in the Isotropic phase. The D_{trans} coefficients overlap between 1 and 3 mg/mL for both parti-

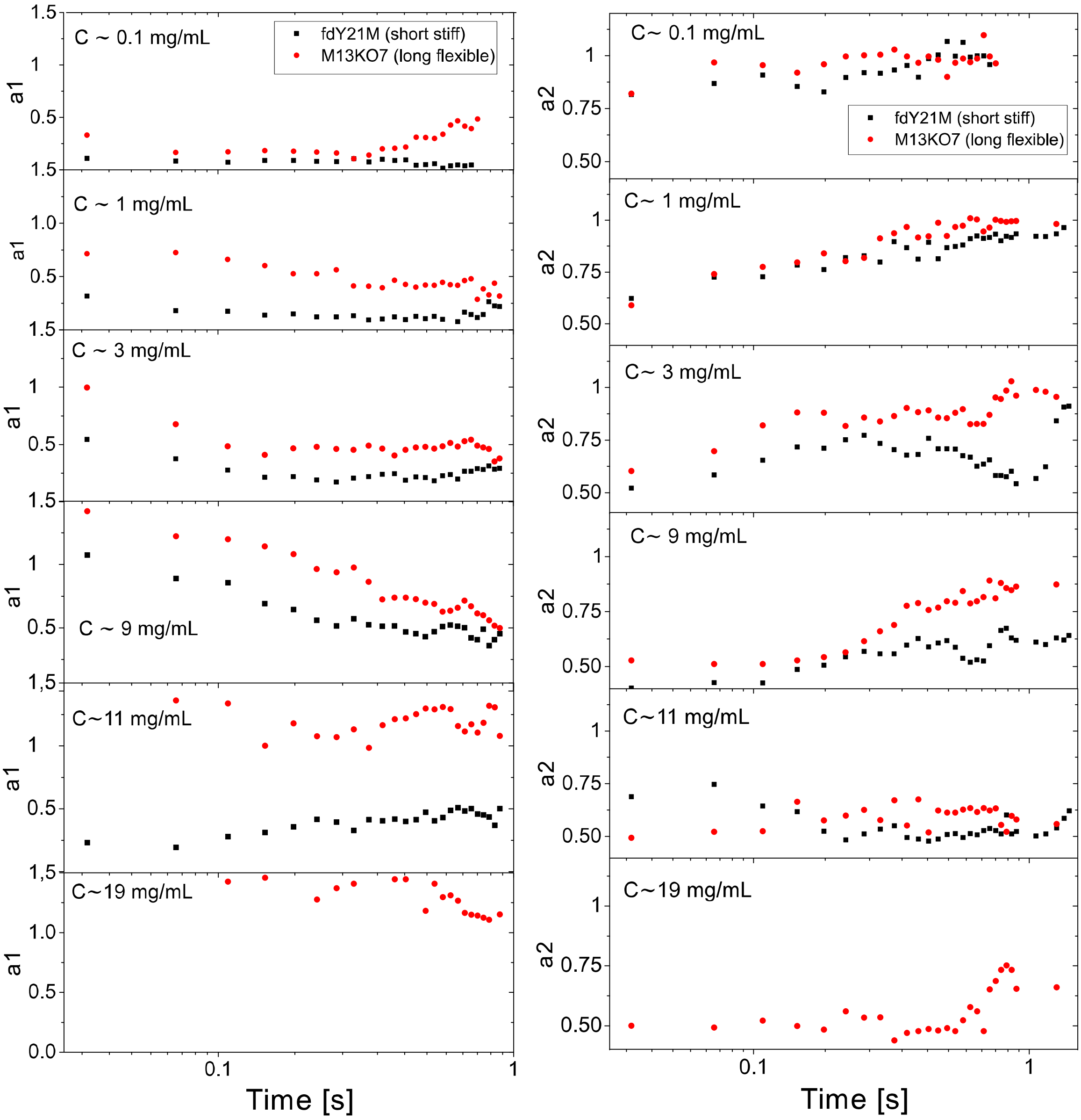

Figure 7.5: *Time dependence for fdY21M (black squares) and M13KO7 (red circles) of (left) the* a_1 *parameter and (right) the* a_2 *parameter both obtained from the fitting of the re-scaled self-van Hove function.*

cles and at 10 mg/mL remains higher for flexible M13KO7. This behavior has been discussed by Russo in his study of the D_{self} for stiff TMV and semi-flexible PBLG. They proposed that the delay in diffusion of PBLG was due to its flexibility as a mechanism to evade the constraints to their motion [59]. In this case, our results are in agreement with the results obtained for TMV.

On the contrary, rotational diffusion is not faster for longer rods at high concentrations in the isotropic phase (close to the phase transition) and increases below the stiff particles at concentrations lower than 10 mg/mL. Hence, flexibility may help to find more often a path to diffuse between the neighbors without reorientation, and also promote the translational diffusion, since D_{rot} for flexible M13KO7 are close to those for stiff fdY21M, as it is shown in Fig.7.3. Also, the time that a particle takes to diffuse $L/2$ is higher for stiff fdY21M, which again confirms that at higher persistence length the mobility in the entanglement of rods is indeed more restricted. These results show that there is an opposite effect of the flexibility on D_{rot} and $Dtrans$. However, although in simulations the results were in agreement with Doi's predictions [60], our results show a deviation in the slope for $Drot/D^0_{rot}$ as a function of concentration. This could be due to the hydrodynamic interaction and the fact that we have a semi-flexible particle in comparison with the stiff rod used in the theoretical model.

Moreover, the a_2 parameter shows that the flexible particles relax faster to $a_2 = 1$, the Gaussian behavior, at concentrations where the tube effect is observed. For stiff particles, we observe values that fluctuate between 0.5 and 0.75 at concentrations in the semi-dilute regime, which suggests high dynamical heterogeneity of the system. Only at concentrations below 3 mg/mL the stiff particles relax to $a_2 = 1$. Hence, the relaxation time shows up at later times with increasing concentration, being slower for stiff fdY21M. This difference in the relaxation is related to the flexibility that helps to overcome the constraint imposed by neighboring rods so that diffusion recovers easily to the Gaussian behavior. In other words, the free volume of flexible particles is higher, so it affects directly the diffusion. For the same reason, the Isotropic phase stability is higher than for stiff particles [22, 36]. Doi proposed that a rod would need to reorient to diffuse through the tube, but flexible rod-like particles can relax by another mechanism, such that flexibility promotes the D_{trans} within the semi-dilute regime concentration. The flexible particles would also exhibit a permeation diffusion through the tube, and they would not always need to reorient. At dilute regime, the D_{rot} of semi-flexible rod increases above that of the stiff particles.

We show that at low concentration the length dominates, as D_{trans} is faster for the smaller particle, while at higher concentrations the persistence length prevails over the length, as it is a mechanism to reduce the constraints.

It is important to remark that those are preliminary results. At present, the data obtained is inconclusive since at the same time that we change flexibility we also change the aspect ratio in 1.3 between the particles, which in an experimental system has an effect for an accurate comparison. Hence, more experimental data is required over a broader range of concentrations and for more systems with short flexible and long stiff rods, to cover all possible combinations. In order to have a stronger confirmation, we also need to study the *coupling between the rotational and translational* diffusion which is measured by the displacement of the rod $\triangle\mathbf{r}(t) = r(t) - r(0)$ projected along the long axis $\mathbf{u}(0)$, [165].

8

Conclusions and outlook

This Thesis provides a comprehensive study of the self-dynamics in the liquid crystalline phases and at phase transitions of colloidal rods, using as a model colloidal system the filamentous fd viruses. Concretely, we suggest an approach to characterize the phase transition dynamically. Moreover, we give insight on how the self-dynamics of rod-like particles is affected by the structure of the mesophase, as well as by the physical properties of the particles (length and flexibility).

The fd viruses have been used for decades as a model colloidal system. These biological rods are ideal model systems because they have an aspect ratio larger than 100, they are highly monodisperse, and they form liquid crystalline phases only by entropy driven forces, as Onsager predicted for the I-N phase transition. The fd viruses can be labeled with florescence dyes, which allows for performing the single particle tracking to determine the self-dynamics. In the case of colloidal lyotropic liquid crystals, the self-dynamics can be used to estimate the free volume of the system, since its increase or decrease affects the dynamical behavior at the single particle level. Hence, self-dynamics can be a probe of the entropy of the system. One of the questions that we address in this Thesis is if the self-Van Hove function can be used to characterize dynamics around and at the phase transitions. Also, we have explored if it can be used to measure the deviation from the diffusive behavior, that commonly is measured with the non-Gaussian parameter [166]. Deviation from the Gaussian behavior is interpreted as a result of anomalous diffusion, generally caused by crowding. This behavior has also been observed in the colloidal glass-transition where the self-van Hove function evolves from a Gaussian into a Levy-flight, where dynamical heterogeneity is found [53, 70]. In most of the experimental studies of self-dynamics of fd viruses in their different liquid crystalline mesophases, detailed analysis, and interpretation of the self-van Hove are missing [27–29]. In Chapters 3 and 6 we try to demonstrate that the self-van Hove function can be used to characterize quantitatively the deviation from the Gaussian behavior.

In chapter 3, we have investigated the dynamics of the stiff mutant fdY21M throughout the phase diagram. The phase transitions are entropy driven by a maximization of the free volume which leads to an increase in the free energy of the system.

First, we have investigated the dynamics around the I-N phase transition. In the Isotropic phase close to the phase transition, the increase of volume fraction generates a scenario where the rotational and translational diffusion is restricted, due to the *tube effect*. The study of the translational diffusion reveals a decay of the motion, which is consistent with previous studies [26]. We have shown that not only the diffusion rate is affected, but also the Gaussian behavior, which is reflected in the change of shape of the self-van Hove function. We found that the Brownian motion is very much restricted in the Isotropic phase close to the I-N phase transition. The same behavior has been observed for colloidal glasses [53, 70], and hints to heterogeneous dynamics.

The Gaussian behavior is recovered after the phase transition in the Nematic phase for the parallel diffusion, which is promoted by the orientational order of the phase [26]. The perpendicular diffusion remains frustrated, demonstrated by the deviation from the Gaussian behavior.

The analysis of the self-van Hove with our method is not possible for the N-SmA and SmA-SmB phase transitions, due to the appearance of distinct peaks at one-rod length integer. Furthermore, we discuss the dynamical coexistence found in the N-SmA and SmA-SmB phase transitions. The N-SmA phase transition is known as a first order phase transition [9, 27] and the coexistence can be observed by DIC microscopy. In the case of the SmA-SmB phase transition, the coexistence between phases cannot be performed by DIC microscopy. The only method used to characterize SmecticA and SmecticB has been so far by SAXS [19]. Contrary to the studies of dynamics at the I-N phase transition [24,63], the possible dynamical coexistence at N-SmA and SmA-SmB was not discussed before. Hence, we propose that the order of the phase transition can be determined looking at the dynamics. Two approaches are performed to distinguish the dynamics.

First, for the N-SmA phase transition, we made a dynamical selection between Smectic and

Nematic trajectories, which is possible due to the different dynamical behavior of particles in these two mesophases. This selection is performed using a step detect algorithm, from which Nematic and Smectic trajectories are distinguished. Coexistence of Nematic and Smectic regions observed by optical microscopy are in agreement with the corresponding dynamical behavior of the tracer rods.

Second, for the SmA-SmB phase transition analysis, we assume that non-jumping particles are in the SmecticB phase. We have compared the dynamics within the layer to estimate the particles that do not jump and the ones that do a jump. This is possible by quantifying the probability of a particle to fluctuate within the layer. In the Smectic-B phase, the particles have crystalline order within the layer, which freezes the dynamics.

We showed that for N-SmA and SmA-SmB phase transition, the dynamics could be characterized to determine the order of the phase transition. However, we need to keep in mind that we could have problems of sample homogeneity. At these high concentrations it is highly difficult experimentally to achieve a macroscopic phase separation (as it occurs for the I-N phase transition), so dynamics could be used to identify the phase transition.

As a future approach to investigate the dynamics at phase transitions, it will be interesting to monitor the dynamics while the phase transition takes place. This can be achieved by using a humidity chamber where evaporation of the solvent is performed leading to a change of concentration undergoing the different phase transitions. This way one would avoid homogenization issues during the sample preparation and also we could have an overview of dynamics in real time as the phase transition occurs. Also, a proper fitting for the self-van Hove is required in the Smectic phase, which can relate the values that we get from the potentials with the intensity of the distinct peaks, so that the analysis of the self-van Hove function can be extrapolated to the N-SmA and SmA-SmB phase transitions.

Following the same dynamical characterization with the self-van Hove function as in Chapter 3, in Chapter 6 we have compared the dynamics from the dilute Isotropic up to semi-dilute regime before the phase transition for short stiff and long flexible particles. We have shown a different dynamical behavior depending on the persistence length of the particle. The flexible particles relax faster to the Gaussian behavior at concentrations corresponding to the semi-dilute regime. Hence, flexibility provides a diffusion mechanism to release the constraint imposed by the surrounding rods. It can be related to the fact that the Isotropic phase concentration range is higher for flexible particles [22]. However, our experimental results for D_{rot} are not in agreement with Doi's predictions [51] for infinite stiff, slender rods and neither with the simulation done by Tao *et al.* with rods of $L/D \cong 60$ [60]. This could be due to hydrodynamic and electrostatic interactions that are not considered in the simulations, as well as to the effect of flexibility in the experimental system. The results for our systems are limited due to the analysis of the data in 2D. In the isotropic phase, we have short correlated time trajectories due to particles going out of focus.

Hence, in follow-up studies, it will be interesting to consider other combinations of physical properties as short and flexible particles and long stiff particles to gain insight on the effect of flexibility and length. Moreover, with a solvent with higher viscosity, which slows down the rotation of the rod, the measure of the rotational diffusion would be easier. Another alternative approach would be to use confocal microscopy.

Previous studies on the dynamics of the Smectic phase motivated us to consider a more complex system as it was the case for the guest-host system that we propose in Chapter 4. The dynamics in the Smectic-A phase of fd viruses are characterized to be hopping-type behavior, in which the particles jump through layers. It has been proved that flexibility also affects the dynamics in the Smectic phase [29].

We have proposed a different approach, from the pure Smectic system, where the dynamics of the Smectic host are compared with semi-flexible long guest particles introduced into it. Generally, a big size of the particle is related to slow dynamics, also observed in the crowded system. We have shown that this is not the case for long particles that are included in a Smectic phase of slightly shorter particles. This is related to the concept of the non-commensurate particle. We suggested that the Smectic potential is not a fixed value, but a result of fluctuations within the layer. The long guest particle has part of its volume included in at least 2 adjacent layers, which promotes the diffusion through the host Smectic layers. The confinement that the long guest particles experience in the host Smectic phase, induce a faster diffusion which disappears when entering the Nematic phase. The results of the analysis of the dynamics within the layer proved that the D_{per} of the long semi-flexible guest particles is restricted. Furthermore, we have observed phase separation of the longer particles with time. This phase separation is expected due to the size mismatch. Recently, it has been shown by simulations that at relatively short time scales, where caging of particles by neighbors predominates the kinetics; the more flexible particles move faster in a pure Smectic phase. The flexibility will cause a *softer* cage effect [116]. However, in our guest-host system, the cage effect is caused by the stiffer host particles. The same study with stiff guest particles would tell if flexibility is a critical feature to release the constraint imposed by the host system, or if it relies only on the non-commensurate effect. These results showed that diffusion for longer particles is not always slower, depending on the structure of the matrix and the size ratio between the guest and host particles. This could be attractive to study and to improve materials with better permeation properties, such layered membranes through which particles could diffuse faster. Thus, it would be a nice finding for example in drug delivery materials.

During these experiments in the guest-host Smectic phase, we have been able to track the dynamics of the guest particles placed in grain boundaries. We present these results in Chapter 5. It seems that particles can diffuse from the Smectic layers to the defect line dislocation within a grain boundary. It has been demonstrated that break of geometry caused by the defects may induce superdiffusion in crowded systems [144]. We have been able to calculate dynamics of guest M13KO7 particles, where a slightly superdiffusive behavior has been observed in particles that diffuse from the Smectic domain into a grain boundary. Also, a nematic-like behavior is observed for the particles located within the line defect of a grain boundary. This poses the question of the nature of the host sample within these line defects.

In conclusion, in this Thesis we have shown that the self-dynamics is a signature for the phase transition of colloidal fd viruses. The Self-dynamics gives detailed information of the free volume of the system around the phase transitions. Consequently, we can measure the relaxation of the dynamics when approaching the phase transitions and also the dynamical coexistence. Moreover, the dynamics of a smectic guest-host system, where the surrounding energy landscape has a smaller length scale than the guest particle, demonstrates that a bigger particle can be faster. In this conditions, also the super-diffusion of the guest particle is observed when it diffuses into a grain boundary. Hence, the fact that fd rods are such a versatile system allowed us to play with different physical properties of the particles to understand more complex systems. Moreover, the self-dynamics can be accurately measured using fluorescence microscopy techniques. This is a step forward to understand the dynamics of colloidal structured systems and also in the development the new materials in which the dynamics of the particles introduced can be controlled.

This thesis treats the dynamics of the different liquid crystalline mesophases and phase transitions of a model colloidal of rod-like particles: the fd viruses. The study of the self-organization of colloidal liquid crystals treats the simplest phenomena of forming structured systems. In a system where anisotropic particles have hard core interactions, the self-organization is purely entropy driven due to the maximization of the free volume of the system. Thus, the measure of dynamics at the single particle level provides information on the available free volume and the structure of the mesophase. Hence, the dynamics can be used to characterize phase transitions and solve issues such as the entropic gain of a phase transition, the order of the phase transition and to find a dynamical signature. We measure the relaxation of the dynamics when approaching the phase transitions and also the dynamical coexistence and the effect of flexibility and length as a mechanism to release the constraint of the neighbors. Moreover, the dynamics of a smectic guest-host system, where the surrounding energy landscape has a smaller length scale than the guest particle, demonstrates that a bigger particle can be faster. In this conditions, also the super-diffusion of the guest particle is observed when it diffuses into a grain boundary. Hence, fd rods are a versatile system and their self-dynamics can be accurately measured using fluorescence microscopy techniques. This is a step forward to understand the dynamics of colloidal structured systems and also in the development the new materials in which the dynamics of the particles introduced can be controlled. The extensive experimental results are completed by a whole analysis and interpretation, being very promising and challenging

9

Appendix 1

9.1 Two-dimensional single particle tracking for the study of dynamics

Fluorescence microscopy allows us to collect good quality images of the fluorescence-labeled particles to perform the particle tracking analysis. Single-particle tracking is a different approach appeared in the 80's and combined high spatial and temporal resolution. It provides information that is not available by Fluorescence Recovery After Photobleaching (FRAP) or other methods that study the collective diffusion of the particles of the system. Single-particle tracking is based on the individual location of a particle with micro or nanometer precision, measuring its individual dynamics as a function of time. However, it is necessary to develop algorithms to get the trajectories and analyze the diffusion obtained from the image analysis. The centroids of the particles are located and continuously linked in time between frames to generate the trajectories, as shown in Fig9.1. Later, these trajectories can be analyzed using different approaches, such as the *Mean squared-displacement* or the *self-van Hove function*, as we have seen throughout this thesis.

At the same time, the big disadvantages are the background fluorescence noise produced by particles out of focus and the photobleaching of dyes over time. Also, different factors influence the quality of the video microscopy: exposure time, frame rate, detection noise, etcetera.

The aim of this section is to present the algorithms used to perform the single particle

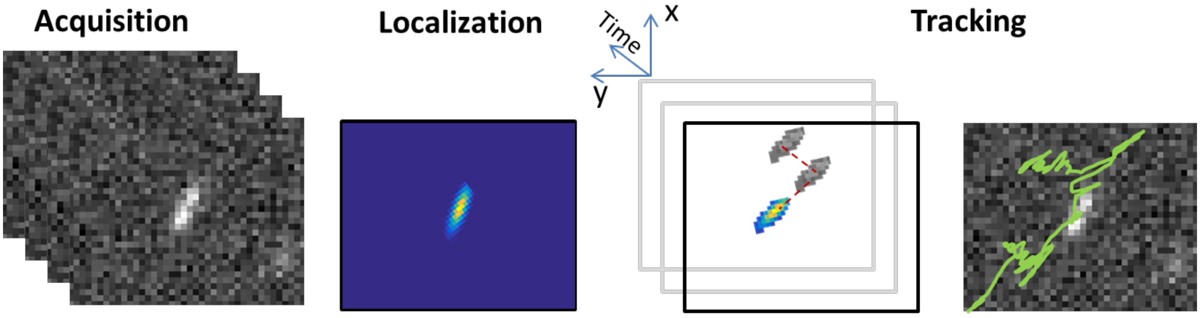

Figure 9.1: *Different steps of particle tracking method.*

tracking analysis and how the parameters are determined to identify, locate and track rod-like particles and study their dynamical behavior. For this purpose, we use a Matlab particle tracking code, which has been improved from an existing version of IDL for particle tracking. Nevertheless, we need to set some parameters within the algorithm to treat the movie and collect the right information from it. In this section, the goal is to explain the function of each algorithm as well as the criteria followed to set the different parameters within these algorithms to optimize the analysis for our systems.

9.1.1 Particle Location: determining the position of the particles

The first thing to consider is the type of system that we are studying and the settings of our instrument. In the Guest-Host system, for example, there are two kinds of rod-like particles labeled with different dyes: fdY21M and M13KO7 labeled with Alexa488 and Dylight550 respectively, in a matrix of a concentrated Smectic phase of fdY21M. This is something to take into account for the particle location because the size of the particles and the intensity of the dye depend directly on them. It has been observed that the life time for Dylight550 is longer than for Alexa448 due to the smaller effect of the photobleaching.

In all of the movies analyzed, we work with frame rates of 33 fps and 50 fps corresponding to 20 and 5 ms exposure time, at 100x magnification (oil immersion objective) and at binning two. The camera used is sCMOS, knowing that for the sCMOS camera one pixel is $6.5\mu m$, the size of a pixel at binning 2 using a 100x immersion oil objective can be easily calculated using equation 1, which gives that one pixel is $0.13\mu m$.

$$pixelsize = \frac{camerapixelsize \times binning}{objective\ magnification \times objective\ lens\ magnification \times Cmount} \tag{9.1}$$

The theoretical values of length and width of both particles are compared by measuring the particles with ImageJ. We found a big difference in the width of the particles measured due to the resolution limitation of the camera. While the theoretical value D_{theo} would correspond to 0.03 pixels, the minimum value for the experimental diameter D_{exp} is 1 pixel, because this is the minimum unit of the resolution of the camera.

Table 9.1: *Theoretical (L_t) and experimental length L_{exp}, experimental diameter D_{exp}. Units in pixels*

	L_t	D_{exp}	L_{exp}
fdY21M	7	1.8 ± 0.2	6.8 ± 0.6
M13KO7	9	2 ± 0.1	8.9 ± 0.7

During the process of particle location, the program approximates the candidate particles by looking at the brightest pixel. After this step, the location is refined by calculating the centroid-weighed position using a 2D-Gaussian fitting, which also determines the x (parallel) and y (perpendicular) axis and the angle with respect to the axis. This process requires certain functions and parameters as described in Table 9.2.

Table 9.2: *Functions and their corresponding descriptions using in Matlab for the Particle location from the fluorescence movies*

Function	Description	Parameters used
bpass	Filtering and smoothing of the image	image, bp1,bp2
pkfnd	Find the local maxima intensity in a picture within a pixel level accuracy. Rough particle positon.	image, min.intensity si
parapos_angle	Calculates the centroid of the brighest spot with sub-pixel accuracy. Gaussian fitting to determine the long and short axis and the angle	image, sz, contrast, aspect.ratio si

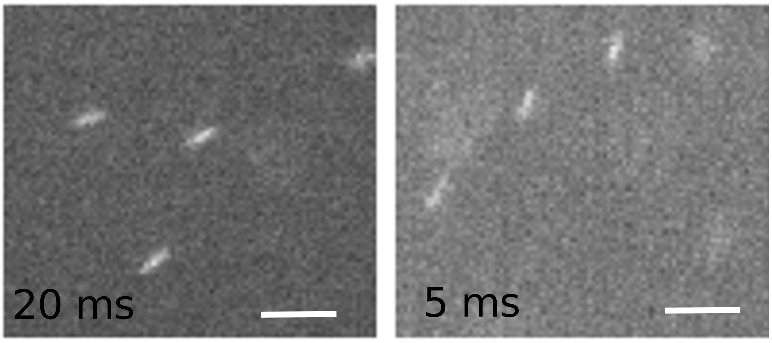

***Figure 9.2:** Example of difference in background noise between two fluorescence images taken at different exposure times. The scale bar is 2μm.*

The process of particle location collects the information frame by frame, until a chosen maximum number of frames. Moreover, specific parameters must be set to perform the particle location. However, how do we know which are the right parameters to perform the analysis? It is important to consider the physical meaning of these parameters and to take into account the limitations of the instrument. As mentioned before, there are some factors that influence the quality of the image, coming from the instrument:

- Exposure time and frame rate: it depends on the sensitivity of the camera, the intensity of fluorescence emission of the particles and the overall tolerance noise.
- Detection noise: the noise is the standard deviation of the brightness in the region that excludes in-focus and out of focus particles. The SNR (signal to noise ratio) is proportional to the rate of photoelectrons conversion in the process that takes place in the detector, which converts light power to electrical current, on an active-pixel sensor (CMOS). The SNR can be improved increasing the light or integration time

Furthermore, some parameters depend on the sample: the concentration of the labeled particles added, the concentration of the sample and as a consequence the phase of the sample (Smectic, Nematic, isotropic), and also the type of dyes used to label our particles. The parameters for the particle location algorithm are shown in Tab.9.3. The particle location algorithm is divided into different stages as explained below.

Filtering. The first step in the particle location is the filtering of the raw image to avoid contrast gradients that complicate the process of identification of particles. The image has non-uniform background intensity, and it must be corrected before the analysis. For that purpose

Table 9.3: *Parameters and their corresponding descriptions using in the Matlab functions for the Particle location from the fluorescence movies.*

Parameter	Description	Physical meaning
bp values	values to smooth and discriminate noise	
image	image that is treated	
sz	twice the distance of the partilce picture within a pixel level accuracy.	Separation between particles. Depends on concentration
min.intensity	the minimum brightness of a pixel that might be local maxima	Intensity of the particle
si	Size of the square window for the Gaussian fitting	Depends on the length of the particle
contrast	minimum value for the position to be kept	Signal to noise ratio
aspect	minimun aspect ratio	Calculation of L/D in pixels

we use the *band pass values (bp1 and bp2)* . The first value is referred to the intensity of the noise correlation (ξ) and the second value to the region dimension (w). If we increase the difference between those two values, the brightness will increase, as shown in Fig.9.3. During the filtering of the image, it is necessary to have a value of bp2 which makes the particles look brighter but without making the background blurry.

Location of particles. Once the image is already filtered, the function pkfnd.m estimates the brightest centroid at pixel-level accuracy from which the initial positions of the particles (x_0, y_0) are obtained. For this estimation, the minimum intensity and the minimum distance between particles parameters must be determined. The minimum intensity parameter is just the intensity threshold value for identifying the brightest pixels. We can determine the maximum value in Matlab. The bigger the value, the fewer particles we will keep. This parameter is tested for each concentration. The effect of the photobleaching in the minimum intensity needed is also tested with the program *FirstLasFrame_Analysis.m*, which compares the percentage of particles located between the first and the last frame. The limit distance between to particles, *the si parameter*, is applied in order to avoid two particles to be considered the

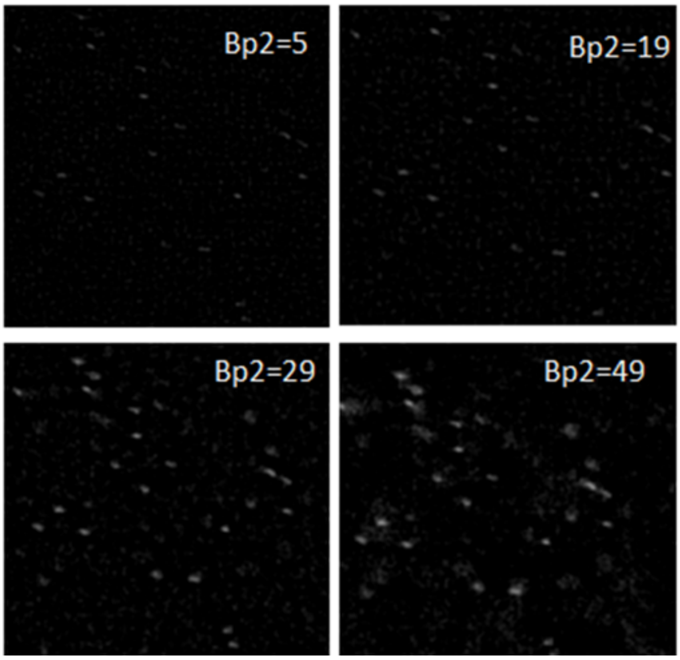

Figure 9.3: *Different values of the filtering parameter bp2. When increasing this value we increase intensity of the brightest pixel but also the image becomes blurry.*

same when two particles overlap by diffusion, as shown in Fig.9.4. It needs to be at least one virus length in pixels to avoid dimers as two particles or big objects as many particles. The minimum distance between close particles has been measured manually between 215 particles at each concentration and taking into account events where the particles overlap.

The next step is refining the initial location to obtain a location with a sub-pixel resolution from the raw image. This is done by fitting the shape of the *ith* particle using a Gaussian function and applying some extra criteria to remove possible contamination locations. A 2D Gaussian fitting is done around the particle Image I_i, where the orientation and the short and long axes of the particle are specified:

$$I_i = I_0 exp(-\frac{|r - r_i|}{S^2}). \tag{9.2}$$

To set the size of the square around the particle (Fig.9.4a), we use the *sz parameter*. The correction is calculated as

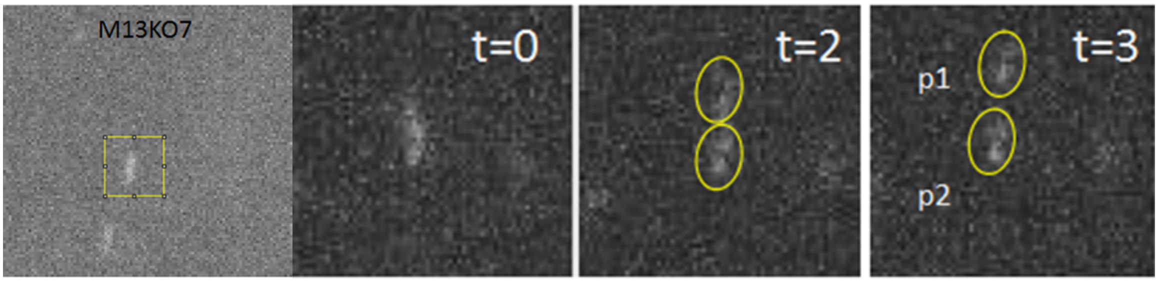

Figure 9.4: *Fluorescence images of two particles that overlap in the image and them separate with time due to parallel diffusion. The yellow circles indicate the two different particles, p1 and p2.*

$$\begin{pmatrix} \varepsilon_x \\ \varepsilon_y \end{pmatrix} = \sum_{i^2+j^2 \leq w^2} \begin{pmatrix} i \\ j \end{pmatrix} I(x_{0+i}, y_{0+j}), \tag{9.3}$$

where I is obtained from the Gaussian fitting. The final refined particle location is

$$(x_i, y_j) = (x_0 + \varepsilon_x, y_0 + \varepsilon_y). \tag{9.4}$$

Moreover, an extra selection is done from the centroids obtained from the 2D-Gaussian fitting, using the parameters *contrast* and *aspect*. Contrast is defined as difference in light intensity between the image and the adjacent background relative to the overall background intensity (or as described above SNR):

$$I_0 - d = \frac{I_{signal} - I_{noise}}{\sigma noise} \tag{9.5}$$

The values for both particles are calculated and set as 5 over all frames. This value could change depending on the movie, and the field of view, but in general, thanks to the filtering of the image for our sample it stays constant during all phases. It is the minimum value for the contrast.

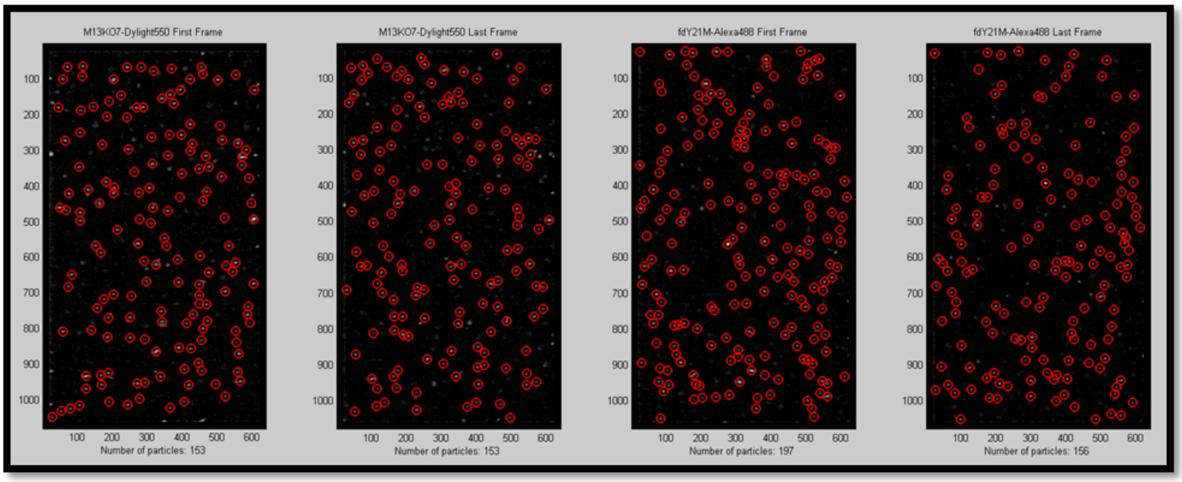

Figure 9.5: *Result of the Particle Location program of two types of particles, comparing the first and last frames of the movie. Red circles identify each single particle.*

The *aspect parameter* sets the minimum aspect ratio for each particle to be considered. When the particles are beads, the aspect ratio is 1. In our case, we have anisotropic particles, which means that the aspect ratio is bigger than one. In pixels we have an aspect ratio of about 2-3, bur to be sure that all particles are located even if some of them get out of focus, we decided to set this value between 1-2.

With all these parameters set, we use the program $FirstLastFrame_Analysis.m$ to check if they are the correct ones for our system. Since there is an effect of photobleaching, this program allows us to also compare the first and last frame with the same parameters, and confirm that we can keep them constant with time. Since there are two types of particles, we will have the option to set them for each particle. Less than 20% of particles are lost from the first frame to the last frame.

In conclusion, having different factors in mind and also the physical properties of our sample, we set parameters to perform our analysis. For other systems, with different physical properties than the viruses, following these steps, it would be possible to do a proper analysis.

9.1.2 Particle tracking: connecting the position in time

Once the particles are located frame by frame, the next step is to generate the traces by relating in time the different particle positions. This is done by inputting the data file with the coordinates and also setting the parameters for the particle tracking. The algorithm links the positions by using separation-based criteria, such as the nearest-neighbor distance. The pairs of localizations showing the minimum distance are selected as the most likely situation of the same particle in successive frames and are linked together. Repeating this procedure over all the particles and all the frames finally provide the reconstructed trajectories.

Table 9.4: *Functions and their corresponding descriptions using in Matlab for the Particle tracking from the fluorescence movies*

Function	Description	Parameters used
tracks_2D	construct 2-dimensional trajectories from a list of coordinates	position, maxdisp memory, good
CentRotLoc	Center all traces and calculate the angle for each trace. Rotation of the trace	thetaUse, tracks
MSDsvh_rod	Calculates the MSD, P2 and self-van Hove list	stack, mindisp

As explained before, there are some parameters that depend on the type of particle that we are analyzing. In our sample, we have observed that the dynamics of M13KO7 are slightly different from fdY21M, so this is a key point to build consistent trajectories for each particle. Also, the mesophase affects the construction of trajectories, since for example in the Smectic phase we have almost no particles going out of focus within the time duration of the movie, while in the Isotropic phase particles are continuously going in and out of focus. The parameters shown in Table 9.5, indicate the main criteria followed to have a well-connected trajectory. The values of these parameters change for each virus and each mesophase as it is reported at the end of this Appendix.

After obtaining the trajectories, the next step is the calculation of the Mean squared displacement. The trajectories need first to be centered and rotated, using the *CenRotLoc* function. It centers the trajectories on the artificial XY axis that Matlab creates. After, the traces

Table 9.5: *Parameters and their corresponding descriptions using in the Particle tracking program*

Parameter	Description	Physical meaning
memory	Number of frames that a particle can be lost and recovered to be considered the same	Particle in-out focus
good	minimum number of frames for a trajectory to be considered	minimum length of a trajectory
Max.displacement	maximum numbers of pixels that a particle can move between 2 frames	Depends on the mesophase
Min.displacement	minimum number of pixels that a particle can move	use to avoid stuck bodies
positions	coordinates of the particles obtained from particle location	Positions

are rotated using the individual angle for each trace, which is calculated from the probability distribution function for the orientation of the rod. The MSD is calculated for a particle j whose position is sampled at N discrete times $m\Delta t$,

$$MSD = \frac{1}{N-m}\sum_{i=1}^{N-m} x_j(t_i + m\Delta t) - x_j(t_i))^2, \tag{9.6}$$

This process is done to each single particle and averaged over all of them in each movie. The further analysis is done by Origin to get the diffusion coefficients and exponents from the MSD. At the same time, the program creates a list with the information at each time step to calculate the self-van Hove function using the program *Self-van Hove calculation*.

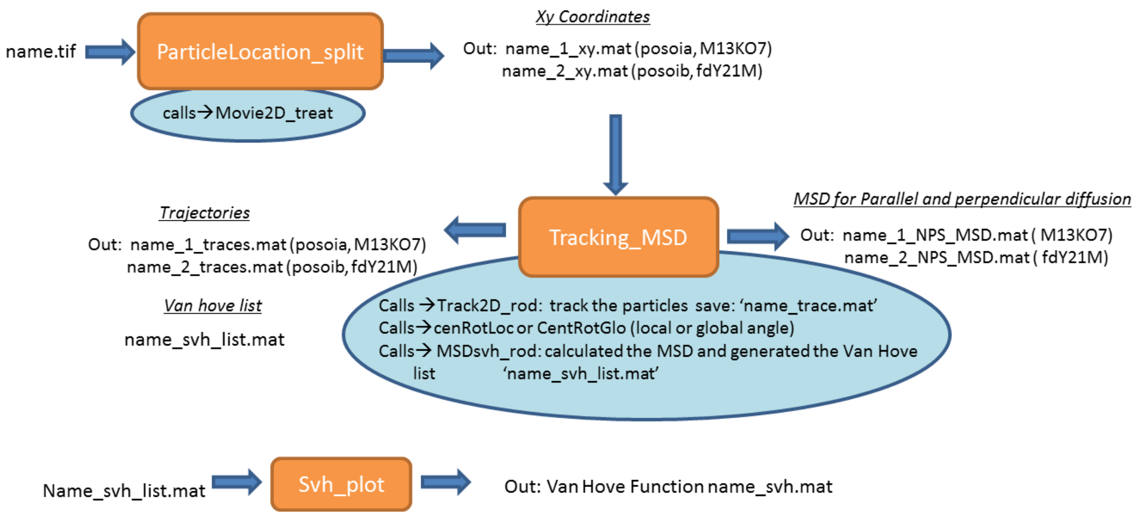

Figure 9.6: Flow chart of the particle tracking program.

9.1.3 Jumping detection

The algorithm of the jump detection is a key point in the analysis of the N-SmA phase transition in Chapter 3. We recognize the jump due to a sharp transition in the trajectory which is recognized by the program. The algorithm constructs a set of scaled derivatives of the input data. First, it detects a maximum (or minimum) value that persists at a coarse scale to ensure the features we detect are significant (e.g. not due to noise). We then track these features through the other scaled derivatives; at the end, we have a reasonably confident measure of where significant edges occurred in the data, in this case, the dramatic change of position due to jumps.

Table 9.6: *Parameters used in the jumping detection algorithm*

Parameter	Description
scales	can be lost and recovered to
threshold	minimum number of frames for a
SD	coordinates of the particles

The selection of scales, therefore, is crucial in this analysis. If the scales considered are too fine, false edges due to noise will be detected. If the scales considered are too coarse,

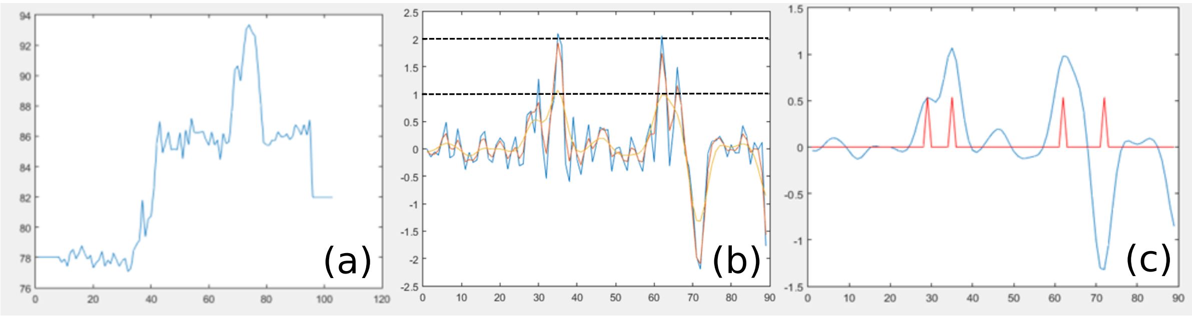

Figure 9.7: *a) Raw position versus time of the jumping particle b) Scales created from the derivatives of the position c) Detection of the minima and maxima from the scales by using the parameter threshold, indicated by the horizontal dashed line.*

significant features may be missed. The parameters needed for this program are shown in Table9.6

We obtain a profile which will be used for the identification of the jumps, as results of a convolution of the Gaussian Kernel of a width given by the amplitude of the scale parameter and the derivative of the data, as it is shown in Fig9.7. Given a threshold parameter, the program will look for those peaks that are within the value. The position of the peaks will be the position of the limit of the jumps. Then, *Minimum jump* is used to confirm that the difference in distance between the recognized jumps is above the value introduced. Otherwise, it will not be considered as a jump. In our case, the minimum jump is an approximately one-rod length.

Fig.9.7c illustrates the importance of thresholding. Here we have used a high initial threshold only to find very prominent features of the data set. Only the two strongest positive step edges are detected. For a given threshold, n, the edge detection application will compare a local maximum, in the derivative to the global maximum.

Moreover, this algorithm has been further refined by including the parameter SD, which is the standard deviation within a residence to be considered Smectic behavior. This is done due to the limitation of the original program to distinguish the Nematic and Smectic trajectories when the jumps in the Smectic phase start to be less sharp.

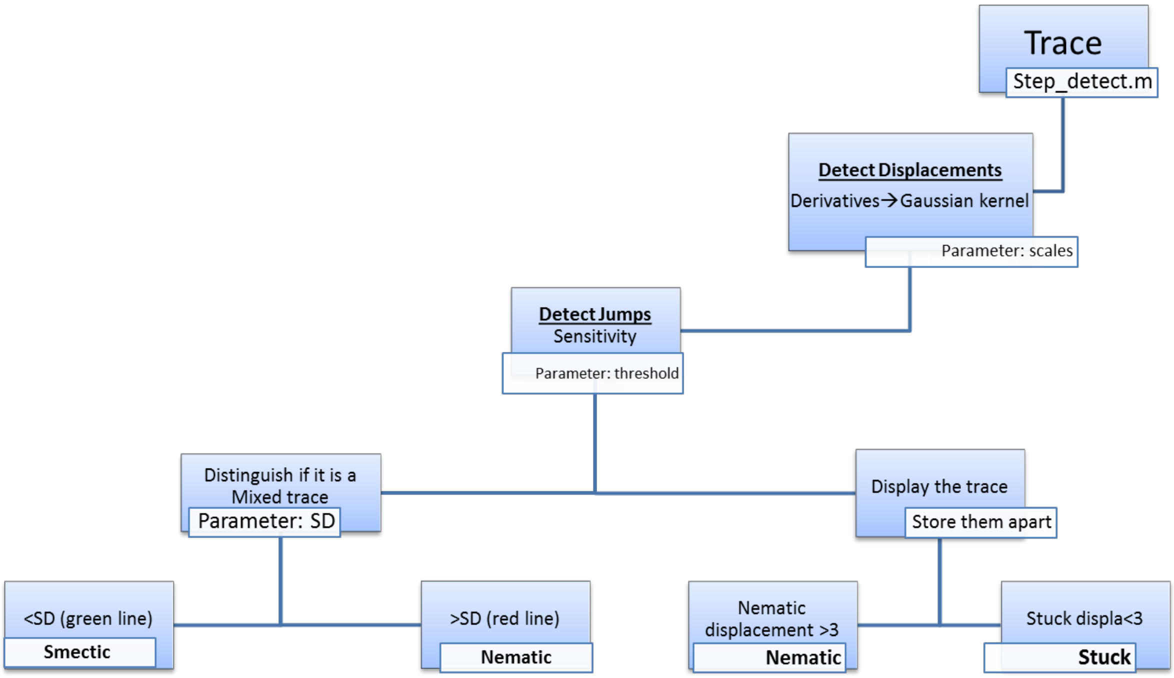

Figure 9.8: *Flow chart of the step detection program to distinguish Nematic and Smectic trajectories.*

9.2 Calculation of Smectic potentials: PSF and deconvolution

After the data acquisition, all videos have been treated with a Particle Tracking Algorithm. The particle tracking gives us information about the dynamics which has to be quantified by calculating the Mean-squared displacement, the self-van Hove function and in the case of the Smectic phase also the Smectic ordering potentials. During the data treatment process, we need to take into account several considerations as it is explained in this section.

9.2.1 PSF and deconvolution in Florescence microscopy

Fluorescence imaging is a versatile technique commonly used in biology to visualize cellular components, proteins or molecules of interest. Also, it is a useful tool to study dynamics of colloids, where the particles can be easily functionalized with different fluorescent dyes, and movies in real time are recorded for their further analysis. When using Fluorescence microscopy, the sample is illuminated with light having the wavelength in the absorption spectrum of the fluorescence molecules of the sample, which will be excited and will emit light of a longer wavelength. This is detected by a camera appended to the microscope which will acquire a two-dimensional image of the light intensity. During this process, diffraction of light will occur, causing blurring which is a nonrandom spreading of the light caused when it passes through the lens and the sample. The final image will be a combination of the light of the in-focus objects and the light caused by the blurring, making deconvolution necessary to remove blur. Blur is considered a function of the microscope system, principally of the objective lens so it can be easily modeled. For this reason, the concept of point spread function (PSF) is introduced. We consider the point spread function as the smallest point source of light. Since the camera cannot focus all this light into a perfect 2D image, the point appears spread into a 2D diffraction pattern. The convolution operation applies the PSF to every point in the object, convolving the light emitted from each point with the PSF.

The procedure of deconvolution allows us to recover the real data from this convoluted in-focus object with the out of focus information. This is all due to the diffraction effect, which refers to diffraction of light when it goes through a small opening. This diffraction d due to the resolution of the microscope can be written as

$$d = \frac{1.22}{NA} \tag{9.7}$$

The point spread function or diffraction pattern depends strongly on the Numerical Aperture (NA) of the objective lens. In an ideal situation, the light would travel in a straight line, creating from a point object a point image. The light will get through an objective lens with an angle α. Thus, the highest resolution depends on this angle α and on the Numerical aperture, which is determined by α.

$$NA = \eta \sin \alpha \tag{9.8}$$

where η is the index of refraction of the medium. At larger numerical aperture we will have better resolution, having a sharper point spread function while at smallest numerical apertures it will be broader. Resolution is defined as the smallest resolvable distance between two points of light source,

$$Resolution(x,y) = \frac{0.61\lambda}{NA} \tag{9.9}$$

Resolution is affected by this diffraction pattern. According to the Rayleigh criterium, two objects are in the resolvable when the maximum intensity of one diffraction pattern is over the first minimum of the other.

To understand the main idea of deconvolution, we first should explain what the convolution process is (of the real image with the psf) and the mathematics behind it. Given two functions f(x) and g(x), f(x) being the real image and g(x) the point spread function, and the convolution gives the amount of overlap of the function g(x) (PSF) as it is shifted over the function f(x) (image).

$$(f*g)(x) = \int f(a)g(a-x)dx \tag{9.10}$$

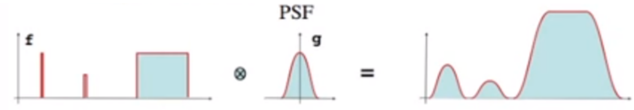

Figure 9.9: *Convolution of two functions and the results obtained.*

The reciprocal process is the deconvolution, where the contribution of the PSF is removed for the signal (final image) to get a more accurate image of the object.

During data acquisition, the accuracy of the determination of the centroid of the particle plays a major role in the final results. This accuracy could decrease due to the *static error* (smearing due to optical aberrations) and *dynamics error* (due to the fact that the particle is moving) [167], and this error when determining the center of the particles propagates through the calculations, showing up for example, in the MSD as the offset.

9.2.2 Calculation of the Smectic potentials and deconvolution

In chapter 3 and 4 we have shown the results of raw and deconvoluted Smectic potentials. In order to perform the deconvolution process, we first get the Point spread function (PSF).It has been obtained with immobile viruses fixed on the glass coverslip of the sample under the same experimental conditions, as shown in Fig.9.10. For a 100x oil objective of NA 1.4, the resolution for the sCMOS camera used in the experiments is 0.2 μm. Our point spread function represents the smearing the particle location due to the limited experimental resolution. One of the key points of using fd bacteriophage for the study of dynamics is the colloidal scale (with an aspect ratio L/D larger than 100) that enables imaging of individual viruses and to observe them as anisotropic particles.

Despite the deconvolution is most of the times done directly during the image processing, we applied the deconvolution analytically on the raw data obtained from the image analysis. For the calculation of the Smectic ordering potentials, we measure fluctuations within the layer, collecting positions for each fluctuation from the center of the Smectic layer. At high concentrations in the Smectic phase, we have completely stuck particles that are not fluctuating. Thus, this signal has a maximum probability, and it needs to be deconvoluted from the final signal of all particles, which is the convolution of fluctuating particles and completely stuck particles.

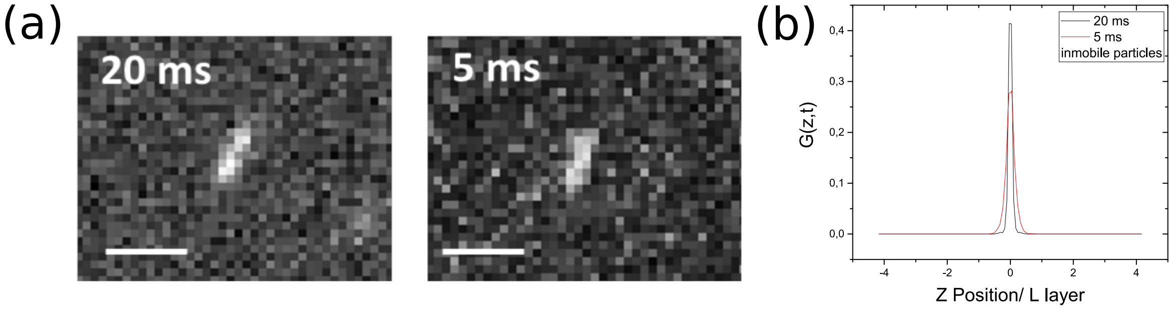

Figure 9.10: *a) Fluorescence picture for 20 and 5 ms exposure times. For low exposure times the SNR is lower. b) Point spread function for 5 and 20 ms exposure times obtained from the probability of the non-moving particles close to the phase transition*

Exposure time has an effect on the quality of the image, where background noise increases when decreasing the exposure time, and the signal of the particles smears. The direct consequence of decreasing the exposure time is the increase of the error when determining the position of the center of the particle. Thus, at different exposure times, we will get different PSF (Fig.9.10). The effect of the smearing of the particle brightness signal due to diffusion or exposure time is also a factor to take into account when applying the deconvolution.

We first calculate the raw potentials. This is performed by converting the probability function P(z) of finding a particle at position z with respect to the middle of a layer to the smectic ordering potential $U_{layer}(z)$ via the Boltzmann law

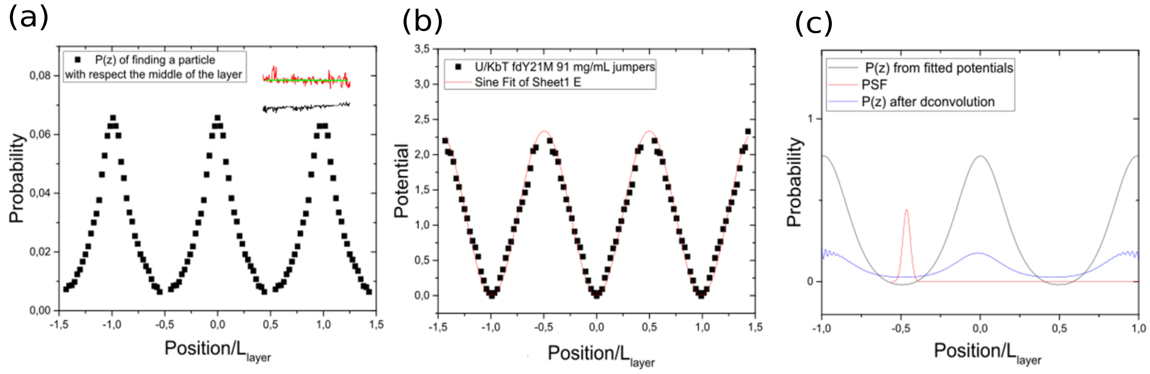

Figure 9.11: *a) Probabilities P(z) obtained from the histogram of position of the particle from the middle of the layer (inset). b) Raw Potentials U_{layer} (black squares) obtained from the P(z) using the Boltzmann factor for Smectic Potentials. Red line is the fit with the sine function. c) Representation of the P(z) before deconvolution (black line) and after deconvolution (blue line) from the PSF (red line).*

$$P(z) \sim exp[-U_{layer}(z)/k_B T] \tag{9.11}$$

To obtain the total ordering potential, the particle distributions in a single layer are added periodically to themselves at all integer numbers of layer spacing L_{layer}. All potentials can be best fitted with a sinusoidal function

$$U_{layer}(z) = U_0 sin(2\pi z/L_{layer}) \tag{9.12}$$

We show this process in Fig.9.11. Then, the fitted sine function is deconvoluted from the

PSF calculated. Hence, the deconvoluted potential is lower than the raw potential obtained from the probability. We found out that the contribution of the point spread function for the particles at high concentrations with approximately 80% stuck particles (100 mg/mL for fdY21M) in the Smectic phase makes the convolved data asymmetrical, being not possible to fit it with a sine function anymore (Fig.9.12).

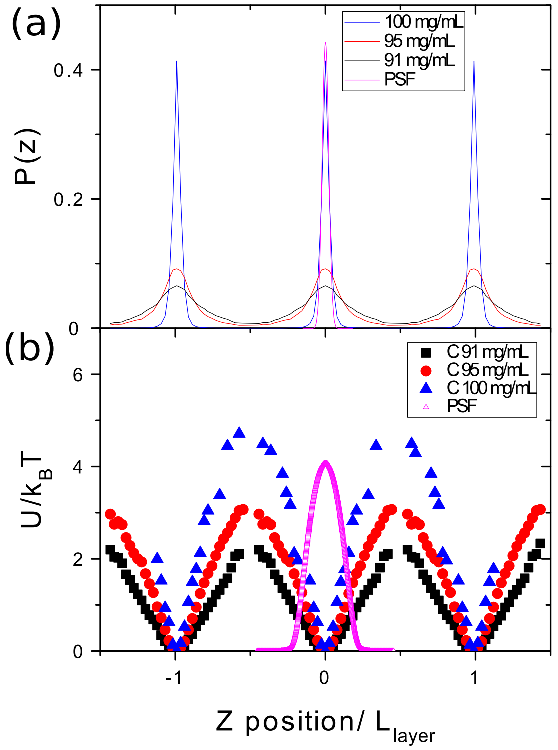

Figure 9.12: *a) Probabilities obtained for 3 concentrations in Smectic phase b) Corresponding raw potentials before the deconvolution. The psf is represented with pink color.*

This is because the particles are not fluctuating but are completely stuck on the layer, making the profile of the probability sharper. For concentrations below the Smectic range for fdY21M and for M13KO7 particles that exhibit Nematic like diffusion in the Smectic background, we found a limitation during the deconvolution, where the results of the deconvolution are noisy. The fact that particles are not commensurate within the Smectic layers gives results that we do not have Smectic ordering potentials (values below 1 K_BT) and the deconvolution of the PSF for the sine function is not valid anymore.

Finally, we simulate the convolution process using the value of U_0 for a given concentration

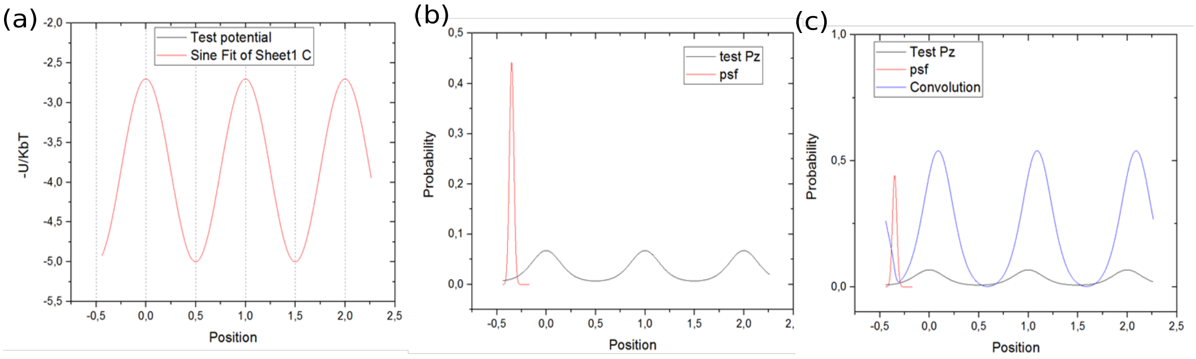

Figure 9.13: *Simulation of the convolution of the real potential and the psf at 91 mg/mL a) Probabilities P(z) obtained from the sine function (Eq) b) Raw Potentials* U_{layer} *(black squares) obtained from the P(z) using the Boltzmann factor for Smectic Potentials. Red line is the fit with the sine function. c) Representation of the P(z) before deconvolution (black line) and after deconvolution (blue line) from the PSF (red line).*

after the deconvolution, as shown in Fig.9.13. We first generate the sine function corresponding to the probability $P(z)$, and then we convolute using Origin with the psf function.

Bibliography

[1] O. Lehmann. Über fließende Krystalle. *Zeitschrift für Physikalische Chemie*, 4:462–472, 1889.

[2] H. Zocher. Über freiwillige strukturbildung in solen. (eine neue art anisotrop flüssiger medien.). *Zeitschrift für anorganische und allgemeine Chemie*, 147:91–110, 1925.

[3] W. M. Stanley. Isolation of a Crystalline Protein Possessing the Properties of Tobacco-Mosaic Virus. *Science*, 81:644–645, 1935.

[4] F. C. Bawden and N. W. Pirie. The isolation and some properties of liquid crystalline substances from solanaceous plants infected with three strains of tobacco mosaic virus. *Proceedings of the Royal Society of London. Series B, Biological Sciences*, 123:274–320, 1937.

[5] A. Stroobants. Columnar versus Smectic Order in Binary mixtures of hard parallel spherocylinders. *Physical review letters*, 69:2388–2391, 1992.

[6] A Patti, DE Masri, R Roij, and M Dijkstra. Collective diffusion of colloidal hard rods in smectic liquid crystals: Effect of particle anisotropy. *The Journal of Chemical Physics*, 132(22):224907, 2010.

[7] L Onsager. The effects of shape on the interaction of colloidal particles. *Annals of the New York Academy of Sciences*, 51:627–659, 1949.

[8] P van der Schoot. The Nematic-Smectic Transition in Suspensions of Slightly Flexible Hard Rods. *Journal de Physique II*, 6:1557–1569, 1996.

[9] J Polson and D Frenkel. First-order nematic-smectic phase transition for hard spherocylinders in the limit of infinite aspect ratio. *Physical Review E*, 56:6260–6263, 1997.

[10] T D Pollard. The cytoskeleton, cellular motility and the reductionist agenda. *Nature*, 422:741–5, 2003.

[11] A F Huxley. Muscular contraction. *J Physiol*, 243:1–43, 1974.

[12] J Newman, H L. Swinney, and L A. Day. Hydrodynamic properties and structure of fd virus. *Journal of Molecular Biology*, 116:593–603, 1977.

[13] S B Zimmerman, , and A P Minton. Macromolecular crowding: Biochemical, biophysical, and physiological consequences. *Annual Review of Biophysics and Biomolecular Structure*, 22:27–65, 1993.

[14] R. John Ellis. Macromolecular crowding: Obvious but underappreciated. *Trends in Biochemical Sciences*, 26:597–604, 2001.

[15] B Hess and A Mikhailov. Self-organization in living cells. *Science*, 264:223–224, 1994.

[16] P Bernado, J García de la Torre, and M Pons. Macromolecular crowding in biological systems: hydrodynamics and NMR methods. *Journal of molecular recognition*, 264:397–407, 2004.

[17] F Höfling and T Franosch. Anomalous transport in the crowded world of biological cells. *Reports on Progress in Physics*, 76:046602, 2013.

[18] D Gnutt and S Ebbinghaus. The macromolecular crowding effect - From in vitro into the cell. *Biological Chemistry*, 397:37–44, 2016.

[19] E Grelet. Hard-rod behavior in dense mesophases of semiflexible and rigid charged viruses. *Phys. Rev. X*, 4:021053, Jun 2014.

[20] S Fraden. Phase Transitions in Colloidal Suspensions of Virus Particles. *Observation, Prediction and Simulation of Phase Transitions in Complex Fluids*, pages 113–164, 1995.

[21] Z Dogic and S Fraden. Smectic phase in a colloidal suspension of semiflexible virus particles. *Physical review letters*, 78:2417–2420, 1997.

[22] E Barry, D Beller, and Z Dogic. A model liquid crystalline system based on rodlike viruses with variable chirality and persistence length. *Soft Matter*, 5:2563–2570, 2009.

[23] R Brown. A brief account of microscopical observations made in the months of june, july and august 1827, on the particles contained in the pollen of plants; and on the general existence of active molecules in organic and inorganic bodies. *Philosophical Magazine Series 2*, 4:161–173, 1828.

[24] A Modlińska, A M Alsayed, and T Gibaud. Condensation and dissolution of nematic droplets in dispersions of colloidal rods with thermo sensitive depletants. *Nature Publishing Group*, pages 1–10, 2015.

[25] Y G Tao, W. K. Den Otter, J. T. Padding, J. K G Dhont, and W. J. Briels. Brownian dynamics simulations of the self- and collective rotational diffusion coefficients of rigid long thin rods. *Journal of Chemical Physics*, 122:0–10, 2005.

[26] M P Lettinga, E Barry, and Z Dogic. Self-diffusion of rod-like viruses in the nematic phase. *Europhysics Letters*, 71:692–698, 2005.

[27] E Grelet, M. Paul Lettinga, M Bier, R van Roij, and P van der Schoot. Dynamical and structural insights into the smectic phase of rod-like particles. *J. Phys. Cond. Matt.*, 20:494213, 2008.

[28] M P Lettinga and E Grelet. Self-diffusion of rodlike viruses through smectic layers. *Phys. Rev. Lett.*, 99:197802, Nov 2007.

[29] E Pouget, E Grelet, and M P Lettinga. Dynamics in the smectic phase of stiff viral rods. *Physical Review E*, 041704:1–6, 2011.

[30] R van Roij, M Dijkstra, P van der Schoot, and M Bier. Self-Diffusion of Particles in Complex Fluids : Temporary Cages and Permanent Barriers. *Phys. Rev. Lett.*, 215901:1–4, 2008.

[31] Joseph E. Mayer. The Theory of Ionic Solutions. *The Journal of Chemical Physics*, 18:1426–1436, 1950.

[32] G. J. Vroege and H. N. W. Lekkerkerker. Phase transitions in lyotropic liquid crystals: bilayer and micelle stability. *Reports on Progress in Physics*, 55:1241–1309, 1992.

[33] Z Y Chen. Nematic ordering in semiflexible polymer chains. *Macromolecules*, 26:3419–3423, 1993.

[34] G. J. Vroege and Henk N W Lekkerkerker. Phase transition in Lyotropic colloidal and plymer liquid crystals. *Reports on Progress in Physics*, 55:1241–1309, 1992.

[35] Albert P. Philipse. The Random Contact Equation and Its Implications for (Colloidal) Rods in Packings, Suspensions, and Anisotropic Powders. *Langmuir*, 12:1127–1133, 1996.

[36] A. R. Khokhlov and A. N. Semenov. Liquid-crystalline ordering in the solution of partially flexible macromolecules. *Physica A: Statistical Mechanics and its Applications*, 112:605–614, 1982.

[37] A. Stroobants, H. N. W. Lekkerkerker, and T. Odijk. *Macromolecules*, pages 2232–2238.

[38] M Hosino, H Nakano, and H Kimura. Nematic-smectic transition in an aligned rod system. *Journal of the Physical Society of Japan*, 46:1709–1715, 1979.

[39] Xin Wen and Robert B. Meyer. Model for smectic-A ordering of parallel hard rods. *Physical Review Letters*, 59:1325–1328, 1987.

[40] B Mulder. Density-functional approach to smectic order in an aligned hard-rod fluid. *Physical Review A*, 35:3095–3101, 1987.

[41] Daan Frenkel. Structure of Hard-core Models for Liquid Crystals. *J. Phys. Chem*, 91:3280–3284, 1988.

[42] D. Frenkel, H. N. W. Lekkerkerker, and a. Stroobants. Thermodynamic stability of a smectic phase in a system of hard rods. *Nature*, 332:822–823, 1988.

[43] C Wetter. Die Flussigkristalle des Tabak- rnosaikvirus. *Biologie in unserer Zeit*, 15:81–89, 1935.

[44] M. van Bruggen, H. Lekkerkerker, G. Maret, and J. Dhont. Long-time translational self-diffusion in isotropic and nematic dispersions of colloidal rods. *Physical Review E*, 58:7668–7677, 1998.

[45] A Kuijk, D V. Byelov, A V. Petukhov, A van Blaaderen, and Ar Imhof. Phase behavior of colloidal silica rods. *Faraday Discussions*, 159:181, 2012.

[46] T Koda and H Kimura. Phase diagram of the nematic-smectic a transition of the binary mixture of parallel hard cylinders of different lengths. *J. Phys. Soc. Jpn*, 63:984–994, 1994.

[47] P Bolhuis and D Frenkel. Tracing the phase boundaries of hard spherocylinders. *Journal of Chemical Physics*, 106:666–687, 1997.

[48] B Roij, R Mulder and M Dijkstra. Phase behavior of binary mixtures of thick and thin hard rods. *Physica A*, 261:374–390, 1998.

[49] E Medero L Raton Y, Martinez Velasco. Stability of smectic phases in hard-rod mixtures. *J. Chem. Phys*, 123:1–12, 2005.

[50] A Einstein. On the Motion of Small Particles Suspended in Liquids at Rest Required by the Molecular-Kinetic Theory of Heat. *Annalen der Physik*, 17:549–560, 1905.

[51] M. Doi. Rotational relaxation time of rigid rod-like macromolecule in concentrated solution. *Journal de Physique*, 36:607–611, 1975.

[52] K M Zero and R Pecora. Rotational and translational diffusion in semidilute solutions of rigid-rod macromolecules. *Macromolecules*, 15:87–93, 1982.

[53] E. R. Weeks. Three-Dimensional Direct Imaging of Structural Relaxation Near the Colloidal Glass Transition. *Science*, 287:627–631, 2000.

[54] D S Banks and C Fradin. Anomalous diffusion of proteins due to molecular crowding. *Biophysical journal*, 89:2960–2971, 2005.

[55] G Drazer and D H Zanette. Experimental evidence of power-law trapping-time distributions in porous media. *Physical review. E, Statistical physics, plasmas, fluids, and related interdisciplinary topics*, 60:5858–64, 1999.

[56] V. Blickle, T. Speck, U. Seifert, and C. Bechinger. Characterizing potentials by a generalized Boltzmann factor. *Physical Review E - Statistical, Nonlinear, and Soft Matter Physics*, 75:1–4, 2007.

[57] H Z Cummins, F D Carlson, T J Herbert, and G Woods. Translational and rotational diffusion constants of tobacco mosaic virus from Rayleigh linewidths. *Biophysical journal*, 9:518, 1969.

[58] T. A. King, A. Knox, and J. D. G. McAdam. Translational and rotational diffusion of tobacco mosaic virus from polarized and depolarized light scattering. *Biopolymers*, 12:1917–1926, 1973.

[59] R C. Cush and P S. Russo. Self-diffusion of a rodlike virus in the isotropic phase. *Macromolecules*, 35:8659–8662, 2002.

[60] Y G Tao, W. K. Den Otter, J. K G Dhont, and W. J. Briels. Isotropic nematic spinodals of rigid long thin rodlike colloids by event-driven Brownian dynamics simulations. *Journal of Chemical Physics*, 124, 2006.

[61] Y Tao, W K Den Otter, J T Padding, J K Dhont, W J Briels, Yu-guo Tao, W K Den Otter, and J T Padding. Brownian dynamics simulations of the self- and collective rotational diffusion coefficients of rigid long thin rod. 244903, 2011.

[62] J Käs, H Strey, J.X. Tang, D Finger, R Ezzell, E Sackmann, and P.A. Janmey. F-actin, a model polymer for semiflexible chains in dilute, semidilute, and liquid crystalline solutions. *Biophysical Journal*, 70:609–625, 1996.

[63] M P Lettinga, K Kang, A Imhof, D Derks, and J K G Dhont. Kinetic pathways of the Nematic-Isotropic phase transition as studied by confocal microscopy on rod-like viruses. *Journal of Physics: Condensed Matter*, 17:11, 2005.

[64] E Grelet. Hexagonal order in crystalline and columnar phases of hard rods. *Physical Review Letters*, 100:1–4, 2008.

[65] L Van Hove. Correlations in space and time and born approximation scattering in systems of interacting particles. *Physical Review*, 95:249–262, 1954.

[66] J.P. Hansen and I.R. McDonald. *Theory of Simple Liquids*. Elsevier Science, 1990.

[67] M Gaub, S Fritzsche, R Haberlandt, and D N Theodorou. Van Hove function for diffusion in zeolites. *Journal of Physical Chemistry B*, 103:4721–4729, 1999.

[68] W K Kegel and A van Blaaderen. Direct Observation of Dynamical Heterogeneities in Colloidal Hard-Sphere Suspensions. *Science*, 287:290–293, 2000.

[69] P Hopkins, A Fortini, A J. Archer, and M Schmidt. The van Hove distribution function for Brownian hard spheres: Dynamical test particle theory and computer simulations

for bulk dynamics. *Journal of Chemical Physics*, 133:1–20, 2010.

[70] E R Weeks and D A Weitz. Subdiffusion and the cage effect studied near the colloidal glass transition. *Chem. Phys.*, 284:361–367, 2002.

[71] C Dalle-Ferrier, M Krüger, R D. L. Hanes, S Walta, M C. Jenkins, and S U. Egelhaaf. Dynamics of dilute colloidal suspensions in modulated potentials. *Soft Matter*, 7:2064, 2011.

[72] S Naderi and P van der Schoot. Size and boundary effects on the diffusive behavior of elongated colloidal particles in a strongly confined dense dispersion. *Journal of Chemical Physics*, 139, 2013.

[73] Mikhail Dzugutov. A universal scaling law for atomic diffusion in condensed matter. *Nature*, 381:137–139, 1996.

[74] Charanbir Kaur, Upendra Harbola, and Shankar P. Das. Nature of the entropy versus self-diffusivity plot for simple liquids. *Journal of Chemical Physics*, 123, 2005.

[75] Z Dogic and S Fraden. Ordered phases of filamentous viruses. *Current Opinion in Colloid and Interface Science*, 11:47–55, 2006.

[76] M R. Hansen, P Hanson, and A Pardi. *Filamentous bacteriophage for aligning RNA, DNA, and proteins for measurement of nuclear magnetic resonance dipolar coupling interactions*, volume 317 of *Methods in Enzymology*. Academic Press, 2000.

[77] J Rakonjac. *Filamentous Bacteriophages: Biology and Applications*. John Wiley and Sons, Ltd, 2001.

[78] Hn Schafer, P Scheurich, G Rathgeber, and K Dose. Nucleotide sequence of fd bacteriophage DNA. *Nucleic Acids Research*, 4:1345–1351, 1978.

[79] C J Marzec and L A Day. DNA and Protein Lattice-Lattice interaction in the filamentous bacteriophages. *Biophysical journal*, 42:171–179, 1982.

[80] J Annstrong, J A Hewitt, and R N Perham. Chemical modification of the coat protein in bacteriophage fd and orientation of the virion during assembly and diassembly. *The EMBO Journal*, 2:1641–1646, 1983.

[81] D A Marvin and B Hohn. Filamentous Bacterial Viruses. *Bacteriological Reviews*, 33:172–209, 1969.

[82] J Armstrong, R N Perham, and John E Walker. Domain structure of bacteriophages fd adsorption protein. *FEBS Letters*, 135:1–6, 1981.

[83] C Zeri, M F Mesleh, A Nevzorov, S J Opella, Y You, P Lin, L Xue, S W Morris, D Wang, H Zeng, R Wen, X Lin, S Casola, G Cattoretti, N Uyttersprot, S B Koralov, J Seagal, Z Hao, A Waisman, A Egert, and D Ghitza. Structure of the coat protein in fd filamentous bacteriophage particles determined by solid-state NMR spectroscopy. *Pnas*, 104:2024–2025, 2007.

[84] D Alsteens, H Trabelsi, P Soumillion, and Y F. Dufrêne. Multiparametric atomic force microscopy imaging of single bacteriophages extruding from living bacteria. *Nature Communications*, 4:2926, 2013.

[85] D. Montalvan-Sorrosa, J. L. González-Solis, J. Mas-Oliva, and R. Castillo. Filamentous virus decoration with gold nanoparticles: global fingerprints of bionanocomposites acquired with SERS. *RSC Adv.*, 4:57329–57336, 2014.

[86] D A Marvin. Filamentous phage structure, infection and assembly. *Current Opinion in Structural Biology*, 8:150–158, 1998.

[87] K. Zimmermann, H. Hagedorn, C. C. Heuck, M. Hinrichsen, and H. Ludwig. The ionic properties of the filamentous bacteriophages Pf1 and fd. *Journal of Biological Chemistry*, 261:1653–1655, 1986.

[88] W M Tan, R Jelinek, S J Opella, P Malik, T D Terry, and R N Perham. Effects of temperature and Y21M mutation on conformational heterogeneity of the major coat protein (pVIII) of filamentous bacteriophage fd. *Journal of molecular biology*, 286:787–796, 1999.

[89] K R. Purdy and S Fraden. Isotropic-cholesteric phase transition of filamentous virus suspensions as a function of rod length and charge. *Physical Review E - Statistical, Nonlinear, and Soft Matter Physics*, 70:1–8, 2004.

[90] Dogic, Z and Fraden, S. Development of model colloidal liquid crystals and the kinetics of the isotropic smectic transition. *Phil. Trans. R. Soc. Lond A*, 359:997–1015, 2001.

[91] Kirstin Rachael Purdy. Liquid crystalline Phase Transitions of Monodisperse and Bidisperse Suspensions of Rodlike Colloidal Virus. *Brandeis University*, 2004.

[92] Z Dogic and S Fraden. Cholesteric phase in virus suspensions. *Langmuir*, 16:7820–7824, 2000.

[93] J. Lapointe and D. A. Marvin. Filamentous bacterial viruses viii. liquid crystals of fd. *Molecular Crystals and Liquid Crystals*, 19:269–278, 1973.

[94] F Tombolato, A Ferrarini, and E Grelet. Chiral Nematic Phase of Suspensions of Rodlike Viruses : Left-Handed Phase Helicity from a Right-Handed Molecular Helix. *Phys. Rev. Lett*, 96:258302–4, 2006.

[95] E Grelet and S Fraden. What Is the Origin of Chirality in the Cholesteric Phase of Virus Suspensions ? *Phys. Rev. Letter*, 90:2–5, 2003.

[96] S Naderi, E Pouget, P Ballesta, P van der Schoot, M P Lettinga, and E Grelet. Fractional hoppinglike motion in columnar mesophases of semiflexible rodlike particles. *Phys. Rev. Lett.*, 111:037801, Jul 2013.

[97] Glenn H. Brown and Jerome J. Wolken. *Chapter 8 - Photoreceptor Structures: The Chloroplasts*. Academic Press, 1979.

[98] Giuseppe Battaglia and Anthony J Ryan. The evolution of vesicles from bulk lamellar gels. *Nature materials*, 4:869–876, 2005.

[99] Jun Yamamoto and Hajime Tanaka. Dynamic control of the photonic smectic order of membranes. *Nature materials*, 4:75–80, 2005.

[100] J Lubkowski, F Hennecke, A Plückthun, and A Wlodawer. Filamentous phage infection: Crystal structure of g3p in complex with its coreceptor, the C-terminal domain of TolA. *Structure*, 7:711–722, 1999.

[101] N Nilsson, a C Malmborg, and C a Borrebaeck. The phage infection process: a functional role for the distal linker region of bacteriophage protein 3. *Journal of virology*, 74:4229–4235, 2000.

[102] M Vodt and R Dubelcco. Some problems of animal virology as studied by the plaque technique. *Cold Spring Harb Symp Quant Biol*, pages 273–279, 1953.

[103] J Buitenhuis. Electrophoresis of fd-virus particles: Experiments and an analysis of the effect of finite rod lengths. *Langmuir*, 28:13354–13363, 2012.

[104] Z Dogic, Kirstin R , E Grelet, M Adams, and S Fraden. Isotropic-nematic phase transition in suspensions of filamentous virus and the neutral polymer Dextran. *Physical review. E, Statistical, nonlinear, and soft matter physics*, 69:051702, 2004.

[105] B J Berne and R Pecora. *Dynamic light scattering: with applications to chemistry, biology, and physics*. Courier Corporation, 1976.

[106] S.T Hess, S Huang, A Heikal, and W Webb. Biological and chemical applications of fluorescence correlation spectroscopy: A review. *Biochemistry*, 41:697–705, 2002.

[107] D J Stephens. Light Microscopy Techniques for Live Cell Imaging. *Science (New York, NY)*, 300:82–86, 2003.

[108] H Qian, M P Sheetz, and E L Elson. Single particle tracking. Analysis of diffusion and flow in two-dimensional systems. *Biophysical journal*, 60:910–21, 1991.

[109] M J. Saxton and K Jacobson. Single-particle tracking:applications to membrane dynamics. *Annual Review of Biophysics and Biomolecular Structure*, 26:373–399, 1997. PMID: 9241424.

[110] Michael J. Saxton. *Single Particle Tracking*, pages 1–33. Humana Press, Totowa, NJ, 2009.

[111] Z Zhang and E Grelet. Tuning chirality in the self-assembly of rod-like viruses by chemical surface modifications. *Soft Matter*, 9:1015, 2013.

[112] K Li, Y Chen, S Li, H G Nguyen, Z Niu, S You, C M. Mello, X Lu, and Q Wang. *Bioconjugate Chemistry*, pages 1369–1377. PMID: 20499838.

[113] D Keilin and Hartree E.F. Inhibitors of catalase reaction. *Nature*, 134:933–933, 1934.

[114] M. L. Snyder and H. C. Lichstein. Sodium azide as an inhibiting substance for gram-negative bacteria. *The Journal of Infectious Diseases*, 67:113–115, 1940.

[115] A Forget and V Fredette. Sodium azide selective medium for the primary isolation of anaerobic bacteria. *Journal of bacteriology*, 83:1217–1223, 1962.

[116] S Naderi and P van Der Schoot. Effect of bending flexibility on the phase behavior and dynamics of rods. *Journal of Chemical Physics*, 141:124901–10, 2014.

[117] A Kuijk, A van Blaaderen, and A Imhof. Synthesis of monodisperse, rodlike silica colloids with tunable aspect ratio. *Journal of the American Chemical Society*, 133:2346–2349, 2011.

[118] H. Löwen. Anisotropic self-diffusion in colloidal nematic phases. *Physical Review E*, 59(2):1989–1995, 1999.

[119] J Tang and S Fraden. Isotropic cholesteric phase transition in colloidal suspensions of filamentous bacteriophage fd. *Liquid Crystals*, 19:459–467, 1995.

[120] M. D. Ediger. Spatially heterogeneous dynamics in supercooled liquids. *Annual Review of Physical Chemistry*, 51:99–128, 2000. PMID: 11031277.

[121] B Wang, S M. Anthony, S Chul Bae, and S Granick. Anomalous yet brownian. *Proceedings of the National Academy of Sciences*, 106:15160–15164, 2009.

[122] B Wang, J Kuo, S Chul Bae, and S Granick. When Brownian diffusion is not Gaussian. *Nature Materials*, 11:481–485, 2012.

[123] C Tsallis, S V. F. Levy, André M. C. Souza, and R Maynard. Statistical-mechanical foundation of the ubiquity of lévy distributions in nature. *Phys. Rev. Lett.*, 75:3589–3593, Nov 1995.

[124] A. Blumen, G. Zumofen, and J. Klafter. Transport aspects in anomalous diffusion: Lévy walks. *Phys. Rev. A*, 40:3964–3973, Oct 1989.

[125] H.a. Kramers. Brownian motion in a field of force and the diffusion model of chemical reactions. *Physica*, 7(4):284–304, 1940.

[126] J a Dix and a S Verkman. Crowding effects on diffusion in solutions and cells. *Annual review of biophysics*, 37:247–263, 2008.

[127] I M. Sokolov. Models of anomalous diffusion in crowded environments. *Soft Matter*, 8:9043, 2012.

[128] L Berthier. Dynamic heterogeneity in amorphous materials. *Physics*, 4:7, 2011.

[129] A Kusumi, Y Sako, and M Yamamoto. Confined Lateral Diffusion of Membrane Receptors as Studied by Single Particle Tracking (Nanovid Microscopy). Effects of Calcium-induced Differentiation in Cultured Epithelial Cells. *Biophysical Journal*, 65:2021–2040, 1993.

[130] J J. Wolken. Lipids and the molecular structure of photoreceptors. *Journal of the American Oil Chemists Society*, 43:271–274, 1966.

[131] P. Holmqvist. Short-time dynamic signature of the liquid-crystal-glass transition in a suspension of charged spherical colloids. *Langmuir*, 30:6678–6683, 2014.

[132] R Zwanzig. Diffusion in a rough potential. *Proceedings of the National Academy of Sciences of the United States of America*, 85:2029–2030, 1988.

[133] M Lindner, G Nir, A Vivante, I T. Young, and Y Garini. Dynamic analysis of a diffusing particle in a trapping potential. *Physical Review E - Statistical, Nonlinear, and Soft Matter Physics*, 87:1–5, 2013.

[134] M Evstigneev, O Zvyagolskaya, S Bleil, R Eichhorn, C Bechinger, and P Reimann. Diffusion of colloidal particles in a tilted periodic potential: Theory versus experiment. *Physical Review E - Statistical, Nonlinear, and Soft Matter Physics*, 77:1–4, 2008.

[135] G Volpe, G Volpe, and S Gigan. Brownian motion in a speckle light field: tunable anomalous diffusion and selective optical manipulation. *Scientific reports*, 4:3936, 2014.

[136] P Tierno and M R Shaebani. Soft Matter magnetic colloids driven above a two-state flashing potential. *Soft Matter*, 12:3398–3405, 2016.

[137] K Kang, A. Wilk, J. Buitenhuis, A. Patkowski, and Jan K G Dhont. Diffusion of spheres in isotropic and nematic suspensions of rods. *The Journal of chemical physics*, 124:044907, 2006.

[138] R. Van Der Haegen H. N. W. Lekkerkerker, Ph. Coulon and R. Deblieck. On the isotropic liquid crystal phase separation in a solution of rodlike particles of different lengths. *Journal of Chemical Physics*, 1:3427–3433, 1984.

[139] S Varga, K Purdy, A Galindo, S Fraden, and G Jackson. Nematic-nematic phase separa-

tion in binary mixtures of thick and thin hard rods: Results from Onsager-like theories. *Physical Review E - Statistical, Nonlinear, and Soft Matter Physics*, 72:1–19, 2005.

[140] L N. Buitenhuis, Jand Donselaar, Paul A. Buining, A Stroobants, and Henk N W Lekkerkerker. Phase Separation of Mixtures of Colloidal Boehmite Rod and Flexible Polymer. *Journal of Colloid and interface science*, 175:46–56, 1995.

[141] Naama Gal and Daphne Weihs. Experimental evidence of strong anomalous diffusion in living cells. *Physical Review E - Statistical, Nonlinear, and Soft Matter Physics*, 81(2):5–8, 2010.

[142] Julia F. Reverey, Jae-Hyung Jeon, Han Bao, Matthias Leippe, Ralf Metzler, and Christine Selhuber-Unkel. Superdiffusion dominates intracellular particle motion in the supercrowded cytoplasm of pathogenic Acanthamoeba castellanii. *Scientific Reports*, 5(February):11690, 2015.

[143] D Stauffer, C Schulze, and D W Heermann. Superdiffusion in a Model for Diffusion in a Molecularly Crowded Environment. *J. Biol. Phys*, 34:1–8, 2008.

[144] P Illien, O Bénichou, G Oshanin, and R Voituriez. Velocity anomaly of a driven tracer in a confined crowded environment. *Physical Review Letters*, 113:1–5, 2014.

[145] G Gradenigo, E Bertin, and G Biroli. Field-induced superdiffusion and dynamical heterogeneity. *Physical Review E - Statistical, Nonlinear, and Soft Matter Physics*, 93:1–5, 2016.

[146] Tian Hui Zhang and Xiang Yang Liu. Configurations and diffusion of point defects in two-dimensional colloidal crystals. *Applied Physics Letters*, 89(26):147–150, 2006.

[147] B. van der Meer, W. Qi, J. Sprakel, L. Filion, and M. Dijkstra. Dynamical heterogeneities and defects in two-dimensional soft colloidal crystals. *Soft Matter*, pages 9385–9392, 2015.

[148] Michael P Allen, Mark A Warren, and Mark R Wilson. Molecular-dynamics simulation of the smectic- A * twist grain-boundary phase. *Physical Review E*, 57:5585–5596, 1998.

[149] Nasser Mohieddin Abukhdeir and Alejandro D. Rey. Edge dislocation core structure in

lamellar smectic-A liquid crystals. *Soft Matter*, 6(6):1117, 2010.

[150] Delphine Coursault, Johan Grand, Bruno Zappone, Habib Ayeb, Georges Lévi, Nordin Félidj, and Emmanuelle Lacaze. Linear self-assembly of nanoparticles within liquid crystal defect arrays. *Advanced Materials*, 24(11):1461–1465, 2012.

[151] Chris D. Muzny and Noel A. Clark. Direct observation of the brownian motion of a liquid-crystal topological defect. *Physical Review Letters*, 68(6):804–807, 1992.

[152] Robin L Blumberg Selinger. Diffusion in a smectic liquid crystal with screw dislocations. *Physical Review E - Statistical, Nonlinear, and Soft Matter Physics*, 65(5):1–4, 2002.

[153] F. C. Frank. I. Liquid crystals. On the theory of liquid crystals. *Discussions of the Faraday Society*, 25:19, 1958.

[154] P Oswald and P Pieranski. *Smectic and Columnar Liquid Crystals: Concepts and Physical Properties Illustrated by Experiments*. 2005.

[155] J. W. Goodby. Twisted and frustrated states of matter. *Proceedings of the Royal Society A: Mathematical, Physical and Engineering Sciences*, 468(2142):1521–1542, 2012.

[156] A. R. Bausch and K. Kroy. A bottom-up approach to cell mechanics. *Nature Physics*, 2:231–238, 2006.

[157] J Howard and A A. Hyman. Dynamics and mechanics of the microtubule plus end. *Nature*, 422:753–758, 2003.

[158] R Everaers. Rheology and Microscopic Topology of Entangled Polymeric Liquids. *Science*, 303:823–826, 2004.

[159] P. G. de Gennes. Reptation of a Polymer Chain in the Presence of Fixed Obstacles. *The Journal of Chemical Physics*, 55:572, 1971.

[160] M. Doi and S. F. Edwards. *The Theory of Polymer Dynamics*. Oxford University Press, USA, nov 1986.

[161] Z Bu, P S Russo, D L Tipton, and I I Negulescu. Self-Diffusion of Rodlike Polymers in Isotropic Solutions. *Macromolecules*, 27:6871–6882, 1994.

[162] G. J. Doucet, J. Qiu, and P. S. Russo. Effect of length on the diffusion of a rodlike polymer at concentrations spanning the isotropic-Lyotropic transition. *Journal of Physical Chemistry B*, 114:4777–4782, 2010.

[163] Y L S Tse and H C. Andersen. Modified scaling principle for rotational relaxation in a model for suspensions of rigid rods. *Journal of Chemical Physics*, 139:044905–18, 2013.

[164] P D Cobb and J E Butler. Simulations of concentrated suspensions of rigid fibers : Relationship between short- time diffusivities and the long-time rotational diffusion. *J. Chem. Phys*, pages 054908–19.

[165] S Leitmann, F Höfling, and T Franosch. Tube Concept for Entangled Stiff Fibers Predicts Their Dynamics in Space and Time. *Physical Review Letters*, 117:097801, 2016.

[166] M M Hurley and Peter Harrowell. Non Gaussian behavior and the dynamical complexity of particle motion in a dense two dimensional liquid. *J. Chem. Phus*, 105:10521–26, 1996.

[167] T Savin and P S Doyle. Static and dynamic errors in particle tracking microrheology. *Biophysical journal*, 88:623–638, 2005.